Title
Development of Amorphous-silicon-based Optical Coatings for Gravitational-wave Detectors

Author
Zhou, Ruinan

Publication Date
2023

Peer reviewed|Thesis/dissertation

Development of Amorphous-silicon-based Optical Coatings for Gravitational-wave Detectors

By

Ruinan Zhou

A dissertation submitted in partial satisfaction of the

requirements for the degree of

Doctor of Philosophy

in

Engineering - Materials Science and Engineering

in the

Graduate Division

of the

University of California, Berkeley

Committee in charge:

Professor Frances Hellman, Chair
Professor Steven G. Louie
Professor Jie Yao

Summer 2023

Abstract

Development of Amorphous-silicon-based Optical Coatings for Gravitational-wave Detectors

by

Ruinan Zhou

Doctor of Philosophy in Engineering - Materials Science and Engineering

University of California, Berkeley

Professor Frances Hellman, Chair

The search for new coating materials, particularly high-refractive-index layers, is crucial in the field of interferometric gravitational-wave (GW) detectors. These detectors require coatings with low mechanical loss to minimize thermal noise and low optical absorption to maintain measurement stability and precision. The development of novel high-index coating materials with improved mechanical and optical properties has the potential to advance GW detection and enable more precise measurements of astrophysical phenomena.

This study investigated the structural and mechanical properties of amorphous silicon (*a*-Si), hydrogenated amorphous silicon (*a*-Si:H), and amorphous silicon carbide (*a*-SiC) films deposited using magnetron sputtering (MS). The effects of deposition parameters, such as working gas, gas pressure, substrate temperature, and post-growth treatments including vacuum annealing and post-hydrogenation, were explored. The choice of working gas and its pressure, which influences the kinetic energy of the sputtered atoms upon arrival at the substrate, was found to significantly affect the properties of the deposited films. The impact of energetic incoming atoms is reflected in compressive film stress and film densification, a phenomenon known as the atomic peening effect. Additionally, a transition in dominant defects from nanovoids in e-beam *a*-Si to divacancies and self-interstitials in MS *a*-Si was observed, which can be attributed to the higher kinetic energy of incident atoms. By selecting appropriate working gas and deposition conditions, such as low gas pressure and high growth temperature, the structural order was improved, as indicated by lower bond angle deviation, and the mechanical loss of MS *a*-Si was reduced at both low temperatures and room temperature.

Introduction of hydrogen to *a*-Si had a significant impact on its optical absorption at infrared wavelengths and the room-temperature mechanical loss. We propose that hydrogen plays a dual role in *a*-Si:H, acting as a passivating agent for dangling bonds, particularly at high temperatures, and facilitating structural relaxation, and the latter is responsible for the observed changes in the physical properties of *a*-Si:H. The incorporation of carbon in *a*-SiC films resulted in higher mechanical loss and optical absorption compared to pure *a*-Si films. These findings provide insights into the underlying mechanisms and offer potential solutions for optimizing the performance of *a*-Si-based coatings for GW detector mirrors.

ACKNOWLEDGEMENTS

I would like to express my sincere gratitude to all those who have contributed to the completion of this PhD thesis.

First and foremost, I am deeply thankful to my advisor, Frances Hellman, for her invaluable guidance and mentorship throughout my doctoral journey. Her expertise, insights, and continuous support have been instrumental in shaping the direction of this research. I am also grateful to the members of my thesis committee, Steven Louie and Jie Yao, for their time and constructive criticism.

Furthermore, I would like to express my sincere appreciation for the support and assistance provided by the members of the Hellman Lab. I want to specifically acknowledge the contributions of Manel Molina-Ruiz, who generously dedicated his time and insights to the studies conducted as part of this thesis.

This work would not have been possible without the support of my collaborators from LIGO Collaboration and Naval Research Laboratory.

My deepest gratitude goes to my mom, dad, and my younger brother for their unwavering love, understanding and encouragement, even during the most challenging times. Their unconditional support and unwavering belief in my abilities have been the driving force behind my PhD journey. As I have grown older, I have come to realize the immense impact they have had on my life, and I am truly grateful for everything they have done for me.

Lastly, I would like to thank the following: my former advisors at Oxford, Peter Wilshaw and Sebastian Bonilla for teaching me how to properly do research, Maximilian Hofer for his politeness and professionalism, the adorable squirrels on campus, whose presence brought joy, the star jasmine in front of Doe library for its delightful fragrance, and myself for staying alive, despite having said a million times that I didn't want to.

Once again, thank you all for your contributions, large and small, in making this endeavor possible.

Table of Contents

LIST OF FIGURES

LIST OF TABLES

CHAPTER 1

INTRODUCTION

1.1 Gravitational waves

Newton's theory of gravity predicts that the gravitational force exerted by a mass at a distance, r, away from its present position always has the $1/r^2$ form, regardless of the motion of the mass. Einstein's general theory of relativity, however, revolutionized our understanding of gravity and introduced the concept of gravitational waves (GWs) [1]. This theory can be summarized in just 12 words, as famously put by physicist John Wheeler: "Space-time tells matter how to move; matter tells space-time how to curve." Gravitational waves are predicted by Einstein to arise from asymmetric mass acceleration and propagate as fluctuations in space-time curvature.

1.1.1 Theory of relativity

In special theory of relativity, the space-time interval ds between any two neighbouring points is given by,

$$\begin{aligned} ds^2 &= -c^2dt^2 + dx^2 + dy^2 + dz^2 \\ ds^2 &= \eta_{\mu\nu}dx^\mu dy^\nu \end{aligned} \tag{1.1.1}$$

where $\eta_{\mu\nu}$ is the Minkowski metric of a "flat" space-time.

$$\eta_{\mu\nu} = \begin{pmatrix} -1 & 0 & 0 & 0 \\ 0 & 1 & 0 & 0 \\ 0 & 0 & 1 & 0 \\ 0 & 0 & 0 & 1 \end{pmatrix} \tag{1.1.2}$$

In general theory of relativity, the space-time is no longer "flat". Instead, it is curved in order to represent accelerating sources of gravitational field. The general statement of the definition of space-time is therefore,

$$ds^2 = g_{\mu\nu}dx^\mu dy^\nu \tag{1.1.3}$$

where the metric tensor $g_{\mu\nu}$ contains all the information about the space-time curvature. If we only consider that the gravitational field is weak, $g_{\mu\nu}$ can be decomposed into a flat space-time metric plus a small perturbation. Hence, $g_{\mu\nu}$ can be written in the form,

$$g_{\mu\nu} = \eta_{\mu\nu} + h_{\mu\nu} \tag{1.1.4}$$

Here $h_{\mu\nu}$ represents the perturbation experienced by the Minkowski space. Under the weak-field limit, Einstein's field equation can be linearized, yielding a wave equation,

$$\left(\bigtriangledown^2 - \frac{1}{c^2} \frac{\partial^2}{\partial t^2} \right) h_{\mu\nu} = 0 \tag{1.1.5}$$

The simplest solution to this wave equation is a plane wave solution in the form of,

$$h_{\mu\nu} = A_{\mu\nu} e^{ik_\alpha x^\alpha} \tag{1.1.6}$$

where $A_{\mu\nu}$ is the polarization tensor, in which the information on the amplitude and the polarization state of the wave is encoded. k_α is the wavevector that determines the propagation direction of the wave and its frequency.

The transverse traceless gauge (TT gauge) is used for the construction of $h_{\mu\nu}$. In this gauge, only the spatial components of $h_{\mu\nu}$ are non-zero, which means that the wave is transverse to its own propagation direction, and additionally, the sum of the diagonal components is zero (traceless). Based on the TT gauge, the amplitude $A_{\mu\nu}$ can be described by two independent components h_+ and $h_\times$, and can be written as,

$$A_{\mu\nu} = h_+ \epsilon_+^{\mu\nu} + h_\times \epsilon_\times^{\mu\nu} \tag{1.1.7}$$

And

$$h_+ = \begin{pmatrix} 0 & 0 & 0 & 0 \\ 0 & 1 & 0 & 0 \\ 0 & 0 & -1 & 0 \\ 0 & 0 & 0 & 0 \end{pmatrix} \quad h_\times = \begin{pmatrix} 0 & 0 & 0 & 0 \\ 0 & 0 & 1 & 0 \\ 0 & 1 & 0 & 0 \\ 0 & 0 & 0 & 0 \end{pmatrix} \tag{1.1.8}$$

if we assume the wave is propagating in the z-direction, i.e. a gravitational wave traveling in the z-direction affects only the components in the x-y plane.

A visualization of the effect of a gravitational wave passing through a ring of test masses can be seen in Fig. 1.1, in which the difference between the two polarizations of a gravitational wave is illustrated. As GW passes through these test masses, it causes an increase in their separation distance in one direction, while the distance in the perpendicular direction is decreased, thereby demonstrating the quadrupolar nature of gravitational waves.

The detection of gravitational waves is a challenging task owing to their incredibly

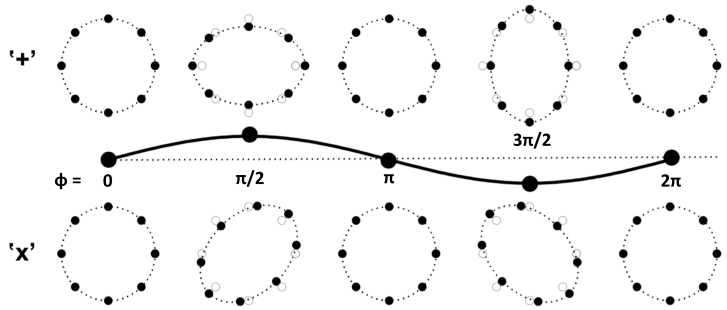

Figure 1.1: The effect of a gravitational wave passing perpendicularly through a ring of test masses. The two possible polarizations of a gravitational wave are represented by '+' (top), and '×' (bottom).

small amplitude and sensitivity of detection equipment. As a result, detectable gravitational waves are produced by extremely large astrophysical bodies [2]. Examples include black hole mergers, compact binary systems, pulsars and supernovae. In addition to these sources, a stochastic gravitational wave background is believed to exist, which is similar to the cosmic microwave background.

In conclusion, gravitation is not a force, but a phenomenon of geodesic motion through curved space-time. The paths of freely falling bodies, i.e. objects not subject to influences of non-gravitational force, define a preferred set of curves in space-time. This allows a set of free-falling masses to be employed in defining the coordination system in space-time. When a gravitational wave passes through this system, the space between the masses becomes curved, while the coordinates of the masses themselves remain unaffected.

1.2 Gravitational-wave detectors

There are two main reasons why the detection of gravitational waves is important: complementing the other ways we view the universe, such as via the electromagnetic spectrum and particles like neutrinos, and understanding the fundamental laws of physics. By detecting GWs, we are able to unveil the space-time metric around black holes, and observe the formation of black holes, the merger of binary systems and activities of massive neutron stars or supernovae. Furthermore, comparing the arrival time of light and GW generated from the same source would confirm whether Einstein's prediction on the speed of GW is correct. The polarization states of GW predicted by general relativity can also be verified. The detection of gravitational waves has practical applications as well. For example,

the technology used in GW detectors can be applied to other precision measurement applications.

Efforts to directly detect gravitational waves have been ongoing since the 1960s. It is estimated that every year, gravitational waves pass through the Earth with a strength of $10^{-23}-10^{-21}$ at around 100 Hz, which falls within the most sensitive frequency range of many GW detectors [3]. Therefore, the primary objective has been to improve the sensitivity of GW detection to levels below the amplitudes of these gravitational waves. The first detection of GW, associated with coalescence of stellar mass black holes, was made on September 14^{th}, 2015, heralding the opening of a new window for observational astronomy.

The earliest attempts at GW detection were undertaken by Joseph Weber at the University of Maryland [4]. Weber used long aluminum bars with resonant modes that may be excited by a passing GW. However, those resonant bar-shaped detectors were limited to a very narrow bandwith and poor sensitivity, and did not manage to produce replicable results [5]. Studies were also carried out using pulsar timing to analyze gravitational waves. While these observations did not confirm the existence of gravitational waves, they did show that the binary pulsar system is losing energy at a rate faster than can be explained by electromagnetic radiation alone [6–10]. This work earned Hulse and Taylor the Nobel Prize in Physics in 1993.

Research has shifted towards utilizing laser interferometers capable of high sensitivities over a broad frequency band. This led to the creation of a global network of first-generation interferometric GW detectors. These detector projects utilize laser interferometry to measure the fluctuating tidal strains in space caused by gravitational waves. The measurements involve monitoring the fluctuations in the relative positions of highly reflective mirrors, which are separated by kilometer-scale distances. The second-generation detector era is composed of several projects worldwide, including the American Advanced LIGO [11], the French/Italian Advanced Virgo [12], the German/British GEO 600 [13], and the Japanese KAGRA [14]. Many of these detectors are currently undergoing significant upgrades to improve their sensitivity. My work is closely related to the U.S. project LIGO, which will be described in detail in the following section. Additionally, it is relevant to the Virgo project, which utilizes the same technologies as those employed in LIGO.

1.2.1 LIGO

Laser Interferometer Gravitational-wave Observatory (LIGO) is an astronomical instrument designed to probe the universe by detecting gravitational waves. LIGO consists of two distantly located interferometers, one in Hanford, Washington, and one in Livingston, Louisiana. The site locations were chosen to be sufficiently separated so that the environmental perturbations are independent and therefore uncorrelated. The two LIGO detectors are Michelson interferometers with 4 km-long arms and resonant Fabry-Perot cavities. After operating for 9 years without detection, the initial LIGO detectors were upgraded to the current Advanced LIGO (aLIGO), which successfully observed gravitational waves and earned Weiss, Barish and Thorne the 2017 Nobel Prize in Physics. Ongoing improvements in aLIGO aim to suppress noise and expand the range of observable compact masses while maintaining signal strength [11].

Figure 1.2 presents a schematic diagram of the aLIGO detector and an aerial view of the LIGO Livingston site. The device comprises a light source, a beam-splitter that acts as a partially reflecting mirror, and two test masses positioned at a distance from the beam-splitter in two orthogonal directions. LIGO's test masses are large transparent cylinders made of fused silica, with a diameter of 34 cm and a thickness of 20 cm, coated with thin reflective dielectric layers. Light transmitted through the beam-splitter travels towards one of the test masses while the reflected beam travels down the orthogonal arm. The laser beams reflected from the end test masses return and interfere at the beam-splitter (BS).

The core function of a Michelson interferometer is to convert the phase difference in the light that returns to power modulation at the reflection and output port. To enhance the displacement-to-phase response of the arms, Fabry-Perot cavities are utilized, enabling multiple beam passes before exiting through the input test mass to the beam-splitter. This leads to a significant power boost within the 4 km arms, increasing the initial laser power of 125 W to 750 kW. This results in amplified signals, aided by signal recycling [11].

The interferometer compares the distance the light beams traveled (L) in the two arms. If the distances differ by zero or a whole number of wavelengths, destructive interference would take place, which translates into a weak or no signal at the photodetector. If they differ by a whole number and a half wavelength there will be constructive interference and a strong signal will be detected. The power of the light detected at the photodetector, P_{out}, can be expressed as:

$$\begin{aligned} P_{out} &= P_{in} sin^2(\Delta\phi) \\ &= P_{in} sin^2(2k\Delta L) \end{aligned} \tag{1.2.1}$$

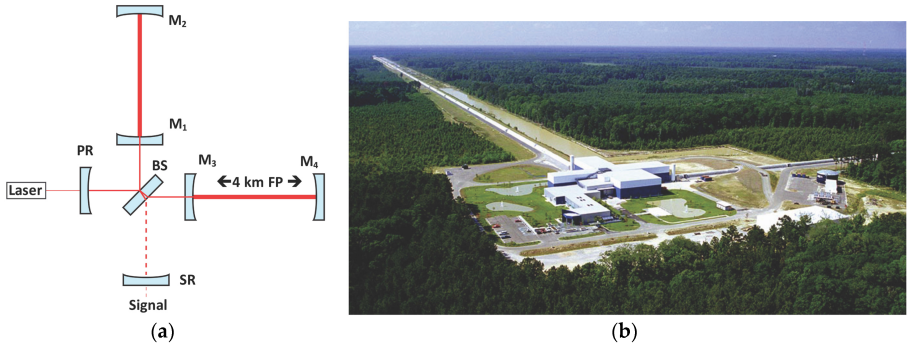

Figure 1.2: (a) Simplified schematic interferometric configuration used in aLIGO. (b) LIGO Livingston gravitational-wave detector, taken from Ref. 15.

where P_{in} is the input power of the laser, $\Delta\phi$ is the phase difference and k is 2π multiplied by frequency.

When a gravitational wave passes through the interferometer, the local space-time is altered, leading to an effective change in the length of the arms. Due to the incoming GW, one of the interferometer arms is shortened, while the other gets lengthened, causing the beams to become slightly out of phase with respect to the initial beam. After several trips down the Fabry-Perot cavities, the two separate beams leave the arms, recombine at the beam splitter, and result in a measurable signal at the photodetector, as illustrated in Fig. 1.3.

To maximize the power of the light stored in the arm cavities, a power recycling mirror (PRM in Fig. 1.3) is placed at the input port to reflect any light that exits back into the interferometer. An additional cavity is made to ensure that no light is reflected back to the laser [16].

Another technology used in LIGO detectors that is similar in concept to power recycling is signal recycling. A partially reflective mirror is inserted in between the beam splitter and the photodetector, shown as SRM in Fig. 1.3. This mirror is designed to reduce the sensitivity of GW detection to mirror imperfections, leading to more efficient signal detection.

1.2.2 Limitations on detector sensitivity

Precise measurement of gravitational waves is one of the biggest challenges in modern physics. The LIGO detectors are designed to detect a strain or fractional change in length of 10^{-21} m or below, resulting in an arm length change of

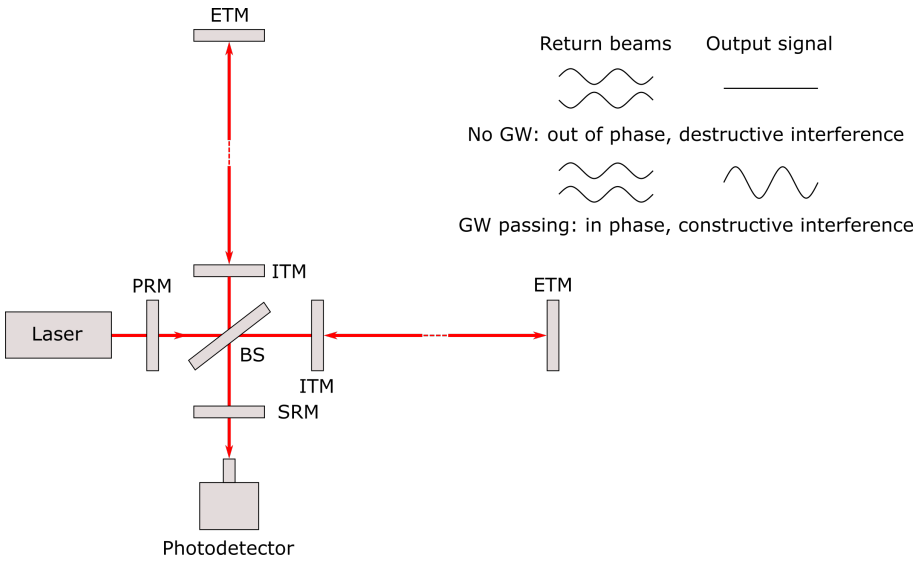

Figure 1.3: The working principle of a laser interferometric GW detector.

only 10^{-18} m (due to the use of a 4 km-long baseline), which is a thousand times smaller than the diameter of a proton. Reducing the noise level in the instrument is crucial to detect the extraordinarily small changes and distinguish them from non-gravitational sources mimicking genuine GW signals. To achieve this, LIGO utilizes special interferometry techniques, state-of-the-art optics, highly stable lasers, and multiple layers of vibration isolation to increase its sensitivity and minimize background noise. The noise budget of aLIGO, depicted in Fig. 1.4, illustrates the major contributors to the overall noise [17]. The sensitivity of LIGO to gravitational waves is affected by various factors across different frequency ranges. Seismic activity limits sensitivity at low frequencies (<10 Hz), whereas thermal noise in the suspensions and test masses, particularly in the coatings of test masses, becomes significant within the range of 10−200 Hz. At higher frequencies (around 200−10000 Hz), the quantum nature of light imposes limitations. This section discusses each fundamental noise source in detail, along with the steps taken to mitigate them.

1.2.2.1 Seismic noise

Seismic noise, resulting from continuous ground motion, significantly limits the sensitivity of ground-based interferometric GW detectors in the low-frequency range. This noise spectrum originates from various sources, including wind, ocean waves and human activity. At 30 Hz, the seismic noise is a billion times stronger than the level needed for detecting gravitational waves [18]. To mitigate this, the

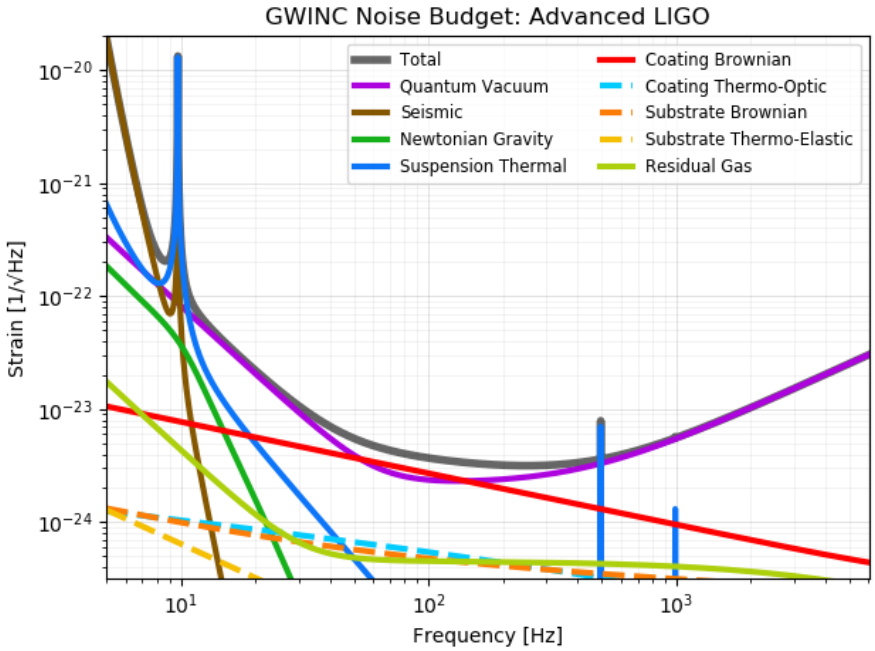

Figure 1.4: Advanced LIGO noise budget [17].

test masses must be isolated from ground disturbances. This is achieved through cascaded, multi-stage seismic isolation systems and pendulum suspension, which shield the test masses from seismic vibrations.

Through the transfer function of an N-staged pendulum suspension, the attenuation achieved can be expressed as [2],

$$\frac{x}{x_g} \approx \left(\frac{f_0}{f}\right)^{2N} \tag{1.2.2}$$

where x is the displacement of the test mass, x_g the ground motion, f_0 the resonant frequency of the mass, and f the frequency of interest.

1.2.2.2 Gravity-gradient noise

Gravity-gradient noise, also known as the Newtonian noise, is caused by fluctuations in the Newtonian gravitational field resulting from seismic mass density fluctuations in the vicinity of the test mass. Unlike seismic noise, this noise cannot be reduced through the isolation systems. However, it may be suppressed by monitoring ground motion and predicting the gravity field caused by the motion.

Choosing a site with low seismic activity for the detector can also reduce gravity-gradient noise [19]. The best solution is placing the detector somewhere other than the Earth's surface. Take the Japanese detector project KAGRA for example. An underground location was chosen in the Kamioka mines in Japan [14]. Einstein Telescope is expected to follow suit by incorporating underground interferometers into its design [20]. Space-based detectors have also been proposed as an alternative solution [21].

1.2.2.3 Quantum noise

As described earlier in Sec. 1.2.1, interferometers are designed to sense the change in the interference pattern at the output, and quantum fluctuations of light and in the movement of the center of test masses set a limit on the measurement accuracy. This quantum noise can be divided into two components: photon shot noise, and radiation pressure noise.

Photon shot noise arises from the statistical fluctuation in the number of photons collected at the photodetector. At high frequencies, photon shot noise is an important sensitivity limit, as it scales almost linearly with frequency. It is the dominant noise source at frequencies greater than several hundred Hz [22]. To minimize photon shot noise, it is desirable to increase the input laser power and the time spent within the detector by the light. This can be achieved by extending the arm length, or introducing delay lines or Fabry-Perot cavities.

While raising the laser power would be ideal for minimizing photon shot noise, it can contribute to another noise source: radiation pressure noise, which is most significant at low frequencies. Radiation pressure noise occurs because incident photons carry momentum that is transferred to the mirrors, causing slight displacements, and thus, is proportional to the laser intensity. Although increasing the mirror's mass and the interferometer arm length can reduce the effects of radiation pressure, the noise increases with the input laser power. The effect of photon shot noise decreases with increasing laser power, whereas radiation pressure noise increases. Therefore, there is an optimum laser power that minimizes the quantum noise. This sensitivity limit to the optimum laser power is known as the Standard Quantum Limit (SQL), and corresponds to the Heisenberg Uncertainty Principle in its position and momentum formulation. Research has shown that the SQL can surpassed by using squeezed light techniques. These techniques have already been implemented in aLIGO and are planned to be further enhanced in future upgrades [23, 24].

1.2.2.4 Thermal noise

The dominant source of noise in the mid-frequency range (10−200 Hz), the most sensitive frequency band of an interferometric detector, is thermal noise [11]. Thermal noise is a combination of three sources: Brownian noise, thermoelastic noise and thermo-refractive noise, which will be discussed in more detail in Sec. 2.1. Thermal noise did not play a significant role in limiting the performance of first-generation GW detectors, as it was overshadowed by technical sources of noise. However, in second-generation GW detectors, the sensitivity is constrained by thermal noise in the dielectric reflective coatings at their most sensitive frequency bands [25], as shown in Fig. 1.4, which shows the noise budget of aLIGO [26]. The Brownian noise generated by the coatings (represented in red) has a significant contribution between 10 to 200 Hz.

1.3 Amorphous materials for GW mirror coatings

Currently, aLIGO uses multilayer dielectric mirror coatings made of stacks of ion beam-sputtered low-index amorphous silica (SiO_2) and high-index titania (TiO_2)-doped tantala (Ta_2O_5) [11]. Amorphous dielectric materials have garnered particular interest for coating applications in LIGO test masses due to two main reasons. Firstly, traditional metal coatings absorb too much light at the operating laser wavelength (1064 nm [11]), resulting in unwanted melting of the coatings. Secondly, amorphous coatings can be deposited uniformly on a large scale. In comparison, although crystalline films possess more desirable properties, particularly low thermal noise [27, 28], they are difficult to grow without defects, such as grain boundaries. This challenge is especially pronounced for deposition on 34 cm diameter test masses. Additionally, to ensure epitaxial growth, the selected high-index and low-index materials must have similar lattice constants. These problems are not an issue with amorphous coatings. Consequently, researchers have focused on improving the performance of amorphous coatings to enhance their suitability for GW detectors.

Amorphous solids are structurally distinct from crystals in that they lack long-range order (LRO). Instead, they exhibit short-range order (SRO) and sometimes medium-range order (MRO), which describe atomic arrangements over distances of one or two atoms and 1−3 nms, respectively. The physical properties of disordered materials differ significantly from their crystalline counterparts, and the difference is often related to the degree of structural disorder. It is interesting to note that even different forms of the same amorphous materials can exhibit

deviations in structure due to the method of formation and thermal history. In the context of GW detectors, two properties of particular interest in candidate materials are optical absorption and mechanical loss. Low absorption of incoming laser beam is crucial for minimizing the loss of laser power, and low mechanical dissipation is directly related to suppressing thermal noise in mirror coatings. This section will briefly discuss the optical and mechanical properties of amorphous materials and how they are related to the material structure, with detailed information provided in Chapter 2.

1.3.1 Optical absorption in amorphous materials

In crystalline semiconductors, it is possible to experimentally define the optical absorption edge, marked by a sudden increase in absorption at a specific photon energy. This phenomenon is related to the concept of an optical gap, which arises from fundamental calculations of the transitions between the filled valence band and the unoccupied conduction band. The lack of LRO in amorphous solids breaks the translational symmetry so that the Bloch theorem is no longer valid. But the tight-binding approximation on the other hand, stays valid due to SRO. Therefore, the wavefunctions of electrons are limited to localized regions [29]. In this regard, the most noteworthy features found in amorphous semiconductors are: (1) the absence of sharp band edges and tailing of density of states into the gap called Urbach tails [30]; (2) localization of states in energy regions where the density of states is low; (3) the existence of broad bands of defect levels in the gap (in contrast to sharp discrete levels in crystals), the so-called deep states. These are all responsible for many properties unique for amorphous semiconductors.

A typical optical absorption spectrum of amorphous semiconductors can be divided into three regions: band-to-band absorption, band-tail absorption, and absorption by deep levels [32], which are demonstrated in Fig. 1.5. Region A is the high-energy region in which the absorption takes place between non-localized states. The absorption coefficient can be described by the Tauc relation [33],

$$\alpha \approx \frac{(E - E_g)^n}{E} \tag{1.3.1}$$

where E is the photon energy, E_g is the optical band-gap energy, n is 2 for 3D materials, but typically takes values between $0.5-3$ for many amorphous semiconductors depends on the nature of the transition [31, 34]. An example of band gap extraction from the Tauc plot is shown in Fig. 1.6, which is a widely used method for determining the band gap. It is worth noting that there is another definition of the band gap occasionally used, known as the isoabsorption gap, E_{03} and E_{04}, which correspond to the photon energy at which the optical

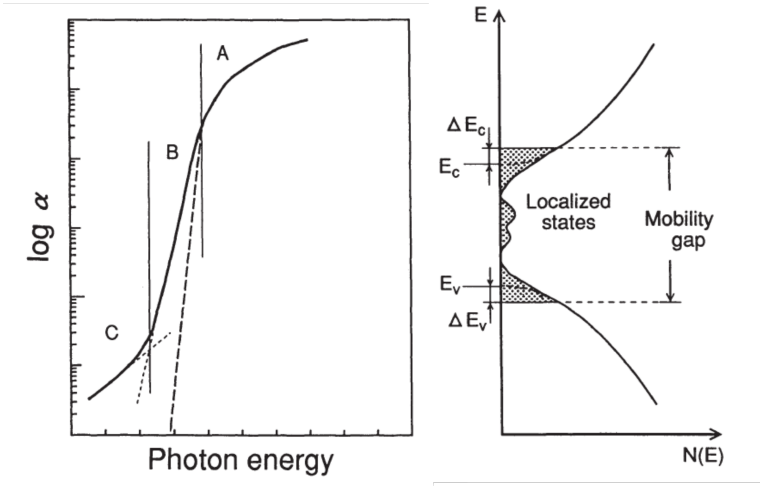

Figure 1.5: Typical behavior of optical absorption for amorphous solids in a logarithmic scale (left). The three regions, Regions A, B and C represent different absorption mechanisms. Density of states, $N(E)$, as a function of energy E for amorphous semiconductors (right). The dotted area indicates localized electronic states. ΔE_v and ΔE_c are band tails due to disorder and are responsible for absorption in Region B [31].

absorption coefficient reaches 10^3 and 10^4 cm^{-1}, respectively.

Region B is called Urbach region, since it corresponds to absorption involving Urbach tails, with a near-band edge exponential increase of absorption coefficient with photon energy,

$$\alpha \approx e^{E/E_U} \tag{1.3.2}$$

where the exponential factor E_U indicates the width of the Urbach tails [30].

In the low-absorption region (Region C), only transitions involving sub-band gap defect states take place. The absorption coefficient is thus very structure-sensitive,

$$\alpha \approx e^{E/E_d} \tag{1.3.3}$$

where E_d represents the width of the defect states.

Amorphous semiconductors, unlike crystalline semiconductors, exhibit broader absorption edges (Regions B and C). Additionally, accurately determining the absorption edge is complicated due to significant variations in optical properties of amorphous materials, depending on the synthesis conditions. Thin film thickness further adds to the challenge of precise absorption measurements.

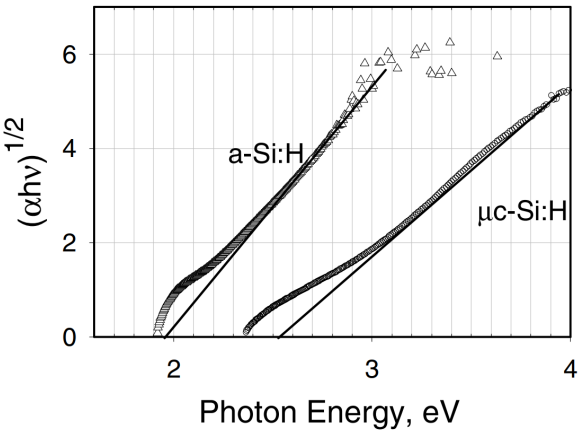

Figure 1.6: Typical Tauc plot used to estimate optical band gap of hydrogenated amorphous and microcrystalline silicon [35]. The solid line is a guide to band gap extraction, indicating the band gap as the point at which it crosses the x-axis (photon energy axis, in eV).

1.3.2 Mechanical response of amorphous materials

The mechanical response of ideal solids is described by Hooke's law, which assumes an instantaneous reaction to stress. However, real materials exhibit a phase lag in their strain response. This delayed response is known as anelasticity, characterized by mechanical loss or internal friction, which refers to the dissipation of mechanical energy during cyclic stress or strain. The extent of mechanical loss is typically quantified by the loss angle, representing the phase difference between the applied stress or strain and the resulting response. Anelastic behavior in materials arises from various underlying mechanisms. In crystalline materials, the amount of elastic energy dissipated during oscillations depends on point defects, dislocations and grain boundaries [36, 37]. In amorphous materials, the anelastic response is believed to be governed by the movement of atoms between energy states that are separated by potential barriers [38]. At low temperatures (<10 K), the energy dissipation follows a quantum tunneling model, where groups of atoms can switch between two energy levels via tunneling. This representation is known as the tunneling two-level systems (TLSs) [39, 40]. Further discussion on this will be provided in Sec. 2.2. Above 10 K, thermal activation becomes the primary source of energy loss due to mechanical response, as atoms acquire sufficient energy to overcome potential barriers.

1.4 Project objectives and thesis outline

Remarkable advancements have been made in the detection of gravitational waves, but further improvements in sensitivity are still needed. The main challenge lies in developing coatings that possess high reflectivity, low optical absorption, low thermal noise, and minimal light scattering, as these factors directly impact the detection horizon and rate of gravitational waves. To accomplish these goals, coatings must exhibit exceptional optical and mechanical properties, such as a high refractive index, minimal optical absorption, low mechanical loss, and remarkable uniformity. Amorphous materials offer advantages over crystalline materials in terms of achieving homogeneity for large-scale deposition, thereby minimizing scattering and ensuring uniform film properties. Since thermal noise is directly proportional to temperature, cryogenic operating temperatures are being considered for next-generation GW detectors, such as LIGO Voyager [41] and Einstein Telescope [20]. Therefore, it is also critical to find coating materials that contribute low thermal noise even at low temperatures.

Previous research has primarily focused on optimizing oxide coatings using techniques like adjusting deposition parameters and employing post-deposition annealing. However, these efforts have yielded limited improvements. This thesis focuses on proposing new amorphous silicon (a-Si)-based coating solutions to address the thermal noise and optical absorption problems. Through this research, it is hoped that the developed coating can be utilized in the upgrade of aLIGO and in the design of future GW detectors, thereby enhancing their scientific capabilities. This research has broader implications beyond GW detectors, particularly in the field of modern quantum devices like superconducting qubits. The presence of tunneling two-level systems, which contributes towards low-temperature mechanical loss, can also cause decoherence and limit the lifespan of quantum information storage. Therefore, the development of a-Si-based materials that are free of TLSs could benefit the advancement of quantum computing.

This thesis will have the following structure: Chapter 2 will review the sources of thermal noise and their origins, and previous work and progress made improving the physical properties of a-Si films, and their relationship to structural features. Chapter 3 will describe the experimental techniques used, including deposition parameters, post-growth treatments and characterization techniques. Chapter 4 and 5 will present investigations of the impacts of working gas and its pressure on a-Si film structure and properties. Chapter 6 will look into hydrogenated a-Si and the role hydrogen plays in these films. Chapter 7 will explore the addition of carbon into a-Si and discuss the properties of amorphous silicon carbide (a-SiC) compared to pure a-Si. The results of these a-Si-based films and their influence on the LIGO project will be summarized in a concluding chapter (Chapter 8).

CHAPTER 2
LITERATURE REVIEW

2.1 Thermal noise in mirror coatings

The current generation of GW detectors has undergone significant upgrades and is approaching the fundamental limits to noise; one of these appears to be thermal noise [42]. Thermal noise is expected to be the major noise in the mid-frequency range, the most sensitive band of GW detection. The GW community has devoted considerable efforts to investigating and modeling them. This section provides an overview of two main categories of thermal noise sources: intrinsic noise, commonly known as Brownian noise, which arises from internal friction, and extrinsic noise, driven by thermal fluctuations. Extrinsic noise encompasses thermoelastic noise and thermo-refractive noise. The origins and underlying mechanisms of these noise sources will be discussed in detail in this section.

2.1.1 Brownian noise

Brownian motion was first observed by the Scottish botanist Robert Brown in 1828. He reported complex paths of dust particles and pollen grains suspended in water [43]. A full mathematical treatment was given in 1905 by Einstein and showed that these random movements were due to collisions between particles as they underwent thermal motion [44]. Einstein also described how the pollen grains lost their kinetic energy as a result of these collisions while floating in the water. It was the first time that a dissipation process had been described as the outcome of random fluctuations. The idea of energy dissipation in a linear system was delved further by Callen et al. [45,46]. A generalized model called the fluctuation-dissipation theorem was developed, which correlates thermally driven fluctuations with energy dissipation within a system [47].

The fluctuation-dissipation theorem states that in any linear system that is in thermal equilibrium and capable of undergoing dissipative processes, there will be thermally driven stochastic fluctuations. These fluctuations are characterized by their magnitude and frequency, which are determined by the system's dissipative properties. The power spectral density, S_x, of the fluctuating system

displacement induced by thermal effects can be expressed as,

$$S_x(\omega, T) = \frac{4k_B T}{\omega^2} \Re[\mathcal{Y}(\omega)] \tag{2.1.1}$$

where ω denotes the angular frequency, T the temperature, k_B the Boltzmann constant, $\mathcal{Y}$ the admittance of the system, which is defined as,

$$\mathcal{Y}(\omega) = \frac{v(\omega)}{F(\omega)} \tag{2.1.2}$$

where a force $F(\omega)$ is applied to the system and results in a motion of velocity $v(\omega)$.

Building upon Eq. 2.1.1, Levin derived the fluctuation in displacement along the x-axis in the test masses of interferometric gravitational wave detectors, which is written in the form of [48],

$$S_x = \frac{8k_B T}{\omega^2} \frac{W_{diss}}{F_0^2} \tag{2.1.3}$$

where W_{diss} denotes the time-averaged dissipated power in the system under an oscillatory force of amplitude F_0.

For a homogeneously distributed internal loss, the term W_{diss} is then expressed by,

$$W_{diss} = \omega U \phi \tag{2.1.4}$$

where U is the maximum elastic energy stored in the system and ϕ is the mechanical loss angle, defined as $\phi = \frac{E_{dissipated}}{2\pi E_{stored}}$. The contributions from the mirror substrate and the mirror coating can be calculated separately [49],

$$\begin{aligned} S_{x,s} &= \frac{8k_B T}{\omega} \frac{1-\nu_s^2}{2\sqrt{\pi} E_s \omega_m} \phi_s \\ S_{x,c} &= \frac{8k_B T}{\pi\omega} \frac{(1+\nu_s)(1-2\nu_s)}{E_s} \frac{d_c}{\omega_m^2} \phi_c \end{aligned} \tag{2.1.5}$$

where s, c are subscripts indicating substrate and coating, respectively, ν is the Poisson's ratio, E is the Young's modulus, ω_m is the radius of the Gaussian laser beam where the irradiance is $1/e^2$, and d_c is the thickness of coating.

It can be seen from Eq. 2.1.5 that the noise generated from thermally induced movement of atoms in a material is directly proportional to the mechanical loss of the material, ϕ, or the inverse of its quality factor, Q^{-1}. Figure 2.1 depicts how Q of a mechanical system is extracted. The higher the Q, the sharper the peak at the resonant frequency, the slower the decay in oscillation amplitude,

and hence the smaller the energy loss per oscillation cycle. Therefore, a proper choice of high-Q materials for mirror coatings can suppress this intrinsic energy dissipation and greatly reduce their Brownian noise.

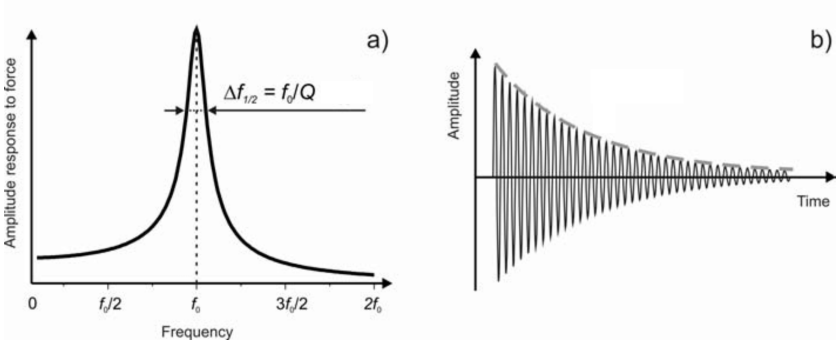

Figure 2.1: Quality factor of an oscillator, measured in (a) frequency and (b) time domain.

2.1.2 Thermoelastic noise

Thermoelastic noise is a phenomenon that arises due to thermal expansion mismatch when exposed to temperature fluctuations. In a vibrating structure, the periodic displacement field generates a temperature gradient in the elastic body, causing the compressed region to become hotter and the stretched region to become cooler. This leads to a heat transfer process in order to attain thermal equilibrium, resulting in elastic components that are out of phase with the existing ones. The energy dissipated due to this irreversible heat flow is referred to as thermoelastic loss [50, 51]. However, measuring thermoelastic noise directly is difficult, thus it is necessary to build an accurate model to estimate thermoelastic loss for various geometries. Thermoelastic noise has been extensively studied for micro- and nano-scale resonators [52–54], as well as for LIGO mirrors [55, 56].

Zener published the first analysis of thermoelastic damping in thin resonator beams undergoing flexural vibrations in 1937 [50]. Lifshitz and Roukes later improved upon Zener's model, rigorously solving the fundamental equations and leading to different approximate solutions of temperature profile, resulting in different expressions for thermoelastic loss (referred to as ϕ_{TE}) [52]. They derived ϕ_{TE} in a vibrating body from the imaginary parts of vibration frequencies by solving the classical Fourier thermal conducting equation. Zener's equation has been employed by several authors to derive ϕ_{TE} in various resonators used for mechanical loss studies [57, 58].

Fejer et al. developed an independent approach to look at ϕ_{TE} that exists in coated substrates due to thermal expansion mismatch between coating and substrate. They calculated the energy dissipated due to the elastic field induced by thermal fluctuations in the coating and in an infinite substrate [55]. Somiya and Yamamoto extended Fejer et al.'s work by considering a finite-sized substrate and proposing a different solution to the thermal equations using the elastic response of a cylinder with finite thickness [56]. The energy dissipation due to heat flow was then directly extracted from the temperature gradient.

In the context of LIGO mirrors and their multilayer coatings, accurate calculation of thermoelastic loss is essential when working with materials that have different thermal and elastic properties. Previous studies by Fejer et al. and Somiya and Yamamoto utilized a similar approach known as the effective-medium treatment to estimate the thermoelastic loss in mirrors with multilayer coatings. This method abstracts the multilayers as a homogeneous medium with weighted-average physical properties. However, the assumptions made in effective-medium approximation limit the accuracy of the thermoelastic loss estimation. We presented a more realistic model that takes into account finite-sized single-layer and multilayer coated substrates using improved methods and approximations [59]. Instead of treating the coating layers as a whole, we considered the individual interfaces between layers and considered the influence of boundary conditions. Our findings revealed that the interfaces and layer thicknesses play a significant role in shifting the frequency of the loss peak, which remained hidden in the effective-medium approximation. By incorporating these factors into our model, we were able to provide a more comprehensive understanding of thermoelastic loss. Furthermore, our work complements existing calculations on thermoelastic loss in a single body caused by thermal fluctuations. Together, these approaches can offer accurate estimations of the magnitude of thermoelastic loss in GW detector mirrors at various frequencies and temperatures.

2.1.3 Thermo-refractive noise

Thermo-refractive noise arises from the temperature dependence of the refractive index in coating materials. Fluctuations in the local temperature of the coating result in variations in the refractive index, n, thereby affecting the optical path length of the laser beam that passes through the coating. The magnitude of these refractive index fluctuations is influenced by the thermo-optic coefficient, denoted as β, which represents the rate of change of refractive index with respect to temperature (dn/dT). The power spectral density of thermo-refractive noise

calculated by Braginsky et al. is [60],

$$S_{x,\beta}(\omega) = \frac{\sqrt{2}\beta_{eff}^2 \lambda^2 k_B T^2}{\pi r_0^2 \sqrt{\omega \rho C \kappa}} \tag{2.1.6}$$

where λ is the laser wavelength, κ is the thermal conductivity of the coating, r_0 is the radius at which the intensity of the Gaussian laser beam falls to $1/e^2$ of the maximum, ρ is the density of the coating, and C is the specific heat capacity. β_{eff} is the effective temperature dependence of the refractive index of the whole coating, which is calculated from the individual coefficients of the high and low index layers from:

$$\beta_{eff} = \frac{n_L^2 \beta_H + n_H^2 \beta_L}{4(n_H^2 - n_L^2)} \tag{2.1.7}$$

in the case where the coating is composed of quarter-wavelength layers only. Here, n represents the refractive index of either the high-index (H) or the low-index (L) material.

2.1.4 Summary

Thermal noise comprises Brownian noise, thermoelastic loss, and thermo-refractive noise. Brownian noise is present in all mechanical components of an interferometer GW detector, with its greatest impact observed near and within the test masses, especially in the optical coatings on their surfaces. Coating Brownian noise limits the sensitivity of aLIGO within the frequency range of $10-200$ Hz [26]. Lowering the operating temperature and increasing the laser beam radius are approaches to mitigate this noise. However, the size of the mirrors sets a limit on the achievable beam radius, and manufacturing and suspension system requirements impose constraints on the test mass dimensions. Cryogenic cooling, as demonstrated in the KAGRA detector [14], offers a means to reduce thermal noise but introduces additional complexities, such as water condensation on the test masses. Another method for reducing thermal noise involves using high-Q substrate and coating materials with lower mechanical dissipation and favorable material properties. Measuring the frequency and temperature dependence of mechanical loss in various materials provides valuable insights for understanding dissipative mechanisms, identifying the optimal materials for test masses and their mirror coatings, and optimizing the operating conditions of GW detectors.

2.2 Mechanical loss behavior of amorphous Si

Internal friction in a material is caused by its anelasticity. When stress is applied to an ideal elastic material, it should respond instantaneously. However, in real

anelastic materials, the strain response is not instantaneous and builds up over a relaxation time [36, 61]. In the case of an oscillating stress of angular frequency ω and amplitude σ_0 applied to a material [61]:

$$\sigma = \sigma_0 e^{i\omega t} \tag{2.2.1}$$

Here, σ is the stress in the material. The resulting strain will oscillate with the same frequency as the applied stress, but will have a phase lag, ϕ, in relation to the applied stress. This phase lag arises from the strain developing over a finite relaxation time. The anelastic strain would be:

$$\epsilon = \epsilon_0 e^{i(\omega t - \phi)} \tag{2.2.2}$$

The angle of phase lag is commonly known as the mechanical loss of the material. As previously discussed in Sec. 2.1.1, mechanical loss ϕ is a measure of the fractional energy dissipated per cycle of oscillation due to anelastic behavior.

Mechanical loss is associated with adjacent energy states in the structure that can be populated by the system. It may arise from a number of causes, such as changes in atomic arrangement, point defects, dislocations, or grain boundaries in crystalline materials [36]. In amorphous materials, it is believed that mechanical loss is associated with bonding network [39] and structural features [62, 63]. At room temperature, the energy dissipation process occurs through thermal activation. In an asymmetric double-well potential, the energy barrier is surmountable due to thermal energy. A review on the room-temperature mechanical loss of a-Si will be provided in Sec. 2.4. At low temperatures, however, the thermal energy is insufficient, and the transition occurs through tunneling of TLSs. When a material undergoes mechanical vibrations, these vibrations can couple with TLSs. The interaction between phonons and TLSs results in energy exchange and dissipation. The coherent motion of phonons induces incoherent motion of TLSs. This phenomenon is evident in the deviation of heat capacity, thermal conductivity and internal friction of amorphous materials from classical theories at low temperatures. Hence, a model that describes the tunneling events was developed to describe the properties of glasses for T <1 K, which will be discussed in detail in the next section.

2.2.1 Two-level systems and the standard tunneling model

The pioneering measurements conducted by Zeller and Pohl in 1971 on the specific heat and thermal conductivity of glasses at temperatures below 1 K provided the initial insight into the distinct behavior of amorphous solids compared to their

crystalline counterparts. The data from their experiments, shown in Fig. 2.2 [64], demonstrated that the conventional Debye model is inadequate for describing the heat capacity at low temperatures, revealing the need for alternative theories.

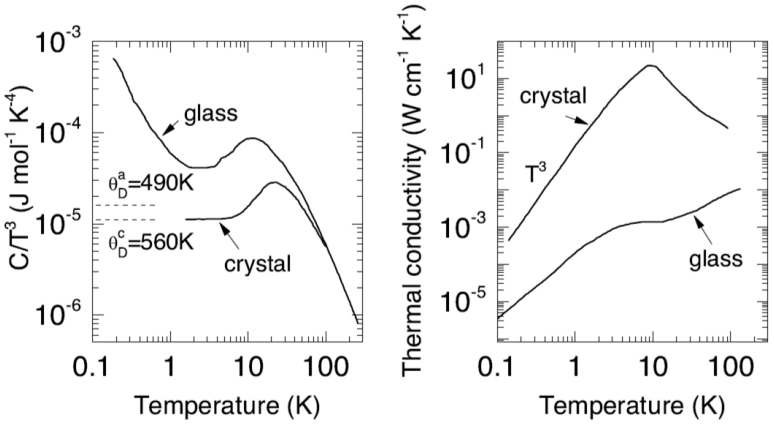

Figure 2.2: Specific heat and thermal conductivity of α-quartz and vitreous silica (a-SiO_2) [64]. The Debye specific heats (- - -) are calculated from the sound velocity [65].

The concept of tunneling two-level systems, also known as the standard tunneling model (STM), was introduced by Phillips [39] in 1972 and independently by Anderson et al. [40] to explain the excess heat capacity and the anomalous thermal conductivity of amorphous solids. A common visualization of a TLS is depicted in Fig. 2.3. An atom or a group of atoms can sit in one of the two minima in a double-well potential. At sufficiently low temperatures, the barrier separating the two local energy minima cannot be overcome via thermal jumps. Instead the dynamics are dominated by quantum tunneling.

The effective Hamiltonian in this case has the form [67],

$$H_{TLS} = \frac{1}{2}\begin{pmatrix} \Delta & \Delta_0 \\ \Delta_0 & -\Delta \end{pmatrix} \tag{2.2.3}$$

where Δ is the asymmetry energy and Δ_0 represents the energy barrier between two states, as demonstrated in Fig. 2.3.

The two lowest eigenstates, represented by $|L\rangle$ and $|R\rangle$, in the left and right potential wells, respectively, undergo hybridization due to tunneling events, and

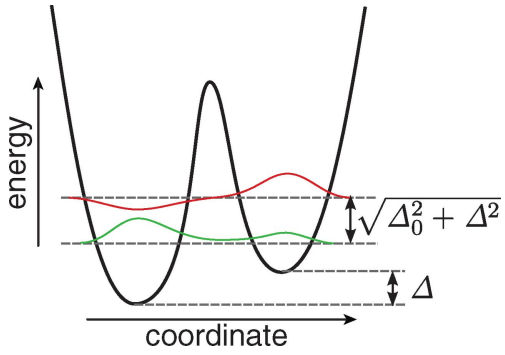

Figure 2.3: A two-level system that has two closely spaced local energy minima, with an energy barrier of Δ_0, an energy asymmetry of Δ and a splitting of $\sqrt{\Delta_0^2 + \Delta^2}$ between eigenstates [66].

therefore,

$$\begin{aligned} |\psi\rangle_+ &= sin\left(\frac{\theta}{2}\right)|L\rangle + cos\left(\frac{\theta}{2}\right)|R\rangle \\ |\psi\rangle_- &= cos\left(\frac{\theta}{2}\right)|L\rangle - sin\left(\frac{\theta}{2}\right)|R\rangle \end{aligned} \tag{2.2.4}$$

where the mixing angle θ is defined as $\tan(\theta)=\Delta_0/\Delta$. And the energy difference between the eigenstates is given by,

$$\Delta E = E_- - E_+ = \sqrt{\Delta_0^2 + \Delta^2} \tag{2.2.5}$$

White and Pohl measured the internal friction of amorphous silica films of various thicknesses. They found that there exists a temperature range in which Q^{-1} is independent of temperature, which is known as the TLS plateau, Q_0^{-1} [68], as illustrated in Fig. 2.4.

The TLS density can be extracted via the equation below according to the STM model [39, 40],

$$Q_0^{-1} = \frac{\pi}{2}\frac{\bar{P}\gamma^2}{\rho\upsilon^2} \tag{2.2.6}$$

where Q_0^{-1} is the plateau loss between 1−10 K, $\bar{P}$ is the spectral density of TLS, γ is the coupling constant between TLSs and phonons, ρ is the mass density and υ is the transverse sound velocity.

Previous studies seemed to show that the TLS density has a universal value intrinsic to the amorphous state, which has been observed in various glasses [69–73]. Hence, GW detector operation at cryogenic temperatures requires the use of

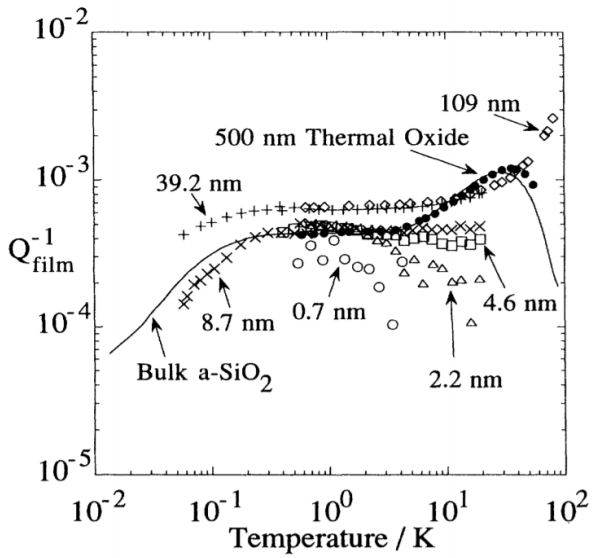

Figure 2.4: The internal friction of the a-SiO_2 films as a function of measurement temperature [68]

materials other than fused silica as mirror substrates, as it exhibits very high mechanical loss at low temperatures (Fig. 2.4). Crystalline silicon (c-Si) has been proposed as a suitable material, as it exhibits low mechanical loss at low temperatures and a zero thermal expansion coefficient at 17.6 K and 123.7 K [74, 75], resulting in zero thermoelastic loss in the substrate. Compared to the typical glassy range, a-Si exhibits a much lower mechanical loss when deposited at high temperature, as demonstrated in Fig. 2.5 [76–78]. This exceptional low-loss behavior at cryogenic temperatures makes a-Si an attractive material for reducing coating Brownian noise in GW detectors.

2.3 Optical absorption in amorphous Si

Optical absorption in a semiconductor essentially occurs when photons excite electrons from the valence band, or electron-occupied states to the conduction band. The optical absorption spectrum of a defect-free crystalline semiconductor is clearly defined, as the spectrum abruptly terminates at the band gap (E_g) due to the absence of electronic states within this region. However, in amorphous semiconductors, electronic state distributions are affected by structural disorder and extend into the gap region, leading to a broad and featureless absorption spectrum. In Fig. 2.6, the optical absorption coefficient of crystalline and amor-

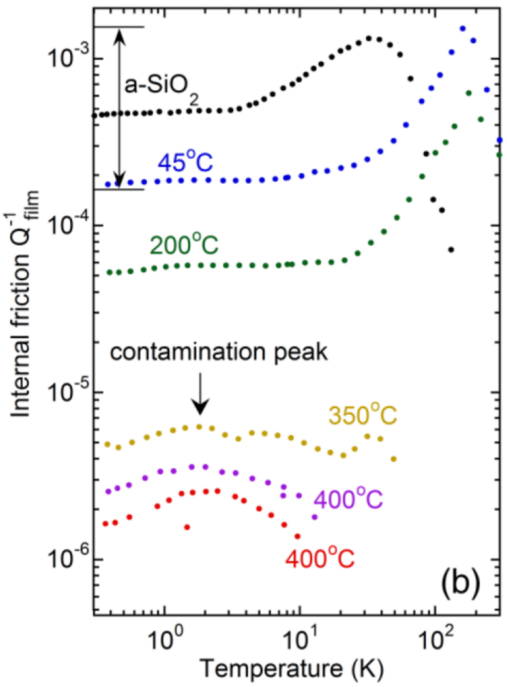

Figure 2.5: Internal friction of a-Si films made by electron-beam evaporation, and a thermal oxide layer labeled 'SiO_2'. The "contamination peak" refers to the contamination from the bare substrate [77].

phous Si is depicted. It is evident that *c*-Si exhibits higher absorption between 1.0−1.8 eV, which corresponds to wavelengths of ∼1200−700 nm, compared to *a*-Si. This necessitates the use of a longer wavelength than the current 1064 nm for *c*-Si (proposed as the mirror substrate for LIGO Voyager [41]), but *a*-Si remains a promising option for use at 1064 nm as the high-index material in GW detector mirror coatings.

As previously discussed in Sec. 1.3.1, the optical absorption spectrum of amorphous semiconductors consists of three regions. Extensive research has been conducted to identify the defects in *a*-Si that are related to absorption in Region B (Fig. 1.5), where band-edge states are responsible for photon absorption. Pierce and Spicer discussed the tailing states in *a*-Si, pointing out that the sharpness of band edges is influenced by sample preparation, and the formation of tail states is more likely related to structural imperfections, such as voids, rather than the lack of long-range order [81]. In the seminal work by Cody et al. [82], they proposed two components of disorder that lead to a tail that encroaches into the gap region: structural disorder, which is intrinsic in an amorphous network, and

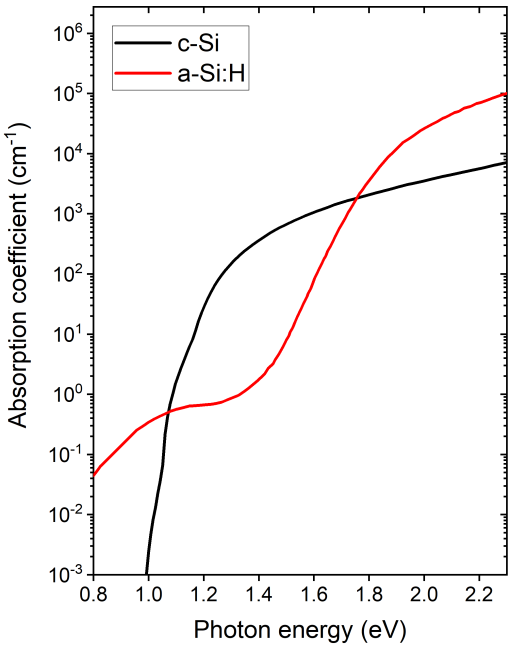

Figure 2.6: Comparison of the optical absorption coefficients of c-Si (black line) [79], and a-Si (red line) [80].

thermal disorder, induced by provision of thermal energy. They conducted a study on *a*-Si:H that looked at each of these components separately. Structural disorder was intentionally introduced into *a*-Si:H films through the thermal evolution of hydrogen at elevated annealing temperatures. The role of thermal disorder was evaluated from absorption measurements conducted at various temperatures. Their findings suggest that the impact of thermal and structural components of disorder is cumulative. Furthermore, they concluded that the improvement in structural order, which is promoted by the presence of hydrogen, is the main factor contributing to the reduction in the tail breadth, rather than the actual hydrogen content or dangling bond density.

Since hydrogenation has proven to be effective in enhancing the electrical and optical properties of *a*-Si, efforts have been devoted into investigating the role of hydrogen in *a*-Si via simulation. Initially it was widely believed that hydrogen is mainly involved in dangling bond passivation, which removes the localized states in the middle of the band gap. However, it has been found that the addition of hydrogen to the Si bonding network also results in structural reorganization and lowers the energy barrier required for the relaxation process of Si-Si bonds.

Several authors have reported on this phenomenon [83–86]. Sriraman et al. suggested that the insertion of hydrogen into strained Si-Si bonds in a bridging position or in a bond-center configuration causes chemical annealing and subsequent atomic rearrangements, leading to annihilation of these bonds. Afterward, the hydrogen atom can remain bonded to one of the Si atoms or diffuse through the network [85]. These events improve the structural order of *a*-Si and eliminate weak Si-Si bonds that are responsible for creating Urbach tails.

2.4 *a*-Si for GW mirror coating: challenges and progress

The initial interest in *a*-Si as a promising coating material for LIGO mirrors started from its extremely low loss at cryogenic temperatures compared to other glasses; its mechanical loss is about 1-2 orders of magnitude lower than the current coating materials, 25% TiO_2-doped *a*-Ta_2O_5 and *a*-SiO_2 below 10 K [77, 87, 88]. Hydrogenated *a*-Si was the first material reported to have a Q_0^{-1} below the "universal" glassy range by Liu et al. in 1997 [76]; a noticeable decrease in internal friction confirms the lack of low-energy excitations in 1 at.% hydrogenated *a*-Si:H made by hot-wire chemical vapor deposition. They attributed this phenomenon to hydrogen passivation of dangling bonds and enhanced bond regularity. However, it was later demonstrated that in spite of having dangling bonds in the structure, TLS can still be removed in unhydrogenated *a*-Si by optimizing the deposition parameters, suggesting that hydrogen is not prerequisite to suppressing TLS density in *a*-Si [77]. Queen et al. proposed that formation of TLS is related to underconstrained, low-density regions with nano-scale defects [62, 63]. Molina-Ruiz et al. [78] and Jacks et al. [89] have confirmed that while there is little variation in dangling bond density, some variation in atomic density of samples that have different Q_0^{-1} suggests that medium-range order and nanovoids play a role in density changes in electron-beam evaporated *a*-Si.

Multiple studies have investigated the mechanical loss of *a*-Si deposited by a variety of physical vapor deposition (PVD) techniques, such as electron-beam evaporation (e-beam) [77, 78, 89], ion-beam sputtering (IBS) [90], reactive low-voltage ion plating (RLVIP) [91], magnetron sputtering (MS) [92], and hot-wire chemical vapor deposition (HWCVD) [93]. Table 2.1 summarizes the loss behavior of *a*-Si prepared by these methods. It can be seen that e-beam *a*-Si grown at a substrate temperature of 425 °C exhibited the lowest low-T mechanical loss [77], whereas IBS *a*-Si showed the lowest room-temperature (RT) mechanical loss after annealing [90]. The RT loss of IBS *a*-Si is over 60% lower than that of the current high-index layer, *a*-Ti:Ta_2O_5 [94]. While the loss mechanisms at low tem-

Table 2.1: Comparison between a-Si films grown by electron-beam evaporation (e-beam), magnetron sputtering (MS), ion-beam sputtering (IBS), reactive low-voltage ion plating (RLVIP) and hot-wire chemical vapor deposition (HWCVD).

Deposition method	Growth conditions	Q_0^{-1} (1 K) $\times 10^{-5}$	Q_0^{-1} (10 K) $\times 10^{-5}$	Q_{RT}^{-1} $\times 10^{-4}$
e-beam as-deposited [77, 78, 89, 95]	RT	18.4	19.7	4.2
	425 °C	0.2	0.1	2.2
	425 °C thin film[1]	2.1	1.6	
MS as-deposited [92]	RT, 3.0 mTorr	5.4	6.2	
	303 °C, 3.0 mTorr	2.9	3.5	
	370 °C, 3.0 mTorr	1.7	2.2	
	431 °C, 3.0 mTorr	1.5	2.0	
IBS annealed[2] [90]	RT		3.3	0.9
RLVIP as-deposited [91]	250 °C		1.5	1.1
RLVIP annealed[2] [91]	250 °C			0.2
HWCVD as-deposited[3] [93]	370 °C	1.1	2.5	
HWCVD annealed[4] [93]	370 °C	1.2	2.9	

[1] Film thickness (60 nm) [78] is lower than the other two e-beam samples listed (∼300 nm) [77].
[2] Heat treatment in Ref. 90, 91 was done at 450 °C and 500 °C respectively, and performed in air. The resulted formation of SiO_2 might affect the measured properties, making direct comparison difficult.
[3] The HWCVD-deposited sample contains 7 at.% H.
[4] Annealing of the HWCVD *a*-Si:H sample was performed at 200 °C for 3 hours in vacuum.

peratures have been identified to be tunneling TLSs and understood relatively well through the STM, it is still unclear what is responsible for the mechanical dissipation at room temperature.

Although *a*-Si shows noticeably lower low-T and RT mechanical losses than *a*-Ti:Ta_2O_5, its optical absorption is quite high at the wavelength of the current detector laser (1064 nm), which is on the level of 10^4-10^5 ppm for a layer of quarter-wavelength thickness [96]. This level of absorption is significantly higher than the required ppm-level absorption for the coating. Future cryogenic detectors such as Einstein Telescope and LIGO Voyager are likely to use *c*-Si as mirror substrates, which is highly absorbing at 1064 nm, necessitating the use of longer wavelengths. At 1550 or 2000 nm, *a*-Si's optical absorption is much lower [91, 95, 96], but still needs to be improved.

Optical absorption has been studied in e-beam, IBS and RLVIP *a*-Si by several authors [91, 95, 96]. Steinlechner et al. has reported absorption measurements on a single layer of *a*-Si and a bilayer of *a*-Si/*a*-SiO_2 produced with IBS [96].

The measurements were taken at laser wavelengths of 1064 and 1550 nm, with heat treatments up to 1000 °C in both air and vacuum. It was found that heat treatment reduces absorption, with an optimal temperature of 450 °C for the *a*-Si single layer. A single layer of *a*-Si exhibits a minimum at 755 ppm for a quarter-wavelength thickness at 1550 nm after vacuum annealing. For the bilayer configuration consisting of one layer of *a*-Si and one layer of *a*-SiO_2, the minimum is observed at 1430 ppm. Cooling the bilayer from RT to 30 K reduces the optical absorption at 1550 nm by 35%. In a subsequent study, they built upon the previous findings and implemented a combination of post-growth heat treatment, cryogenic operation temperature, and a longer laser wavelength of 2000 nm on RLVIP *a*-Si. This approach is shown to suppress the absorption of a single *a*-Si layer to approximately 30 ppm [91].

Even though the absorption of *a*-Si at 1550 and 2000 nm is promising to meet the requirement for GW detector mirror coatings, its absorption at the current laser wavelength, 1064 nm, is shown to be a few thousands ppm for a quarter-wavelength thick layer, far from the ideal ppm level [96]. To address this, a multimaterial design was proposed to incorporate *a*-Si layers in the lower part of the coating stack [97]. Compared to the current coating, 11 bilayers of *a*-Ta_2O_5/*a*-SiO_2 are replaced with 5 bilayers of *a*-Si/*a*-SiO_2 in the multimaterial design. This reduces the overall coating thickness by 34% while maintaining high reflectivity, thanks to the high refractive index of *a*-Si (3.5 [98]). This, combined with *a*-Si's low mechanical loss, would lead to a much improved Brownian thermal noise in the coating, where the reduction is expected to be 25% at cryogenic temperatures and 15% at room temperature. The *a*-Si layers considered in this design were not optimized to have low absorption and mechanical loss. Therefore, further improvements in the properties of *a*-Si could potentially lead to additional reductions in overall coating absorption and thermal noise. This provides motivation for development of *a*-Si-based coatings for GW detectors operating at not only 1550 and 2000 nm, but also 1064 nm.

Given the high optical absorption of *a*-Si, finding optimal growth methods and post-growth treatments to minimize photon absorption in the infrared range is crucial for its use in GW detector mirror coatings. Improving, or at least maintaining the low mechanical loss of *a*-Si is equally important to keep the Brownian thermal noise at a minimum. To address these challenges, this project has explored the following strategies:

- Magnetron sputtering as a deposition method for *a*-Si, which allows for more flexibility in deposition conditions, including the working gas and gas pressure. Post-growth annealing in vacuum has also been studied.
- In-situ and post-growth hydrogenation of *a*-Si, as hydrogen has been effec-

tive in improving the electrical properties of *a*-Si in electronic and photovoltaic devices, and optical properties as well.

- Incorporating carbon into the *a*-Si network. Diamond-form carbon, which is sp^3 bonded, possesses a large band gap that precludes photon absorption at the three wavelengths relevant to GW detectors.

CHAPTER 3
EXPERIMENTAL METHODS

3.1 Deposition technique

Physical vapor deposition techniques are widely used in various industries and applications for thin film deposition. These techniques involve physical processes such as evaporation, sublimation or ionic impingement on a target, enabling the transfer of material atom by atom onto a substrate surface to form a growing film. In this study, we utilized magnetron sputtering, a widely used PVD technique, to deposit *a*-Si, *a*-Si:H and *a*-SiC films. Magnetron sputtering has been extensively employed in various fields such as microelectronics and surface engineering for the fabrication of films and coatings. It offers several advantages, including its simplicity, reliability and the capability to precisely control deposition parameters in order to obtain the desired film properties [99].

The fundamental sputtering process involves bombarding a target with gas ions. The ions are generated in a glow-discharge plasma in front of the target; they bombard the target surface and eject atoms which later condense on the substrate surface and form a film. Secondary electrons are also ejected from the target, which are essential to maintaining the plasma. The sputtering process is usually limited by low ionization efficiencies within the plasma and thus results in low deposition rates.

Magnetron sputtering is an advanced variation of basic sputtering through the use of a magnetic field. By aligning the magnetic field parallel to the target surface, the motion of secondary electrons is confined. This confinement leads to the formation of a dense plasma near the target, increasing the likelihood of electron-atom collisions and enhancing ionization. The use of magnetron sputtering provides additional benefits over conventional sputtering. Firstly, it enables significantly higher ion currents, resulting in higher deposition rates and faster film growth. Secondly, it allows the use of a lower working gas pressure to stabilize the plasma, thereby increasing the kinetic energy of the sputtered atoms when arriving on the substrate surface, which will be discussed further later in this section. This combination of higher ion current and higher incident atom energy contributes to improved efficiency and film quality in various thin film

applications.

Figure 3.1 illustrates different stages of film growth using PVD techniques. Initially amorphous clusters form on the substrate surface. These clusters grow in three dimensions and merge via the Volmer-Weber growth mechanism, forming density-deficient boundaries between the islands. As the growth progresses, the relatively dense region closest to the substrate undergoes a transition to a columnar grain structure, characterized by high-aspect-ratio voids along the boundaries. Adatoms generally diffuse after landing, but have a tendency to adhere near the location where they land and create columns of material, leading to subsequent formation of low-density regions due to shadowing effects [100]. When adatom mobility is enhanced during growth, either through higher kinetic energy of incident particles or elevated substrate temperature, a denser film structure is formed with a reduced number of open-volume defects incorporated into the film. In the case of e-beam *a*-Si, the 425 °C-deposited film contains a lower total volume of nanovoids than the RT-deposited *a*-Si [89].

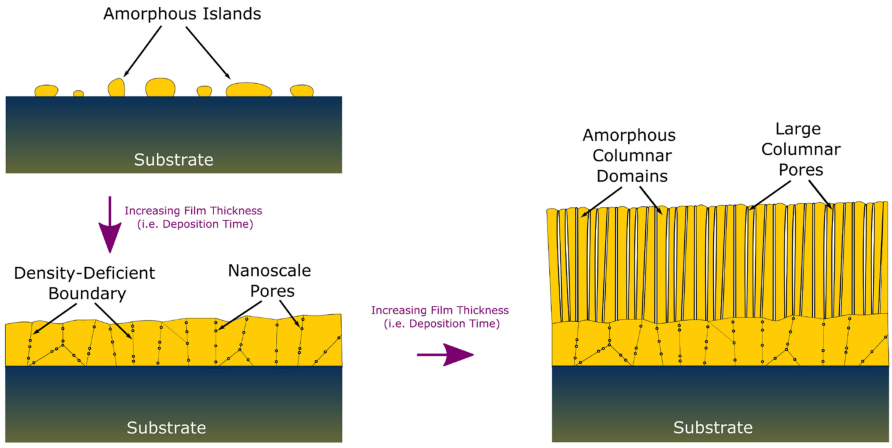

Figure 3.1: Schematic illustration depicting the evolution of amorphous film structure using PVD techniques, adapted from Ref. 100.

The kinetic energy of incoming atoms is a key differentiating factor among various PVD techniques. Take electron-beam evaporation, magnetron sputtering and ion-beam sputtering for example. In electron-beam or effusion cell evaporation, the energy per incoming particle is thermal, hence ∼10's of meV per atom. In magnetron sputtering, the energy per incoming particle is typically 100 times higher than that in electron-beam evaporation, although this can be significantly reduced by collisions with gas atoms at higher gas pressure. Ion-beam sputtering has much higher energy for deposited atoms than magnetron sputtering, with the

energy level varying from 10−1000 times higher depending on the specific growth conditions. One of the methods to manipulate incident atom energy in sputtering is by changing the bias voltage of the target gun. In this work, the gun was set to be in constant power mode, and it was found that a higher gun voltage was required to create a plasma for heavier gas when sputtering Si, under the same gas pressure. The discharge current decreased with increasing voltage, resulting in a 30−40% variation among the gases for the same power setting (Table 3.1).

Owing to a higher gun voltage, heavier gas ions possess more kinetic energy, $E_{k,gas}$, which results in a larger sputtering yield, defined as the number of target atoms sputtered by each gas ion and a larger kinetic energy for the sputtered target atoms, in this case Si. For Si, the sputtering yield with these inert gases is either below or around one atom per ion, excluding the possibility of sputtering multiple atoms by a single gas ion [101]. Hence, here we assume an one-on-one elastic collision, the kinetic energy transferred to a sputtered Si atom from a gas ion is expressed in,

$$E_{k,Si} = \frac{4m_{gas}m_{Si}\cos^2\theta}{(m_{gas}+m_{Si})^2} \times E_{k,gas} - b \tag{3.1.1}$$

where m_{gas} is the atomic mass of the working gas, m_{Si} the atomic mass of Si, θ the exit angle of the sputtered Si atom from the target, $E_{k,gas}$ the kinetic energy of gas ion upon acceleration towards the target (calculated based on accelerating voltage listed in Table 3.1), and b the surface binding energy of Si (the energy required to remove one Si atom from the target surface, 3.8 eV [102]).

The gas atoms in the chamber are typically at the thermal energy of the chamber, which is 10's of meV, far lower than the energy of compared to the ejected target atoms and are therefore considered stationary. After being ejected from the target and colliding with a gas atom in the chamber, the kinetic energy of a sputtered Si atom is reduced to,

$$E'_{k,Si} = \left(1 - \frac{4m_{gas}m_{Si}\cos^2\varphi}{(m_{gas}+m_{Si})^2}\right) \times E_{k,Si} \tag{3.1.2}$$

where φ represents the exit angle of Si atom relative to its original incoming direction, indicating the deflection in the trajectory of the Si atom. $E'_{k,Si}$ against different working gases is plotted in Fig. 3.2.

We can estimate the average incident atom energy at $\theta = \varphi = 0°$, where the target is positioned directly beneath the substrate plate, and the sputtered atoms exit the target perpendicular to its surface and to the substrate. Since for Si, the sputtering yield for all four gases studied is either below or near one atom per

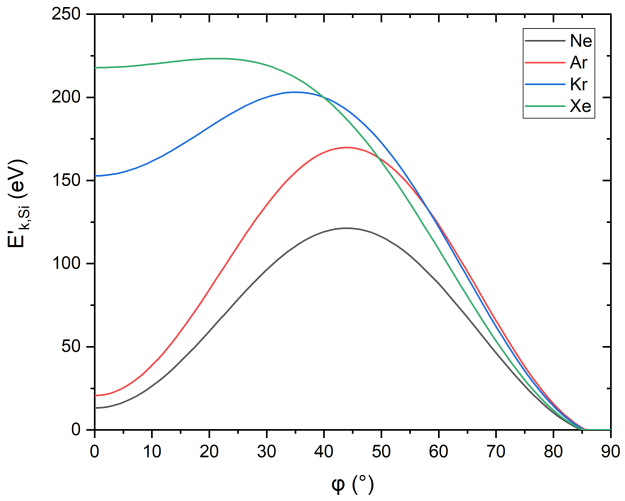

Figure 3.2: Energy left in a sputtered Si atom by various gases after one collision with a gas atom versus the exit angle of Si, based on the gun parameters listed in Table 3.1.

ion [101], the target atom is assumed to be ejected from the target surface at energy $E_{k,Si}$, calculated from Eq. 3.1.1. All collisions are assumed to be one-on-one head-on elastic collisions.

The average number of collisions experienced by the sputtered Si atoms before reaching the substrate, n, is calculated from,

$$\begin{aligned} n &= \text{Volume traveled} \times \text{no. of gas atoms per unit volume} \\ &= \pi d_{Si}^2 L \times \frac{P}{kT} \end{aligned} \tag{3.1.3}$$

where d_{Si} is the diameter of Si atom (222 pm), L the target-to-substrate distance (15.2 cm), P the gas pressure, k the Boltzmann constant and T the temperature (300 K).

After undergoing n collisions with gas atoms in the chamber, the kinetic energy of sputtered Si is reduced to $E''_{k,Si}$, which is expressed as

$$E''_{k,Si} = \left(1 - \frac{4 m_{gas} m_{Si}}{(m_{gas} + m_{Si})^2}\right)^n \times E_{k,Si} \tag{3.1.4}$$

The calculated values of n, $E_{k,Si}$ and $E''_{k,Si}$ at $\theta = \varphi = 0°$ are presented in Table 3.1, along with the corresponding deposition conditions.

Table 3.1: Deposition rate of Si and gun power (P) used in constant power mode, discharge current (I) and accelerating voltage (V) with different working gases and gas pressure, and n, $E_{k,Si}$ and $E''_{k,Si}$ at $\theta = \varphi = 0°$ calculated based on Eq. 3.1.3, 3.1.1, 3.1.4 and the corresponding deposition condition.

Working gas	P (W)	I (mA)	V (V)	Rate (Å/s)	n	$E_{k,Si}$ (eV)	$E''_{k,Si}$ (eV)
Ne 11.0 mTorr	120	244	493	0.29	8.3	475.5	5.1×10^{-11}
18.0 mTorr	120	253	475	0.17	13.6	456.1	4.9×10^{-11}
Ar 1.5 mTorr	120	174	687	0.53	1.1	661.8	12.8
1.5 mTorr	85	169	497	0.30	1.1	477.7	9.27
4.0 mTorr	100	199	495	0.57	3.0	475.8	1.3×10^{-2}
Kr 1.5 mTorr	85	105	820	0.33	1.1	611.2	126.5
Xe 0.5 mTorr	60	63	933	0.25	0.4	537.7	387.0
1.5 mTorr	60	67	901	0.16	1.1	519.1	193.5

$E''_{k,Si}$ against different working gases and gas pressures is plotted in Fig. 3.3. For Ar, even 1.5 mTorr results in significant thermalization of the initially high energy Si atoms ($E_{k,Si}$ >600 eV and $E''_{k,Si}$ ~10 eV, which is reduced more at 4.0 mTorr (0.01 eV)). For the heavier gases (Kr and Xe), their $E_{k,Si}$ (~500−600 eV) is only somewhat reduced by collisions (to 387 eV for 0.5 mTorr and 194 eV for 1.5 mTorr).

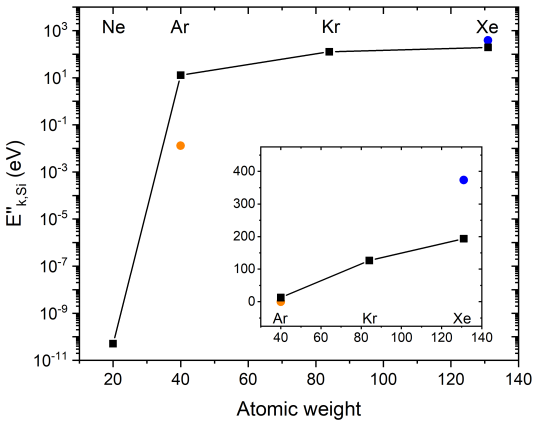

Figure 3.3: Energy of an incident Si atom sputtered by various gases for different working gas pressures: 11.0 mTorr for Ne, and 1.5 mTorr for the other three gases. The orange circle corresponds to $E''_{k,Si}$ for Ar at 4.0 mTorr, and the blue circle represents $E''_{k,Si}$ for Xe at 0.5 mTorr.

When a gas with a large mass difference from Si is selected as the sputtering gas, the energy transfer efficiency during the initial collision between the gas ion and the target is low. However, as the sputtered Si atoms travel through the chamber and undergo subsequent collisions with gas atoms, there is no significant loss in their kinetic energy. Therefore, the usage of Kr and Xe for MS *a*-Si leads to higher $E''_{k,Si}$ compared to Ne and Ar. This calculation accords with the experimental findings in Thornton and Lamb's work studying molybdenum, in which a higher energy per incoming particle was observed with lighter sputtering gas, such as Ne and Ar, compared to Kr and Xe that are closer to Mo in atomic weight [103].

Gas pressure during deposition affects the mean free path of sputtered particles and, consequently, plays a crucial role in determining the energy carried by sputtered Si atoms. At low gas pressure, atoms ejected from the target retain higher kinetic energy, resulting in more intense bombardment of the substrate. In this situation, atomic peening occurs, which involves energetic particles colliding with the substrate, causing atomic displacement and inducing film densification [104]. At high gas pressure, because of increased collision frequency, target atoms are less energetic when arriving at the substrate surface, which in turn promotes shadowing and columnar growth with void formation at column boundaries [105]. The transition pressure at which atomic peening takes place, i.e. where the film stress shifts from compressive to tensile, is determined by various factors, including the atomic weight ratio between the sputtered atom and the working gas, as well as the distance between the substrate and the target [106].

In this work, *a*-Si, *a*-Si:H and *a*-SiC samples were prepared in high-vacuum magnetron sputtering chamber on various substrates for different measurements. The base pressure ranged from 2×10^{-8} to 1×10^{-7} Torr. An liquid nitrogen cooled trap inside the chamber near the substrates was used to eliminate water vapor during growth, as tracked by a residual gas analysis detector. The gas flow was controlled at 10 sccm, and the growth rate was 0.16−0.65 Å/s for *a*-Si/*a*-Si:H deposition, and 0.25−0.50 Å/s for *a*-SiC deposition. The substrate-to-target distance was 15.2 cm and working gas pressure varies from 1.5 to 18.0 mTorr. The temperature of the sample plate was held at 50 °C (room-temperature (RT) growth), 360 °C and 660 °C. The thickness of the films studied was kept at above 300 nm and ranged from 300−380 nm.

In-situ hydrogenation of *a*-Si was conducted in the chamber of magnetron sputtering system by mixing Ar with H_2. A gas mixture of 90% Ar and 10% H_2 was supplied in a flow rate of 5 or 10 sccm via nozzles near substrate plate, while additional pure Ar was supplied into the chamber from the bottom in a flow rate of 5 sccm to dilute the mixture gas to Ar/5% H_2 and maintain the same overall gas flow.

3.2 Post-growth processing

The effect of post-growth treatments on structural and physical properties of *a*-Si, *a*-Si:H and *a*-SiC was also explored. This section elaborates on the two processes that were employed.

3.2.1 Vacuum annealing

Heat treatment was performed in a high vacuum chamber with a base pressure of approximately $3 \times 10^{-8} - 1 \times 10^{-7}$ Torr. The heater temperature was set to 400 °C, and the substrate plate temperature was measured by thermocouples to be at 360 °C. Each annealing process lasted for 3 hours with plate rotation to ensure a uniform temperature across the plate. We note here that because nearly all of our films were grown on *c*-Si substrates, with an amorphous oxide or nitride overlayer, differential thermal contraction after a high-T growth or annealing does not have a significant influence, as the thermal expansion of *a*-Si is close to that of *c*-Si [107].

3.2.2 Post-hydrogenation

Post-hydrogenation was carried out by Ashot Markosyan at Stanford University using a standard horizontal resistance furnace. The hydrogenation was performed at 400 °C using a mixture of high purity N_2/5% H_2, with a flow rate of 20 mL/min. The hydrogenation process lasted for a duration of 3 hours.

3.3 Characterization techniques

3.3.1 Profilometry

Film thickness was measured using a KLA Tencor ASIQ profilometer and most samples were controlled to have a thickness of approximately 300−350 nm. The thickness information is required for data extraction from atomic density, film stress, dangling bond density, mechanical loss and optical absorption measurements.

3.3.2 Rutherford backscattering spectrometry

Rutherford backscattering spectrometry (RBS) was performed at University of Minnesota in a NEC model 5SDH Pelletron tandem accelerator, with α-particle beam energy of 3050 keV on samples deposited on a c-Si substrate coated with a 300 nm-a-SiN_x membrane and 50 nm-thermal oxide. SIMNRA software was used to extract sample composition and areal density from RBS spectrum [108]. Atomic density can thus be calculated based on thickness and areal density of the film.

Hydrogen content was extracted using Elastic recoil detection analysis (ERDA) on samples deposited on 2 cm×1 cm c-Si substrates. ERDA is an ion beam analysis technique used to quantify light elements in solids. This technique overcomes the limitations of RBS, which has poor sensitivity for light elements, such as hydrogen. Detection in ERDA occurs in forward geometry, meaning both scattered and recoiled particles move in the direction of the detector. Typically, a stopper foil of appropriate thickness is positioned in front of the detector to obstruct the heavier scattered projectiles or recoils originating from the sample. Since light element recoils experience less energy loss during traversal, they are not impeded by the stopper foil, thus generating a detectable signal.

3.3.3 Wafer curvature measurement

Macroscopic strain was obtained from the curvature of a 2-inch c-Si wafer before and after film deposition, which is measured by a KLA-Tencor FLX-2320 thin-film stress measurement instrument. The bare wafers were annealed at the growth temperature prior to the initial measurement to prevent any curvature change caused by heating. The macroscopic film stress is extracted using the Stoney equation:

$$\sigma_f = \frac{E_s H^2}{6h(1-\upsilon_s)}\left(\frac{1}{R}-\frac{1}{R_0}\right) \tag{3.3.1}$$

where E is the Young's modulus, H the substrate thickness, h the film thickness, υ the Poisson's ratio, R_0 and R are the curvature radii before and after film deposition, and subscripts f and s represent the film and the substrate respectively [109]. The macroscopic in-plane strain in the bonds, ε_f, in the is found from $\varepsilon_f = \sigma_f / E'_f$, where E'_f is the biaxial modulus, calculated from $E'_f = E_f/(1-\nu)$, E_f the Young's modulus of a-Si, derived from shear modulus obtained from the DPO measurements (Sec. 3.3.9) and Poisson's ratio ν of 0.22 [110]. This strain captures the difference between in-plane and out-of-plane Si–Si bond distances.

3.3.4 Raman spectroscopy

Raman spectroscopy was performed using an inVia Renishaw micro-Raman/PL system equipped with a 488 nm laser in the Wu Lab at UC Berkeley. Structural information of *a*-Si/*a*-Si:H was extracted using the following methods: the linear relation proposed by Beeman, Tsu and Thorpe [111], is used in this work to determine the bond angle deviation, $\Delta\theta$, from the full width at half maximum Γ of the transverse-optic (TO) peak at 480 cm^{-1}: $\Delta\theta = (\Gamma - 15)/6$. Strubbe et al. proposed that the trace of local bond strain tensor in *a*-Si:H is proportional to the amount of shift in TO peak from the *c*-Si TO peak position, confirmed by experimental results: $\mathrm{tr}(\varepsilon) = (\omega - \omega_0)/s$, where ω is the TO peak position measured in cm^{-1}, ω_0 is the TO peak position in *a*-Si and s is a fitting parameter, $s = 460 \pm 10\ cm^{-1}$ [112]. Their study demonstrated that a compressive local strain in Si-Si bonds would result in a shift of the TO peak towards a higher wavenumber in the Raman spectrum. As a result, a positive value of $\mathrm{tr}(\varepsilon)$ indicates compressive local strain, while a negative value represents tensile strain in the bonding network. The samples used for Raman study were grown on a *c*-Si substrate coated with a 300 nm-*a*-SiN_x membrane and 50 nm-thermal oxide. In our investigation, we only observed tensile local bond strain in our *a*-Si films.

3.3.5 Electron paramagnetic resonance

Dangling bond (DB) density (ρ_{DB}) was determined by electron paramagnetic resonance (EPR) spectroscopy. Measurements were made using a Bruker ELEXSYS E580 EPR spectrometer with an X-band ER 4123D CW-Resonator at 9.62 GHz, microwave power of 1.5 mW and magnetic-field modulation amplitude of 5 G. Spectra were obtained from 3375 to 3475 G. A bare *c*-Si substrate was used to determine the contribution from the substrate, and a KCl calibration standard was used to quantify the spin densities in the samples.

3.3.6 Positron annihilation doppler broadening spectroscopy

Doppler broadening spectroscopy (DBS) from positron annihilation in *a*-Si was performed by Marc Weber at Washington State University to obtain the average void size as a function of depth in *a*-Si. Samples were grown on *c*-Si with the native surface oxide left unremoved. During the measurements, the vacuum pressure was maintained below 10^{-7} Torr. The energy of the incident positron beam was adjusted within the range of 50 eV to 70 keV, corresponding to implantation depths in *c*-Si ranging from 1 nm to 15 μm. In this study, an energy of 25 keV

was used, yielding an implantation depth within the substrate of the films. The data analysis was limited to energies below 40 keV to avoid potential systematic errors caused by backscattered positrons annihilating from the walls of the steel vacuum chamber.

3.3.7 X-ray photoelectron spectroscopy

X-ray photoelectron spectroscopy (XPS) was used to study the chemical composition and bonding information of *a*-SiC. After Ar^+ ion sputtering to remove the native oxide layer on the sample surface, XPS spectra were obtained in a Perkin Elmer PHI 5600 XPS system with monochromated Al Kα excitation source, with a resolution of 0.025 eV and 200 ms per step, and a pass energy of 11.75 eV. The spectrum analysis of the chemical and bonding composition was carried out using MultiPak and CasaXPS software and the binding energies from Ref. 113 and 114.

3.3.8 Gentle nodal suspension

Mechanical loss was measured in a gentle nodal suspension (GeNS) system at room temperature. A fused silica substrate of 50 mm in diameter and 0.5 mm in thickness was first annealed and had its mechanical loss measured, so that the loss contribution from the fused silica substrate is minimized, and the influence of high T_s (or annealing temperature) on the loss of the substrate is negligible. A film of interest was then deposited on the substrate, and by knowing the film thickness and the elastic properties of the substrate, the mechanical loss of the film only can be extracted. The sample was excited in the frequency range of 0−25 kHz, and since there was no frequency dependence observed, the obtained values were averaged to obtain the loss angle ϕ, which is also the inverse of Q, the quality factor; $Q^{-1} = \frac{E_{dissipated}}{2\pi E_{stored}}$. This technique is described in more detail in the work of E. Cesarini et al. [115] and Li et al. [116]. The Young's modulus (E) and the Poisson's ratio (ν) of the deposited film can also be extracted from the GeNS measurements using an analytical model detailed in Ref. 117. The GeNS measurements were conducted by Gabriele Vajente at LIGO Laboratory, Caltech.

3.3.9 Double-paddle oscillators

Mechanical loss measurements between 0.3−110 K were performed by Liu et al. at the Naval Research Laboratory in Washington, using high purity *c*-Si double-paddle oscillators (DPO) [118]. The film of interest was deposited on the neck of the DPO. By comparing the ring-down time of the DPO's response, obtained

by exciting it at around 5500 Hz, before and after the deposition, the mechanical loss of transverse modes in the film can be determined. The mechanical loss of the deposited film is extracted using the following equation:

$$Q^{-1}(T) = \frac{G_{sub}t_{sub}}{3G_{film}t_{film}}(Q^{-1}_{total} - Q^{-1}_{bare}) \tag{3.3.2}$$

where G and t refer to the shear modulus and thicknesses of the substrate or DPO (sub) and sample ($film$), and T stands for the measurement temperature. G_{sub} is 62 GPa. The shear modulus of the film, G_{film}, is determined from the resonant frequency shift of the anti-symmetric mode before and after the film deposition.

The DPO measurement extends to room temperature. However, it has been shown that the thermoelastic loss of the c-Si substrate constitutes a significant portion of the background loss, making it difficult to accurately extract Q^{-1} near room temperature [57]. In contrast, GeNS is much less affected by the thermoelastic loss in the fused silica substrate, allowing for a more reliable determination of Q^{-1}_{RT} of the deposited film.

3.3.10 Photothermal common-path interferometry

Optical absorption of the films was measured by a technique called Photothermal common-path interferometry (PCI) at laser wavelengths of 1064 nm, 1550 nm and 2000 nm. Technical details are described in Ref. 119 and Appendix A. Experiments were performed by Ashot Markosyan at Stanford University, on samples grown on 1-inch diameter and 0.25-inch thick Corning 7980 and 7979 fused silica discs at room temperature.

CHAPTER 4

GAS PRESSURE EFFECTS ON PROPERTIES OF MAGNETRON SPUTTERED AMORPHOUS Si

4.1 Introduction

Various deposition techniques have been reported to prepare *a*-Si films [76,77,90–92]. The main difference is the energy of the incident Si atoms, which not only depend on the deposition technique, but also on the growth conditions, as discussed in Sec. 3.1. It is believed that the rigid, tetrahedral covalent bonding network of *a*-Si is the key to suppress formation of tunneling two-level systems, which explains its unusually low plateau loss at $1-10$ K in comparison to traditional glasses. Liu et al. attributed the first observation of lack of low-T excitation in HWCVD *a*-Si:H to hydrogen passivation of dangling bonds [76]. However, it was later shown by our group that hydrogen is not essential for removing TLSs in electron-beam evaporated *a*-Si [77]. It was then proposed by Queen et al. that the formation of TLSs is related to underconstrained, low-density regions with nano-scale defects [62, 63]. Molina-Ruiz et al. also reported a dependence of TLS density on atomic density of e-beam *a*-Si and suggested that nanovoids are associated with mechanical dissipation, while dangling bonds are responsible for dielectric losses [78].

Since previous studies have shown that a denser structure of *a*-Si is helpful in reducing nanovoids and TLS density, as well as improving the low-T loss [78,89], it gives motivation to deposit high-density *a*-Si films. In sputtering, film densification is achieved via energetic sputtered particles, described by the atomic peening effect [104,120]. One method to increase the kinetic energy possessed by the incoming atoms is to lower the working gas pressure. This chapter presents the first observation of overdense *a*-Si films produced through magnetron sputtering. The influence of deposition parameters, particularly the pressure of the working gas (Ar in this work), and post-growth heat treatment on the structure and mechanical loss of these high-density *a*-Si films is examined. Through the characterization of magnetron sputtered *a*-Si, we gained insights into the energy dissipation mechanisms at different temperature regimes, which provide valuable

guidance for optimizing deposition and treatment methods to reduce mechanical loss in a-Si.

4.2 Growth conditions

Amorphous silicon films were prepared by magnetron sputtering with a Si target of 99.999% purity, at a base pressure of $10^{-8}-10^{-7}$ Torr with the use of liquid nitrogen cold trap. Two substrate temperatures (T_s) were chosen, 50 °C, which corresponds to RT growth, and 360 °C. This study explored Ar pressures from 1.5 to 10.0 mTorr. 1.5 mTorr was the lowest Ar pressure to maintain a stable plasma for the Si gun. The growth rate varies from 0.30−0.65 Å/s.

4.3 Results

4.3.1 Atomic density and macroscopic strain

In general, as-deposited a-Si has a lower atomic density (ρ_{at}) than its crystalline couterpart; the atomic density of e-beam a-Si films grown at room temperature and 425 °C (blue dashed lines in Fig. 4.1) is 10.6% and 1.2% below c-Si density, respectively [89]. However, we found that by depositing a-Si films at RT and low Ar pressures (1.5 or 2.0 mTorr) using magnetron sputtering, higher film densities compared to c-Si (5.0×10^{22} at·cm^{-3}) were achieved, as illustrated in Fig. 4.1. The reported a-Si densities were up to 2.3% higher than c-Si densities. In contrast, when grown at high T_s, the films are underdense with a density close to that of c-Si density. Additionally, raising the substrate temperature narrowed the difference in density caused by changes in sputtering gas pressure.

Films deposited at 10.0 mTorr exhibit significantly lower densities compared to other samples. An interesting observation is the exceptionally high oxygen content (10−30 at.%) in the 10.0 mTorr films, whereas the other samples have less than 1 at.% oxygen (Table C.1). RBS spectra indicate that oxygen is uniformly distributed throughout the entire film, suggesting either in-situ oxidation during deposition or the presence of interconnected channels that facilitated oxygen diffusion post-growth. The percentage of Ar is below the detection limit (0.1 at.%) in all MS a-Si films, which indicates the absence of back-reflected gas neutrals in these samples.

To prevent oxidation after deposition, one sample was prepared with a 10 nm thick platinum capping layer. However, this sample still contained approximately

30 at.% oxygen. This observation may be attributed to the highly porous structure formed under high sputtering pressure, as such underdense films are more susceptible to impurity uptake during growth. Therefore, the physical properties of the Ar 10.0 mTorr samples were not further studied.

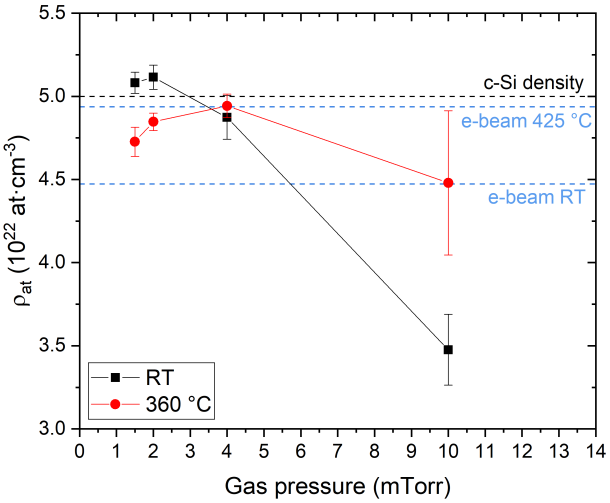

Figure 4.1: Atomic density of MS a-Si films under different deposition conditions in as-deposited (AD) and annealed forms. The atomic densities of c-Si and e-beam a-Si films [89] are represented by black and blue dashed lines, respectively.

Internal stress in MS *a*-Si films was obtained from the change in wafer curvature before and after deposition, and is shown in Fig. 4.2 (a). Given that the samples were deposited on *c*-Si wafers with a surface native oxide layer, and the thermal expansion of *a*-Si is similar to that of *c*-Si, the differential thermal contraction between the film and the substrate after high-T growth or annealing has minimal impact on the film stress (Sec. 3.2.1). MS *a*-Si films show compressive residual stress of 800 MPa when grown at 1.5 mTorr, tensile stress $\leq$100 MPa at 4.0 mTorr, and compressive stress $\sim$100 MPa at 10.0 mTorr. By raising T_s, the magnitude of the residual stress is reduced, with the largest discrepancy found in the two 1.5 mTorr samples. It should be noted that annealing also leads to a reduction in film stress in all samples, with a larger change in internal stress for films deposited at room temperature.

The macroscopic strain, obtained from the residual film stress shown in Fig. 4.2 (a) and analyzed as described in Sec. 3.3.3, is presented in Fig. 4.2 (b). The 10.0 mTorr samples were not included in the DPO measurements, and as a result, no information regarding their elastic properties was available. Therefore, the

macroscopic strain of the 10.0 mTorr samples is not presented. The MS a-Si films deposited at 1.5 mTorr has macroscopic compressive strain and are overdense, whereas a-Si films deposited at 4.0 mTorr exhibit tensile strain and are underdense, for both T_s. These findings are explained by the atomic peening effect: lower gas pressure allows atoms to reach the film growth surface with more energy (Fig. 3.3), resulting in denser films and compressive macroscopic strain [104, 120]. Figure 4.2 also shows that by increasing T_s or by annealing the samples, the magnitude of the macroscopic stress and strain is reduced.

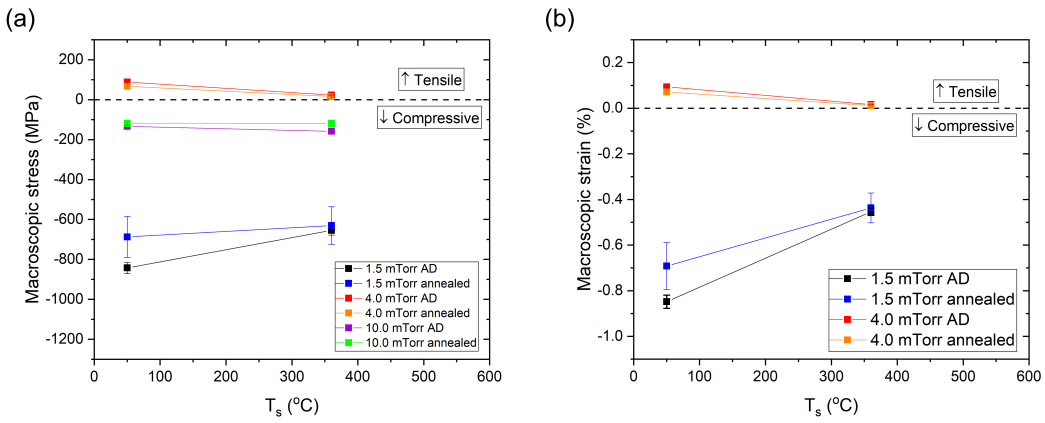

Figure 4.2: (a) Macroscopic stress in MS a-Si in as-deposited (AD) and annealed states as a function of substrate temperature (T_s) for different working gas pressures (1.5, 4.0 and 10.0 mTorr). (b) Macroscopic strain in MS a-Si in as-deposited and annealed states as a function of T_s for two working gas pressures (1.5 and 4.0 mTorr).

4.3.2 Bond angle deviation and local bond strain

As mentioned in Sec. 3.3.4, the structural information, including bond angle deviation and local strain in Si–Si bonds, is extracted from the TO peak of the Raman spectra of a-Si. Bond angle deviation ($\Delta\theta$) describes the dispersion of bond angle distribution in a-Si with respect to the tetrahedral bond angle, 109.5°, in c-Si. Figure 4.3 shows the dependence of $\Delta\theta$ on growth temperature, Ar pressure and annealing. For as-deposited films, $\Delta\theta$ does not vary much from 1.5 to 4.0 mTorr for a-Si deposited at RT, but a slight increase was seen in samples grown at 360 °C. When a sputtering pressure of 10.0 mTorr is used, $\Delta\theta$ experiences a noticeable decrease for both RT- and 360 °C-deposited a-Si. Increasing T_s reduces $\Delta\theta$, which is consistent with the findings in e-beam a-Si [89]. We notice that all MS a-Si films have higher $\Delta\theta$ than e-beam a-Si grown at similar temperatures. Even after annealing, the lowest $\Delta\theta$ achieved in MS a-Si is still higher than that in

e-beam a-Si (both achieved in high-T deposited samples).

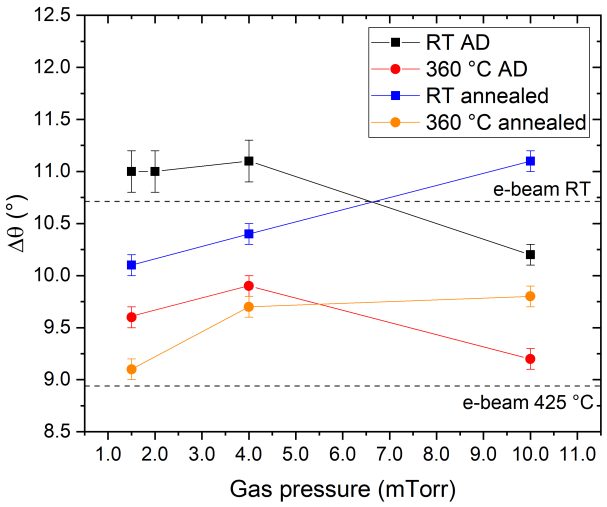

Figure 4.3: Bond angle deviation as a function of gas pressure of magnetron sputtered a-Si films grown at RT and 360 °C in as-deposited and annealed forms, with comparison to e-beam a-Si films grown at similar temperatures (dashed lines) [89].

The local strain of Si–Si bonds, tr(ε), for the same samples is shown as $\Delta\theta$ and is plotted in Fig. 4.4. The local bond strain is tensile for all MS and e-beam a-Si films, even though the macroscopic strain, which is planar in nature, is compressive for the MS films grown at 1.5 mTorr. It may seem counterintuitive, but compressive macroscopic strain means that in-plane bonds are compressed relative to out-of-plane bonds, however the in-plane and out-of-plane strain can both be tensile, compared to c-Si. Typical defects present in a-Si such as divacancies, nanovoids and columnar boundaries [63, 89, 121] will likely result in local tensile stress fields on all surrounding Si–Si bonds. Contrary to $\Delta\theta$, the bond strain shows rather consistent trends across all samples: tr(ε) increases with sputtering pressure but decreases with T_s.

The effect of annealing is different in $\Delta\theta$ and tr(ε); annealing causes $\Delta\theta$ to decrease for samples grown at 1.5 and 4.0 mTorr, tr(ε) increases or remains the same. However, the 10.0 mTorr samples show an increase in both $\Delta\theta$ and tr(ε) after annealing.

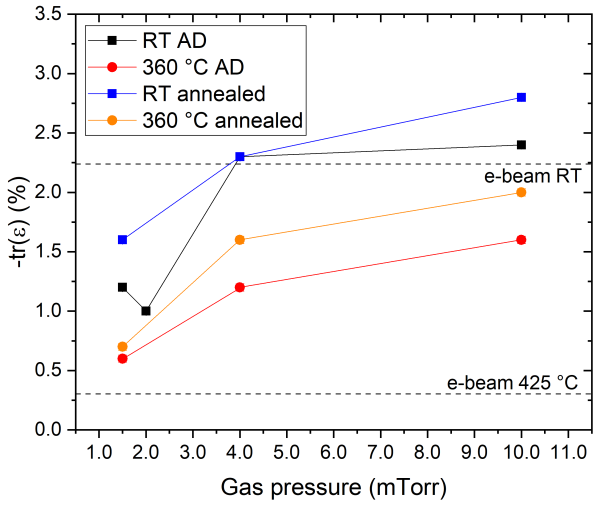

Figure 4.4: Local bond strain versus Ar pressure in MS a-Si grown at different T_s in their as-deposited and annealed states, in comparison to e-beam a-Si (dashed lines) [89].

4.3.3 Dangling bond density

The DB density (ρ_{DB}) of MS *a*-Si is shown in Table 4.1 and is around 10^{19} spins·cm^{-3}, which is nearly an order of magnitude higher than what has been previously reported in e-beam *a*-Si [89]. There is no significant dependence of ρ_{DB} on Ar pressure, growth temperature or annealing. The difference in ρ_{DB} of MS and e-beam *a*-Si can be attributed to the nature of the two deposition techniques. Sputtered atoms have much higher kinetic energy compared to thermally evaporated atoms when they reach the substrate, they cause knock-on collisions that lead to damage to the film structure and formation of dangling bonds.

4.3.4 Doppler broadening spectroscopy

Doppler broadening spectroscopy results indicate that in MS *a*-Si, deposited at Ar pressure of 1.5 mTorr, the open volume in the network is dominated by divacancies, instead of the nanovoids seen in e-beam *a*-Si [89]. The divacancy concentration of both RT- and 360 °C-deposited MS *a*-Si is $\sim 1.6 \times 10^{18}$ cm^{-3}. The presence of an equivalent divacancy concentration in both films, despite one being underdense and the other overdense, suggests that the overdense (RT-grown) sample likely contains self-interstitials, probably due to the atomic peening effect.

4.3.5 Mechanical loss

Figure 4.5 shows Q^{-1} measured by DPO from 0.3 to 110 K. Liu et al. [92] first demonstrated that higher T_s helps lower Q_0^{-1} of MS *a*-Si; while this is a significant effect, it is far smaller than the orders of magnitude improvement found in e-beam *a*-Si. Our results confirm that a reduction of up to 48% can be achieved by increasing T_s from RT to 360 °C. In addition, we found that sputtering pressure has a negligible impact on Q_0^{-1} of MS *a*-Si. Heat treatment is also not effective in improving low-T mechanical loss of *a*-Si films grown at high T_s; Q_0^{-1} remains at almost the same level before and after annealing the 360 °C, 1.5 mTorr *a*-Si sample.

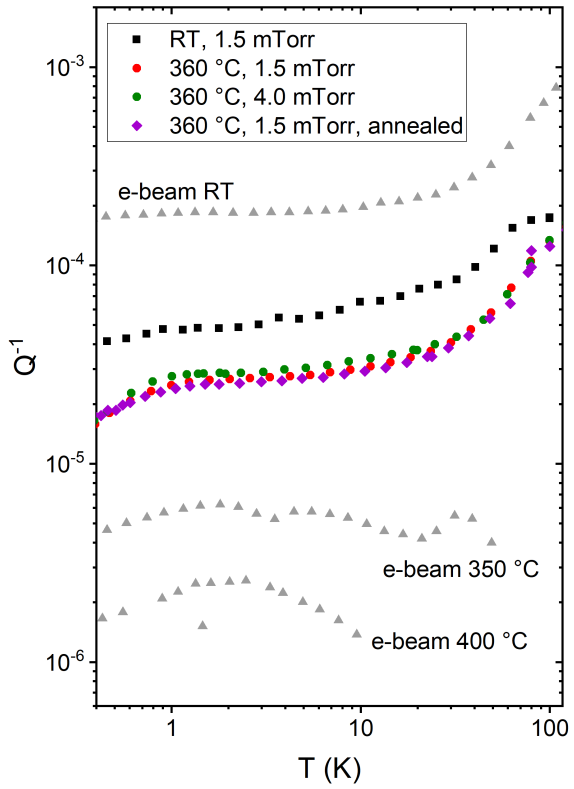

Figure 4.5: Mechanical loss of MS a-Si at low temperatures in their as-deposited and annealed states, compared to e-beam a-Si deposited at RT, 350 °C and 400 °C [77].

Table 4.1 compares the low-T loss reported in this work, with the Q_0^{-1} of *a*-Si made by other techniques [77, 90–92]. The lowest Q_0^{-1} seen in MS *a*-Si is on the same level as the *a*-Si grown using IBS and RLVIP [90,91]. E-beam *a*-Si, in comparison, exhibits a much lower Q_0^{-1} of 2×10^{-6} at 400 °C compared to the other PVD techniques; approximately a ten-times improvement in the mechanical loss

at cryogenic temperatures [77]. The DPO measurements at 300 K yielded the shear modulus at RT, as described in Sec. 3.3.9: 31.8 GPa for the RT, 1.5 mTorr AD *a*-Si, 46.1 GPa for the 360 °C, 1.5 mTorr AD *a*-Si, and 44.6 GPa for the 360 °C, 4.0 mTorr AD *a*-Si. These results indicate an increase in bond stiffness with higher T_s and lower Ar pressure.

The mechanical loss measured by GeNS at room temperature was averaged across various frequencies, as there was no frequency dependence. The weighted means are shown in Fig. 4.5 and Table 4.1. It can be seen that, to achieve a low Q_{RT}^{-1}, low sputtering pressure and a high T_s are required. The lowest RT loss, 1.12×10^{-4}, is observed in the *a*-Si film grown at 360 °C and 1.5 mTorr, which is about 1.9 times lower than that in e-beam *a*-Si, which is prepared at a similar T_s (425 °C) [95].

The influence of annealing on MS *a*-Si is also illustrated in Fig. 4.6. The RT mechanical loss is improved after annealing for the RT-deposited MS *a*-Si at 1.5 mTorr, and overall the lowest RT loss was achieved in this sample (8.5×10^{-5}). This loss is on the same level as the previously reported lowest Q_{RT}^{-1} in IBS *a*-Si (9.0×10^{-5}) [90]. Q_{RT}^{-1} of the sample grown at 360 °C and 1.5 mTorr remained at the same level after the heat treatment. This phenomenon is consistent with the effect of annealing in e-beam *a*-Si, where the Q_{RT}^{-1} of the RT-deposited sample is reduced to that of the 425 °C-deposited one after annealing [95]. Nonetheless, heat treatment yields a lower loss of 9.0×10^{-5} in the MS *a*-Si grown at 360 °C and 4.0 mTorr. Table 4.1 summarizes the mechanical loss of *a*-Si films prepared by various methods at 1 and 10 K and at room temperature.

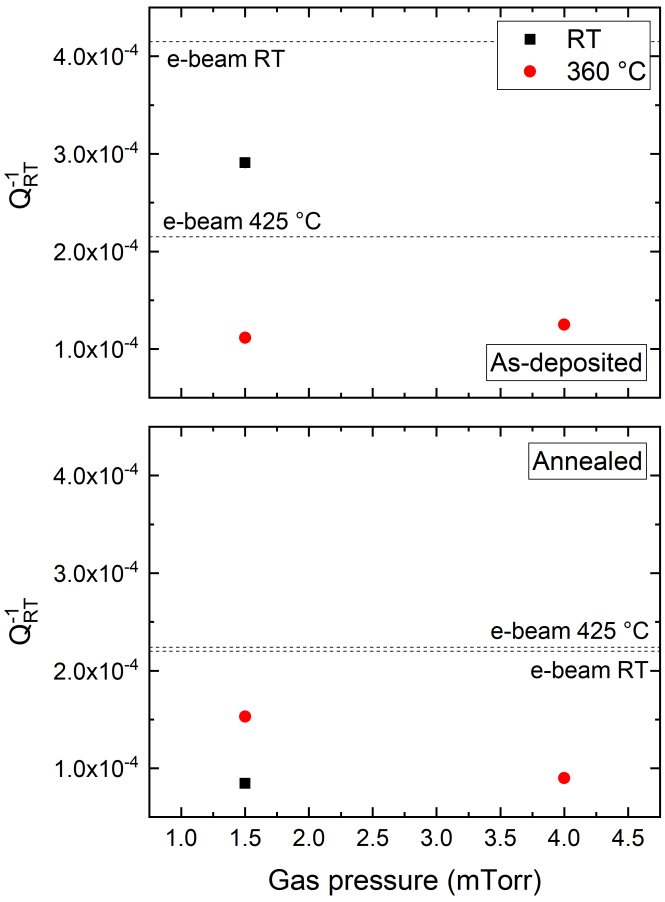

Figure 4.6: Room-temperature mechanical loss dependence of MS a-Si on Ar pressure in their as-deposited (top) and annealed states (bottom). Dashed lines are the RT mechanical loss of e-beam a-Si from Ref. 95.

Table 4.1: Comparison between PVD a-Si films grown by electron-beam evaporation (e-beam), magnetron sputtering (MS), ion-beam sputtering (IBS) and reactive low-voltage ion plating (RLVIP).

Deposition method	Growth conditions	ρ_{at} $\times 10^{22}$ cm^{-3}	$\Delta\theta$ $^\circ$	-tr(ε) %	ρ_{DB} $\times 10^{18}$ cm^{-3}	Q_0^{-1} (1 K) $\times 10^{-5}$	Q_0^{-1} (10 K) $\times 10^{-5}$	Q_{RT}^{-1} $\times 10^{-4}$
e-beam as-deposited [77, 78, 89, 95]	RT	4.47	10.7	2.2	4.3	18.4	19.7	4.2
	425 °C	4.94	8.9	0.3	2.8	0.2	0.1	2.2
	425 °C thin film[1]	4.87	9.5	0.7	2.4	2.1	1.6	
MS as-deposited	RT, 1.5 mTorr	5.08	11.0	1.2	20.0	4.8	6.5	2.9
	360 °C, 1.5 mTorr	4.73	9.6	0.6	17.5	2.5	3.0	1.1
	RT, 4.0 mTorr	4.87	11.1	2.3	13.5			
	360 °C, 4.0 mTorr	4.94	9.9	1.2	14.4	2.8	3.3	1.2
	RT, 10.0 mTorr	3.48	10.2	2.4	10.4			
	360 °C, 10.0 mTorr	4.48	9.2	1.6				
MS annealed	RT, 1.5 mTorr		10.1	1.6	20.4			0.8
	360 °C, 1.5 mTorr		9.1	0.7	14.7	2.4	2.9	1.5
	RT, 4.0 mTorr		10.4	2.3				
	360 °C, 4.0 mTorr		9.7	1.6	6.1			0.9
	RT, 10.0 mTorr		11.1	2.8				
	360 °C, 10.0 mTorr		9.8	2.0				
MS as-deposited [92]	RT, 3.0 mTorr	4.93				5.4	6.2	
	303 °C, 3.0 mTorr	4.94				2.9	3.5	
	370 °C, 3.0 mTorr	4.95				1.7	2.2	
	431 °C, 3.0 mTorr	4.98				1.4	2.0	
IBS annealed[2,3] [90]	RT						3.3	0.9
RLVIP as-deposited[2] [91]	250 °C						1.5	1.1
RLVIP annealed[2,3] [91]	250 °C							0.2

[1] Film thickness (60 nm) [78] is lower than the other two e-beam samples listed (∼300 nm) [77].

[2] The IBS and RLVIP a-Si films were prepared at thicknesses of 500 nm [90] and 1 μm [91], correspondingly, which are thicker than the MS samples in this work and Ref. 92, and the e-beam samples from Ref. 77, 78, 89, 95 (all around 300 nm).

[3] Heat treatment in Ref [90, 91] was done at 450 °C and 500 °C respectively, and performed in air. The resulted formation of SiO_2 might affect the measured properties. Direct comparisons might not be accurate.

4.4 Discussion

In this study, we used magnetron sputtering with various Ar pressures to investigate the effect of incident atom kinetic energy on the structure and properties of MS *a*-Si films and explore the optimal deposition conditions. The dependence of kinetic energy of sputtered Si atoms on the working gas and its pressure is discussed in Sec. 3.1. Our results show that compared to other sputtering-based techniques, such as IBS and RLVIP, MS *a*-Si exhibits similar loss behaviors at both cryogenic temperatures and room temperature (Table 4.1). However, the mechanical loss of the sputtered films behaves quite differently from e-beam *a*-Si; while Q_0^{-1} of MS *a*-Si exhibits only limited improvement with increased T_s, a reduction of 2 orders of magnitude in Q_0^{-1} with higher T_s was observed in e-beam *a*-Si. Moreover, the Q_{RT}^{-1} of MS *a*-Si is lower than that of e-beam *a*-Si at approximately the same T_s, and it exhibits a similar improvement in Q_{RT}^{-1} with higher T_s compared to e-beam *a*-Si (Fig. 4.5). A lower Ar pressure was found to have a slight reducing effect on Q_{RT}^{-1}. It is noteworthy that for both e-beam and MS *a*-Si, annealing the RT-deposited sample results in a similar Q_{RT}^{-1} to that of the high-T deposited sample, whereas for Q_0^{-1}, annealing is considerably less effective than growing at high T_s [95]. The annealed RT-deposited e-beam sample retains a significantly higher Q_0^{-1} value compared to the one deposited at a higher T_s of 425 °C, with the difference spanning approximately two orders of magnitude. These findings suggest that the mechanisms responsible for energy dissipation at low temperatures and at room temperature are distinct and are associated with different origins.

As discussed in Sec. 2.2, the plateau loss, Q_0^{-1} at 1 K, is directly proportional to the density of tunneling two-level systems, and several authors have investigated the structural origins of TLSs in *a*-Si [62,78,122]. Previous studies have reported that in e-beam *a*-Si, films exhibiting higher atomic density and fewer low-density regions, specifically nanovoids, demonstrate lower Q_0^{-1} [78, 89]. Based on these results, we were led to speculate that Q_0^{-1} might show a minimum at the *c*-Si density, with the absence of nanovoids. However, the findings of this study indicate that the relationship between Q_0^{-1} and ρ_{at} observed in previous research does not hold true for our samples. Take the MS RT, 1.5 mTorr *a*-Si, one of the overdense samples for example. It has a Q_0^{-1} that is over 10 times higher than the underdense e-beam 425 °C *a*-Si. Furthermore, samples with the same ρ_{at}, MS 360 °C, 4.0 mTorr *a*-Si and e-beam 425 °C *a*-Si, showed completely different low-T loss behaviors, with Q_0^{-1} values of 2.8×10^{-5} and 0.2×10^{-5}, respectively. These results imply that the formation of TLSs and energy dissipation at low temperatures in *a*-Si cannot be attributed to nanovoids alone.

Structural disorder, which is reflected in bond angle deviation, does not explain

the differences in Q_0^{-1} either. In general, e-beam *a*-Si shows a lower $\Delta\theta$ than MS *a*-Si grown at similar T_s and low gas pressures (Fig. 4.3). However, the Q_0^{-1} of MS RT, 1.5 mTorr *a*-Si is one tenth of that of e-beam *a*-Si grown at room temperature. In addition, the Q_0^{-1} of the annealed MS 360 °C, 1.5 mTorr sample is ten times higher than that of the e-beam 425 °C *a*-Si, despite having almost the same $\Delta\theta$.

We also observed that the variation in dangling bond density does not consistently correspond to the low-T loss behavior. For instance, in the case of the MS 360 °C, 1.5 mTorr sample, there was a decrease in ρ_{DB} after vacuum annealing, while its Q_0^{-1} remained almost unchanged (Table 4.1). In addition, the difference in Q_0^{-1} between MS and e-beam *a*-Si cannot be explained solely by their respective ρ_{DB} values. These findings suggest a lack of correlation between Q_0^{-1} and ρ_{DB}, consistent with previous observations by Molina-Ruiz et al. in e-beam *a*-Si films of various thicknesses [78].

Changes at the macroscopic level are a reflection of microstructural changes. The incident Si atoms in sputtering possess high kinetic energy, resulting in knock-on damage to the deposited film and potential penetration of the surface layer. Bombardment by high-energy particles in sputtering processes leads to compressive film stress (Fig. 4.2 (a)) and a more compact atomic packing, known as the atomic peening effect [104,120]. As discussed in Sec. 3.1, with higher Ar pressure, an increased number of collisions take place between sputtered Si atoms and Ar atoms. This higher collision frequency causes a decrease in the kinetic energy carried by sputtered Si atoms when they reach the substrate. This is reflected in the compressive-to-tensile transition in macroscopic strain when the Ar pressure is increased from 1.5 to 4.0 mTorr, as well as the smaller magnitude of macroscopic strain observed in the 4.0 mTorr samples. Furthermore, *a*-Si deposited at higher gas pressures exhibits a lower density compared to *c*-Si, indicating a less densely packed structure.

Due to the nature of the sputtering process, the predominant defects observed in MS *a*-Si are divacancies (two missing Si atoms) and self-interstitials (Sec. 4.3.4), contrasting with the nanovoids involving multiple missing atoms in e-beam *a*-Si. The impact of T_s on ρ_{at} is less prominent in MS *a*-Si grown at low Ar pressure (1.5−4.0 mTorr) than in e-beam *a*-Si. We propose that these defects create regions in which TLSs form, akin to the effect of nanovoids in e-beam *a*-Si: the MS RT, 1.5 mTorr *a*-Si exhibits a lower Q_0^{-1} compared to e-beam RT *a*-Si due to its denser film structure and fewer open-volume defects (divacancies/nanovoids) (higher ρ_{at}), but the Q_0^{-1} of MS *a*-Si grown at high T_s (300−430 °C) is significantly higher than that of e-beam *a*-Si grown at 300 and 400 °C, as suggested by Liu et al. [92] and confirmed by our results.

The narrow range in Q_0^{-1} of MS a-Si grown at different T_s and different Ar pressures corresponds to the small variations observed in bond angle deviation and local bond strain under different deposition conditions. In electron-beam evaporation, raising the substrate temperature leads to densification by eliminating nanovoids, resulting in a film structure of lower $\Delta\theta$ and tr(ε) [89]. Similarly, in magnetron sputtered samples, we observed a lower $\Delta\theta$ and a lower tr(ε) with higher T_s, but the changes are smaller. The influence of elevated T_s is weaker in MS a-Si compared to e-beam a-Si, on Q_0^{-1} and structural properties (ρ_{at}, $\Delta\theta$ and tr(ε)). The damage and defects accumulated during sputtering are likely embedded sub-surface in the sputtered film, making their removal challenging. The enhanced diffusion at higher temperatures, especially surface diffusion, is less effective in promoting structural relaxation and eliminating defects in MS a-Si, as these damages and defects are located deep within the film.

We turn now to the RT mechanical loss, which is lower for MS a-Si than e-beam a-Si for similar growth temperatures, as shown in Fig. 4.6. This phenomenon cannot be solely explained by any single property among those structural properties discussed earlier, including atomic density, bond angle deviation, local strain, or dangling bond density. We propose that the energy dissipation mechanism at room temperature is governed by the rigidity of the bonding network, rather than the regions surrounding individual defects. Network rigidity can be examined from two perspectives: the resistance of bonds to movement, characterized by bond stiffness, and the flexibility of individual atom movement, influenced by the arrangement of neighboring atoms and the presence of defects. Open-volume defects would provide more space for atomic movement, while self-interstitials would restrict it. Enhancing the network rigidity can be achieved by promoting the formation of a denser and more ordered structure, eliminating defects, particularly open-volume defects that allow for atomic movement, and facilitating structural relaxation at elevated substrate temperatures.

The shear modulus of MS a-Si, determined from DPO measurements serves as an indicator of the stiffness of Si–Si bonds. It exhibits an increase with higher T_s and lower gas pressure (Sec. 4.3.5), even though atomic density reduces. This behavior in MS a-Si can be attributed to two underlying factors. Firstly, low gas pressure results in higher incident atom energy, leading to film densification, as illustrated in Fig. 4.1. Secondly, elevated T_s induces structural reorganization, allowing the atoms to adopt lower energy configurations and strengthen the bonds, resulting in a higher G. The difference in bond stiffness provides an explanation for the RT loss performance of MS a-Si; among all the as-deposited MS a-Si films, the sample deposited at 360 °C and 1.5 mTorr exhibits the highest G and the lowest Q_{RT}^{-1} value.

The e-beam a-Si also shows a decreasing trend in Q_{RT}^{-1} with increasing G, similar to MS a-Si. The RT-deposited e-beam sample has a G of 35.6 GPa and a RT loss of 4.2×10^{-4}, and the 425 °C-deposited e-beam sample has a G of 61.1 GPa and a RT loss of 2.2×10^{-4} [95, 123]. However, comparing these results to those of MS a-Si, we find that the MS 360 °C, 1.5 mTorr a-Si has a lower G (46.1 GPa) than the 425 °C-grown e-beam a-Si, but a Q_{RT}^{-1} (1.1×10^{-4}) that is half of the 425 °C-grown e-beam a-Si. These findings suggest that bond stiffness alone does not fully account for the suppression of energy dissipation mechanism at RT. In addition to less stiff bonds, the availability of adjacent space is required for atomic movements to take place. The denser packing and absence of nanovoids in MS a-Si, induced by atomic peening, compared to e-beam a-Si, help suppress these activities that cause mechanical loss.

The effects of post-growth annealing were also investigated. It was found that annealing improves Q_0^{-1} of e-beam samples grown at RT, but does not affect the Q_0^{-1} of MS 360 °C-deposited a-Si (Fig. 4.5), and e-beam 425 °C-deposited a-Si. Moreover, the e-beam annealed RT-deposited a-Si still exhibits a Q_0^{-1} value that is approximately two orders of magnitude higher than that of the e-beam 425 °C-deposited a-Si [95]. In contrast, annealing the RT-grown sample has a similar impact on Q_{RT}^{-1} to depositing at high T_s in reducing Q_{RT}^{-1} in MS and e-beam a-Si (Fig. 4.6).

A major distinction between annealing and high T_s is that annealing primarily promotes bulk diffusion and defect coarsening, whereas during growth, surface diffusion is also promoted, which is a more efficient means to remove defects. One example is proton-irradiated silicon, where annealing above 250 °C leads to the clustering of divacancies into voids containing more than two missing atoms, as revealed by the decrease in the positron trapping rate associated with divacancies [124]. The observed agglomeration of divacancies in annealed proton-irradiated silicon explains the unexpected increase in local bond strain in MS a-Si after annealing, contrary to the results observed at high T_s. This increase in local bond strain is likely attributed to the coalescence of divacancies into voids during annealing. In addition, the reduction in $\Delta\theta$ of the MS Ar 1.5 and 4.0 mTorr films is smaller by annealing than by raising T_s. These phenomena suggest that annealing is less effective in removing existing defects in the structure. This explains why the same Q_0^{-1} is found in the MS 360 °C, 1.5 mTorr sample before and after annealing. The dissipation mechanism at room temperature, however, is determined by the bonding network and is suppressed by stronger bonds and enhanced structural order. Such improvements can be achieved through local atomic rearrangement facilitated by bulk diffusion, which requires short travel distances and small atomic movements. Hence, the enhancement of Q_{RT}^{-1} is inde-

pendent of the timing of heat application, whether during or after the deposition process, as the role of surface diffusion, which enables large length scale diffusion, is less important.

4.5 Summary

This chapter presented a systematic study of the effects of the pressure of working gas, Ar in this case, substrate temperature and annealing on the properties of magnetron sputtered *a*-Si films. Quantitative structural characterization and mechanical loss measurements were conducted, and the results were compared to *a*-Si films grown by other PVD techniques. The MS RT-deposited sample grown at 1.5 mTorr shows lower mechanical loss at cryogenic temperatures and room temperature than the e-beam RT-deposited *a*-Si, thanks to its denser structure. By growing at high T_s, mechanical losses at low temperatures and room temperature are further improved. Annealing is demonstrated to bring improvement to mechanical loss at room temperature, whereas its impact on Q_0^{-1} is not as prominent. We showed that the Q_{RT}^{-1} of the annealed MS RT 1.5 mTorr *a*-Si is lower than the lowest RT loss achieved in e-beam *a*-Si, and is approximately 65% lower than the currently used high-index material *a*-Ti:Ta_2O_5. However, the low-T mechanical loss of the high-T deposited MS *a*-Si is still $\sim$10 times higher than that of the high-T deposited e-beam *a*-Si.

We proposed that defects such as divacancies and self-interstitials in MS *a*-Si, along with nanovoids in e-beam *a*-Si, contribute to the formation of TLSs and the dissipation of energy at low temperatures through tunneling events between TLSs. The network rigidity, characterized by bond stiffness and ease of atomic movement, is related to dissipation mechanisms at room temperature. Given the promising mechanical loss results and strong dependence on deposition conditions for *a*-Si, further optimization of PVD process parameters may lead to even better performance as a mirror coating material for GW detectors operating at cryogenic temperatures and at ambient temperature.

CHAPTER 5

ROLE OF WORKING GAS ON FILM PROPERTIES OF SPUTTERED AMORPHOUS Si

5.1 Introduction

It was recognized quite early that structural and physical properties of films grown by sputtering depend on the working gas, as the momentum transfer efficiency is related to the mass ratio of the gas ion and the sputtered atom. As discussed in Sec. 3.1, it was shown that changing both the working gas and its pressure has a strong influence on the kinetic energy of sputtered Si atoms. Previously we have explored a range of Ar pressure to deposit *a*-Si in a magnetron sputtering system (Chapter 4). Low gas pressure (1.5 mTorr) was found to promote densification in as-deposited films and lead to lower mechanical loss at both cryogenic temperatures and room temperature. We proposed that the observed improvement is associated with the higher kinetic energy possessed by incident Si atoms when arriving at the substrate. Energetic adatoms play a role in reducing the presence of open-volume defects, i.e. divacancies in MS *a*-Si. This leads to a denser structure and a more rigid bonding network, which in turn suppresses energy dissipation mechanisms. Therefore, we were motivated to explore a broader range of incoming particle energy by changing the working gas and examine its influence on the film structure and physical properties of MS *a*-Si. In this chapter, a systematic study on *a*-Si deposited using neon, argon, krypton and xenon, and a discussion on the influence of adatoms' kinetic energy on the film structure and its subsequent effects on mechanical properties of MS *a*-Si are presented.

5.2 Growth conditions

The *a*-Si films were grown by magnetron sputtering of a Si target (99.999% purity), in a vacuum of 10^{-8}–10^{-7} Torr. In accordance with the findings presented in Chapter 4, where it was demonstrated that a higher substrate temperature contributes to enhanced structural order and reduced mechanical loss at low

temperatures and room temperature, T_s was maintained at 360 °C for all samples studied in this research. The lowest gas pressure that stabilizes the plasma was chosen; for Ar and Kr, this pressure was 1.5 mTorr; for Xe, it was 0.5 mTorr; and for Ne, it was 11−18 mTorr. The system was set to constant gun power mode, allowing for automatic adjustment of gun voltage and discharge current. Detailed information on parameters of the sputtering gun and growth rate is shown in Table 3.1. We noticed that the discharge current becomes lower with heavier sputtering gas. A fourfold difference exists across the discharge current of different gases. While it is expected that heavier sputtering gases would result in fewer Si atoms being sputtered away from the target, due to a lower sputtering yield [101], the growth rate does not directly correlate with the atomic weight of working gas. This is because the number of Si atoms reaching the substrate is also influenced by collisions with gas atoms in the chamber.

5.3 Results

5.3.1 Atomic density

The atomic density extracted from RBS spectra is plotted against the atomic weight of working gas in Fig. 5.1 and is also shown in Table 5.1. Reflected gas is below detection limit (0.1 at.%) in all films, except for the one prepared with Ne, which has gas inclusion of ∼2 at.% at high sputtering pressure (11.0 mTorr). The oxygen content is less than 0.5 at.% for films deposited with Ar, Kr and Xe, whereas the Ne-deposited sample has an oxygen content of approximately 6 at.%. The low ρ_{at} and high oxygen content seen in the Ne 11.0 mTorr and Ar 10.0 mTorr *a*-Si (Sec. 4.3.1) indicate that when using high gas pressure during deposition, a significant number of vacancies/voids are formed within the film. These open-volume defects create rapid diffusion pathways for oxygen, making the film more vulnerable to oxidation when exposed to the atmosphere.

With Ar, Kr and Xe, the atomic density of MS *a*-Si does not show significant variation with the choice of working gas. Only a slight increase in ρ_{at} is observed when transitioning from Ar to Xe. The density of the *a*-Si films deposited using Xe at 0.5 and 1.5 mTorr does not exhibit any noticeable difference. It should be noted that none of the studied samples in this chapter exhibit an overdensity, which was seen in the *a*-Si deposited with Ar at 1.5 and 2.0 mTorr at room temperature, as reported in Sec. 4.3.1.

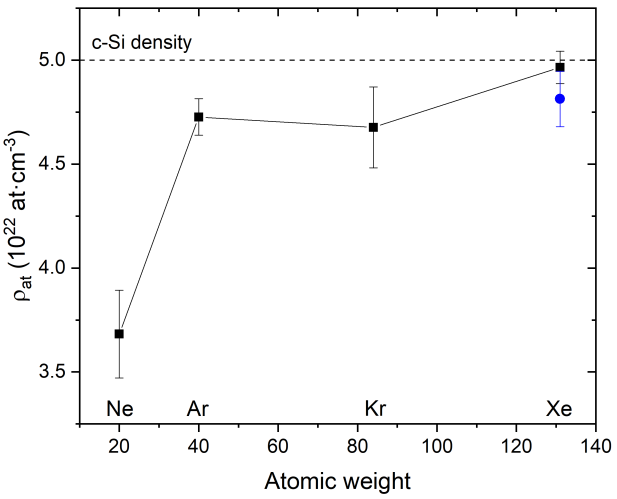

Figure 5.1: Dependence of atomic density of a-Si deposited at 360 °C on atomic weight of working gas: Ne - 20, Ar - 40, Kr - 84, Xe - 131. The gas pressure for Ne is 11.0 mTorr and for Ar, Kr and Xe is 1.5 mTorr. The blue circle indicates the density of Xe 0.5 mTorr deposited a-Si. The density of c-Si (5.0×10^{22} atoms·cm^{-3}) is added for reference (dashed line).

5.3.2 Bond angle deviation and local bond strain

Raman spectroscopy study reveals the local ordering in the *a*-Si network. The two structural parameters extracted, $\Delta\theta$ and tr(ε), are plotted in Fig. 5.2. The influence of gas weight on the structure of MS *a*-Si is evident; heavier sputtering gas promotes a more ordered atomic arrangement, as indicated by the smaller deviation in bond angle. The local bond strain in all films remains tensile and does not exhibit a consistent trend with the weight of the working gas. We also measured the MS Xe 0.5 mTorr *a*-Si and found that it has the same Raman response as the Xe 1.5 mTorr sample.

5.3.3 Dangling bond density

Figure 5.3 illustrates the variation in dangling bond density for MS *a*-Si films deposited using different gases. The observed changes in ρ_{DB} remain within a narrow range compared to the difference between MS and e-beam *a*-Si, which is approximately one order of magnitude (Table 4.1). The maximum difference observed is about twofold. No correlation is seen between ρ_{DB} and either the atomic weight of the sputtering gas or the working gas pressure. The DB density

Working gas		ρ_{at} $\times 10^{22}$ at·cm^{-3}	ρ_{DB} $\times 10^{18}$ spins·cm^{-3}	G GPa
Ne	11.0 mTorr	3.68 ± 0.21	8.4 ± 1.0	
Ar	1.5 mTorr	4.73 ± 0.09	17.5 ± 1.0	46.1
	4.0 mTorr	4.94 ± 0.07	14.4 ± 0.8	44.6
Kr	1.5 mTorr	4.68 ± 0.19	12.7 ± 1.4	45.3
Xe	0.5 mTorr	4.81 ± 0.13	12.8 ± 1.3	48.3
	1.5 mTorr	4.97 ± 0.08	16.4 ± 1.7	48.2

Table 5.1: Atomic density, dangling bond density and shear modulus extracted from DPO measurements.

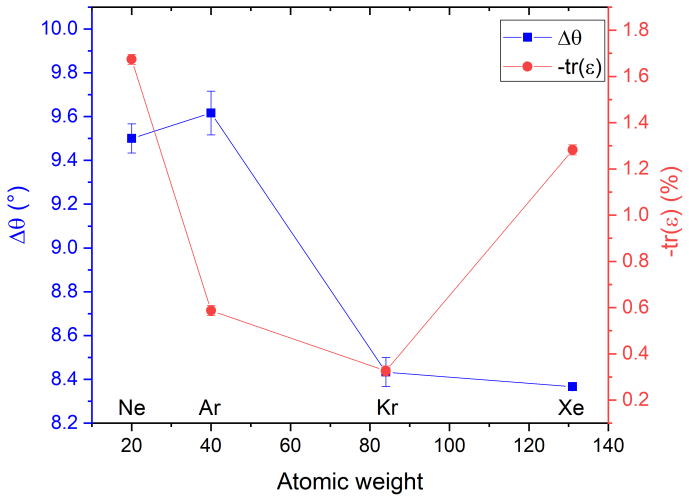

Figure 5.2: Bond angle deviation ($\Delta\theta$) and trace of strain in local bonding ($tr(\varepsilon)$) extracted from Raman spectrum of MS a-Si deposited using different working gases (sputtering pressure: 1.5 mTorr, Ne: 11.0 mTorr).

data is also listed in Table 5.1.

5.3.4 Mechanical loss

Four *a*-Si samples were prepared on DPO substrates for subsequent measurements. Figure 5.4 shows the mechanical loss of *a*-Si films from 0.3 to 110 K. Changing the working gas from Ar to Kr led to a small reduction in Q_0^{-1}, while there was no improvement observed with heavier gas, Xe, at the same pressure, 1.5 mTorr. In Ar-deposited samples, a similar Q_0^{-1} was observed for films grown

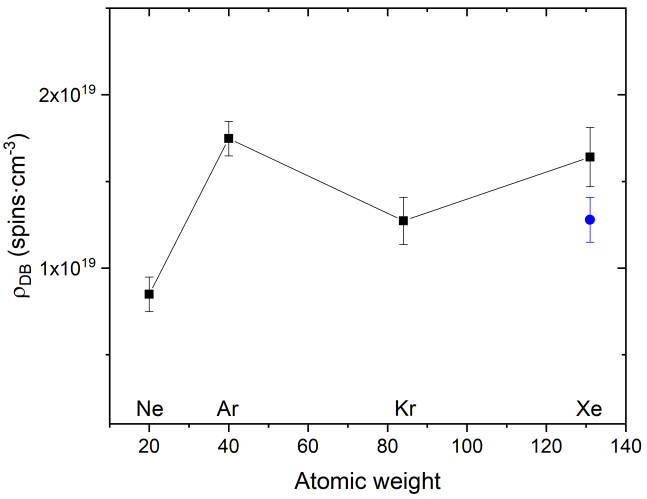

Figure 5.3: Dangling bond density of MS a-Si prepared by different gases. The working gas pressure was 11.0 mTorr for Ne, and 1.5 mTorr for the other gases. The blue circle indicates the ρ_{DB} of the Xe 0.5 mTorr sample.

at 360 °C, 1.5 mTorr and 4.0 mTorr. In contrast, a significant decrease in Q_0^{-1} was seen when the Xe pressure was reduced from 1.5 to 0.5 mTorr, likely related to a larger increase in incident atom kinetic energy than that between Ar 4.0 and 1.5 mTorr (Fig. 3.3). The lowest Q_0^{-1} is obtained in the Xe-sputtered *a*-Si at 0.5 mTorr, which is 8.0×10^{-6} at 1 K and 1.2×10^{-5} at 10 K. Although the MS 360 °C, Xe 0.5 mTorr *a*-Si shows the lowest Q_0^{-1} compared to other sputtered samples, including those obtained through IBS and RLVIP techniques [90, 91], the difference in loss between the MS Xe-deposited *a*-Si and e-beam *a*-Si is still approximately four times at 1 K and over one order of magnitude at 10 K [77] (Table 4.1).

The mechanical loss at room temperature, obtained from GeNS measurements, of MS *a*-Si using different gases is presented in Fig. 5.5. The significant reduction seen in Q_{RT}^{-1}, over a factor of 6, when switching from Ne to heavier gas is likely attributed to the porous film structure resulting from the high Ne pressure employed during deposition. From Ar to Xe, increasing the atomic weight of working gas brought slight improvement in Q_{RT}^{-1}; the RT loss is lowered by 20% if Xe is used to sputter Si atoms instead of Ar at 1.5 mTorr. Decreasing the gas pressure in the case of Xe however, does not lead to further improvement in Q_{RT}^{-1}. The lowest RT loss, 8.9×10^{-5}, is found in the film grown using Xe at 1.5 mTorr, which is comparable to the previously reported lowest value among sputtered *a*-Si films, in annealed IBS *a*-Si (9.0×10^{-5}) [90], and in annealed MS

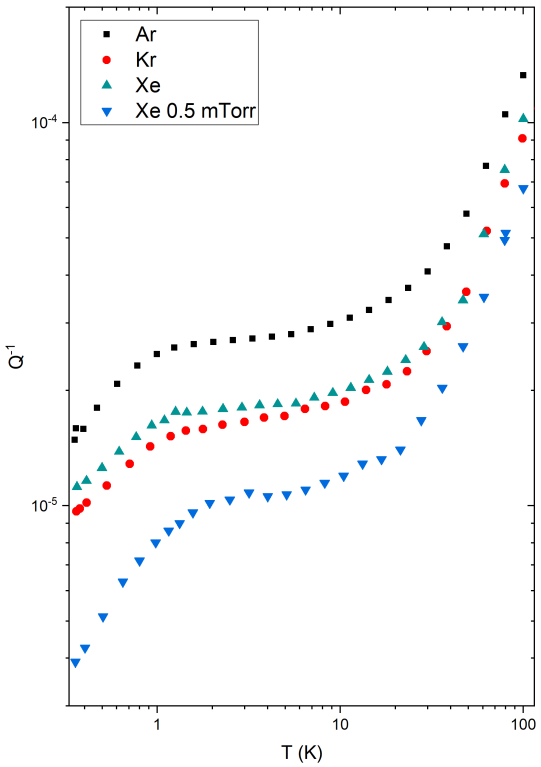

Figure 5.4: Low-temperature mechanical loss of MS a-Si prepared using Ar, Kr and Xe. Ar- and Kr-deposited samples were prepared at 1.5 mTorr. Two gas pressures were attempted for Xe: 0.5 and 1.5 mTorr to investigate the lowest attainable loss in MS a-Si.

RT, Ar 1.5 mTorr *a*-Si (8.5×10^{-5}) (Sec. 4.3.5). A summary of Q^{-1} at various temperatures is provided in Table 5.2. The shear modulus extracted from DPO measurements is listed in Table 5.1.

5.4 Discussion

The relationship between the kinetic energy of incident Si atoms and the atomic weight of the sputtering gas is discussed in Sec. 3.1. It is explained that the larger the difference in atomic weight between the working gas and the target atom, the lower the efficiency of momentum transfer, resulting in lower kinetic energy pos-

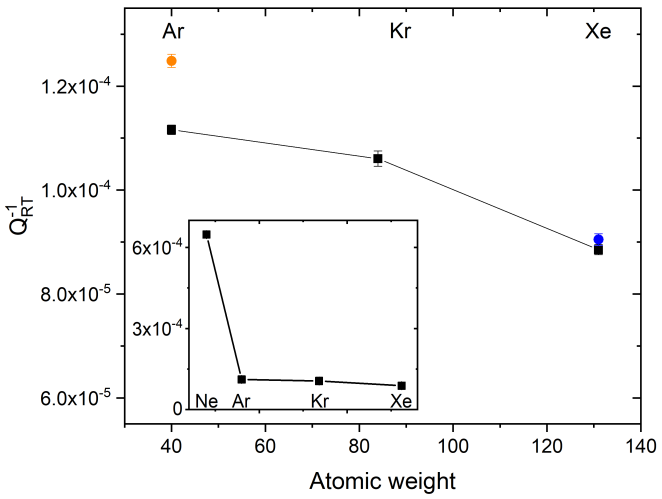

Figure 5.5: Room-temperature mechanical loss dependence of MS a-Si on atomic weight of working gas. Ne-deposited a-Si (insert) was prepared at 18.0 mTorr. The orange circle stands for the RT loss of Ar 4.0 mTorr deposited a-Si and the blue data point represents the loss of a-Si deposited using Xe at 0.5 mTorr.

Growth conditions	Q^{-1} ($\times 10^{-5}$)		
	1 K	10 K	300 K
Ne 18.0 mTorr			64.7±0.4
Ar 1.5 mTorr	2.5	3.0	11.2±0.1
Kr 1.5 mTorr	1.4	1.9	10.6±0.1
Xe 0.5 mTorr	0.8	1.2	9.0±0.1
Xe 1.5 mTorr	1.7	2.0	8.9±0.1

Table 5.2: Mechanical loss of MS a-Si at a substrate temperature of 360 °C, using different gases and sputtering pressures.

sessed by the sputtered atoms when leaving the target (Eq. 3.1.1). Nonetheless, these sputtered atoms experience less energy loss in subsequent collisions with gas atoms in the chamber before reaching the substrate surface (Eq. 3.1.4). Figure 3.3 demonstrates that $E''_{k,Si}$ increases with higher atomic weight of the sputtering gas and lower gas pressure. For Ar at 1.5 mTorr, Kr and Xe, the resulting $E''_{k,Si}$ is significantly higher than the average thermal energy at room temperature (∼25 meV). In contrast, for Ne and Ar at 4.0 mTorr, the sputtered Si atoms are thermalized (Table 3.1), and the impact with the substrate upon arrival is expected to be minimal.

When energetic atoms collide with the substrate surface during deposition, they can displace surface atoms and cause local bonding distortions, resulting in atomic peening. The knock-on damage caused by the impingement of these energetic particles forces atoms to move from their initial configurations to energetically unfavorable positions. Deposition at elevated T_s, coupled with the excess kinetic energy of the incident atoms, promotes diffusion. The knock-on damage may be eliminated through this enhanced diffusion as the displaced atoms migrate to neighboring sites and adopt a more energetically favorable configuration. This process is analogous to the cold working and annealing processes used to treat metals. Collisions with the film surface and underlying layers induce the creation of defects, which serve as a driving force for structural reorganization, similar to the dislocations generated in cold working of metals. When heat treated, a more organized structure with reduced defect density is formed.

With heavier working gas, we saw a higher atomic density (Fig. 5.1) and a reduction in structural disorder, measured by $\Delta\theta$ (Fig. 5.2). The improvement in structural order is expected from a higher $E''_{k,Si}$ with increasing atomic weight of working gas, but the plateauing of $\Delta\theta$ in Kr- and Xe-deposited a-Si, as well as the plateauing of ρ_{at} in Xe-deposited samples at 0.5 and 1.5 mTorr suggest that there is an interplay between atomic peening-induced damage and structural relaxation. As the incident energy continues to increase, only part of the damage undergoes recovery through diffusion, subject to the competition between the rate of defect creation by incoming atoms (deposition rate) and the diffusion rate at a given T_s. In addition, elimination of sub-surface defects, such as divacancies and self-interstitials, created via atomic impingement is very difficult, as it requires either diffusion to the film surface or occupation of nearby vacant atomic sites. The incomplete recovery of the structure is also evident in the higher local strain observed in Si–Si bonds when Xe is employed as the sputtering gas (Fig. 5.2). This explains why further increasing $E''_{k,Si}$ by manipulating the deposition parameters has a marginal effect on the structural improvement and film densification in MS a-Si.

The low-temperature mechanical loss experienced a noticeable improvement from Ar to Kr (big change in $E''_{k,Si}$ from Ar to Kr at 1.5 mTorr), but remains unchanged from Kr to Xe (much smaller change in $E''_{k,Si}$ from Kr to Xe) (Fig. 5.4). As previously discussed, the TLS density in a-Si, which is directly proportional to Q_0^{-1} (Eq. 2.2.6), is associated with various defects within the network, including nanovoids [62, 63, 78, 89], divacancies and self-interstitials (Sec. 4.4). The observed decrease in Q_0^{-1} when transitioning from Ar to Kr is consistent with the denser packing and reduced defect density, as reflected in a smaller $\Delta\theta$ in the film when using heavier sputtering gases. However, when changing from Kr to Xe, similar Q_0^{-1} was found in the 1.5 mTorr samples, which might be explained

by the partial recovery of the damage generated during growth. Nonetheless, a significant reduction of over 50% in the low-T loss was found in the Xe 0.5 mTorr sample, compared to the Xe 1.5 mTorr sample. This differs from that seen in MS 360 °C, Ar 1.5 and 4.0 mTorr *a*-Si, where no significant improvement in Q_0^{-1} was observed (Fig. 4.6). The absolute value of the difference in kinetic energy of the sputtered Si atoms between Xe pressures of 0.5 and 1.5 mTorr is more than 10 times greater than that between Ar pressures of 1.5 and 4.0 mTorr, as shown in Table 3.1. It is likely that the higher $E''_{k,Si}$ with Xe at 0.5 mTorr is sufficient to significantly reduce the density of open-volume defects in the deposited film, ultimately suppressing TLS formation and thus the mechanical loss at low temperatures.

Despite the MS 360 °C, Xe 0.5 mTorr sample showing the lowest Q_0^{-1} among sputtered *a*-Si, its loss is still approximately four times higher than that of e-beam 400 °C-deposited *a*-Si [77]. This significant difference in loss can potentially be attributed to the deposition processes. Sputtering, being a more energetic deposition method, can introduce defects beneath the film surface that may require bulk diffusion for their elimination. In electron-beam evaporation, the adatoms remain on the surface, and high growth temperature allows for fast surface diffusion of these adatoms, which leads to the formation of a near-full-density structure with a low defect density and as a result, a low TLS density and Q_0^{-1}.

Different from what was seen in the low-T loss, the room-temperature mechanical loss exhibited a slight reduction with increasing atomic weight of the sputtering gas, while no change was observed when reducing the Xe pressure from 1.5 to 0.5 mTorr (Fig. 5.5). In Chapter 4, it has been proposed that the RT loss mechanism in *a*-Si is associated with thermal activation over an energy barrier, which is influenced by bond stiffness and atomic movement flexibility within the network. This also provides an explanation for the RT loss of the samples studied here, where lower Q_{RT}^{-1} values are found in samples with higher shear modulus, except for the Kr-deposited sample (Table 5.1).

The competition between defect creation and removal rates, however, appears to result in a plateau in Q_{RT}^{-1} when the kinetic energy of incident Si atoms is increased with heavier working gas (Kr to Xe), and lower gas pressure (Xe 1.5 to 0.5 mTorr). This is consistent with the trends found in ρ_{at} (Fig. 5.1) and $\Delta\theta$ (Fig. 5.2). The improvement in RT loss brought by structural rearrangement is offset by the generation of more defects and the formation of weak bonds in their vicinity due to incoming atom impingement. One sign is the high local bond strain observed in the Xe-deposited samples, which indicates the incomplete removal of defects and the resulted strain in surrounding bonds. As a consequence, the RT loss reaches a limit with higher $E''_{k,Si}$.

This limitation is further demonstrated by the comparable levels of the lowest Q_{RT}^{-1} achieved in both MS and IBS a-Si films. In IBS, the sputtered Si atoms generally have higher kinetic energy at the substrate than in MS, due to higher ion beam energy and much lower gas pressure in the chamber. However, despite this difference, both IBS and MS a-Si films exhibit similar Q_{RT}^{-1} values, approximately 9×10^{-5} (Table 5.2). These results highlight the limitation of increasing incident atom kinetic energy in sputtering techniques for lowering the RT mechanical loss.

5.5 Summary

This chapter presented the results of depositing magnetron sputtered a-Si using different working gases and discussed their influence on the structural and mechanical properties of MS a-Si. The objective of using different gases is to explore a wider range of kinetic energy for the sputtered Si atoms. We found that when heavier working gas was used, there was densification in the a-Si films and an improvement in structural order, attributed to the atomic peening effect resulting from higher incident atom kinetic energy. However, a limit was observed. The mechanical loss at room temperature decreases as the atomic weight of the working gas increases at the same pressure of 1.5 mTorr, but eventually reaches a plateau, consistent with the trend observed in $\Delta\theta$. These findings confirm the previously discussed mechanisms for RT mechanical loss in Chapter 4, where suppressing energy dissipation at RT requires a densely packed structure with a rigid bonding network.

Reducing the Xe pressure from 1.5 to 0.5 mTorr had almost no impact on Q_{RT}^{-1} but unexpectedly caused a noticeable decrease in Q_0^{-1}. The Xe 0.5 mTorr sample exhibited the lowest plateau loss of 8.0×10^{-6} reported for sputtered a-Si. Higher kinetic energy, whether achieved through a higher atomic mass working gas or lower working gas pressure, is beneficial and shows no indication of an upper limit for this effect. This conclusion has significant implications for future research on a-Si using other PVD techniques, particularly ion-beam sputtering. In IBS, gas ions are directed toward the target, and they are largely distinct from the trajectory of the sputtered atoms, resulting in higher kinetic energy overall. By carefully selecting the appropriate working gas, such as Ne or Ar, to maximize momentum transfer from gas ions to Si atoms, and utilizing high accelerating voltages in conjunction with high-T deposition, it is possible to enhance the cryogenic temperature loss performance of a-Si even further.

CHAPTER 6

IMPROVING THE PROPERTIES OF AMORPHOUS Si VIA HYDROGENATION

6.1 Introduction

Hydrogenated amorphous silicon (*a*-Si:H) has been intensively studied for applications in optoelectronic, photonic and photovoltaic devices [125–127]. Hydrogen is crucial for suppressing carrier recombination and improving Si device performance. Two methodologies of hydrogenation of *a*-Si films have been explored in the past: in-situ hydrogenation (in-situ H), which incorporates hydrogen during film growth, and post-hydrogenation (post-H), which is a post-growth treatment that allows the diffusion or implantation of hydrogen atoms into the prepared *a*-Si films. For *a*-Si:H deposited by plasma-enhanced chemical vapor deposition (PECVD) and hot-wire chemical vapor deposition (HWCVD), manipulation of deposition parameters like pressure, substrate temperature, precursor gas silane/H_2 ratio etc., enables the fabrication of films with desired hydrogen content and properties [128–130]. In addition, hydrogen can be introduced after growth, via hydrogen plasma treatment [131], or annealing in forming gas (N_2/5% H_2). PVD *a*-Si:H films have also demonstrated improved physical properties, including band gap and minority carrier lifetime [132, 133], refractive index and optical absorption spectrum [82, 132, 134].

Hydrogen exists in various forms within *a*-Si films. In HWCVD *a*-Si:H, nuclear magnetic resonance spectroscopy revealed that the local hydrogen environment comprises primarily bonded Si–H and secondarily molecular hydrogen (H_2), found in both clustered and isolated states [135]. In RF sputtered *a*-Si:H films, Touir et al. identified isolated Si–H, responsible for the absorption band at 2004 cm^{-1} (4990 nm) in infrared absorption, and Si–H_2 groups, absorbing around 2086 cm^{-1} (4794 nm) [136]. They found that the Si–H_2 groups are located within voids present in the amorphous network. Annealing at elevated temperatures causes the hydrogen to redistribute (at approximately 100−200 °C [130]) and may induce irreversible changes (at around 250 °C) and lead to H_2 formation [137].

It is widely believed that H passivation of dangling bonds is responsible for improved physical properties of *a*-Si:H [138]. In addition to DB passivation, simulation work has shown that hydrogen induces structural reorganization in *a*-Si by lowering the energy barrier for the relaxation process [83–85]. It was proposed by Sriraman et al. that H insertion into strained Si–Si bonds leads to chemical annealing of *a*-Si, and removes these strained bonds through local atomic movements [83,85]. The hydrogen atom either remains bonded to one of the Si atoms, or leaves and diffuses through the network afterwards [84].

As discussed in Sec. 2.4, *a*-Si has demonstrated its potential as a high-index reflective layer in dielectric mirror coatings used in interferometric GW detectors. This is attributed to its high refractive index [91,96], as well as its low mechanical loss at cryogenic temperatures [77] and room temperature (Ref. 90, Chapter 4 and 5). However, *a*-Si has a significantly higher optical absorption than the current high-index layer, *a*-Ti:Ta_2O_5, particularly at the operating wavelength 1064 nm. A multimaterial design proposed by Steinlechner et al. [97] strategically places highly absorbing *a*-Si layers deeper within the coating stack, which mitigates the absorption problem and would reduce the overall mechanical loss of the stack since *a*-Ti:Ta_2O_5 has much higher mechanical loss.

Molina-Ruiz et al. has demonstrated that post-hydrogenation of e-beam *a*-Si grown at room temperature reduces the absorption at 2000 nm to below 10 ppm, which is a significant step towards meeting the ppm-level requirement for GW applications that use this longer wavelength (e.g. LIGO Voyager and Einstein Telescope, and other potential cryogenic detectors) [95]. However, the sample deposited at 425 °C, the one that shows the lowest low-T mechanical loss, exhibited only minimal change in absorption after post-H. The RT mechanical loss demonstrated limited improvement in both e-beam RT- and 425 °C-deposited samples after post-H, irrespective of the deposition temperature. This suggests that photon absorption, especially sub-band gap absorption at the relevant infrared wavelengths for GW detectors, which involves Urbach tail and defect-created mid-gap states (as discussed in Sec. 1.3.1), and mechanical energy dissipation arising from material anelasticity, are related to distinct mechanisms and structural features in *a*-Si:H, warranting further investigation.

This chapter reports on *a*-Si:H films prepared using magnetron sputtering and hydrogenated during and/or after deposition. The optical absorption of MS *a*-Si:H was investigated at three infrared wavelengths: 1064 nm, which is utilized in the current LIGO detectors, and 1550 nm and 2000 nm, proposed for use in the next-generation cryogenic GW detectors, in order to reduce the absorption in the *c*-Si mirror substrate. Their RT mechanical loss was also investigated. Our results show that passivation of dangling bonds does not have significant contri-

bution towards the observed improvement in optical and mechanical properties in *a*-Si:H. Instead, we propose that the presence of hydrogen, acting as a catalyst, facilitates local rearrangement of atoms and removes strained Si–Si bonds that are responsible for sub-band gap absorption and dissipative mechanisms.

6.2 Experimental details

a-Si and *a*-Si:H films were prepared with pure Ar, and Ar/10% H_2 mixture gas respectively. For in-situ hydrogenation, pure Ar was introduced from the chamber's bottom, while the Ar/H_2 gas mixture flowed through the injection holes positioned above the substrate plate. To achieve 5% and 10% H_2 in the working gas, we individually adjusted the flow rates of pure Ar and Ar/H_2 gas to 5 and 5 sccm, and 0 and 10 sccm, respectively. The combined flow rate was kept at 10 sccm, and the gas pressure was maintained at 1.5 mTorr (Sec. 3.1). The base pressure was around $1-2\times10^{-8}$ Torr after the usage of liquid nitrogen trap, and T_s was RT and 360 °C.

Post-growth treatments included vacuum annealing and annealing in forming gas, known as post-hydrogenation. Vacuum annealing was performed in a high-vacuum chamber of base pressure of $\sim3\times10^{-8}$ Torr at 360 °C for 3 hours. Post-H was performed in a standard horizontal resistance furnace using high purity N_2/5% H_2 at 400 °C for 3 hours, with a flow rate of 20 mL/min. A comparison of annealing atmospheres (vacuum and air, both commonly used in LIGO mirror coating treatments) is provided in Appendix B.

6.3 Results

6.3.1 Hydrogen content

Hydrogen content and depth profiles obtained from RBS+ERDA experiments are presented in Fig. 6.1, 6.2 and 6.3. By comparing the in-situ hydrogenated samples, and Ar-deposited samples with post-hydrogenation, it is obvious that the in-situ H is more effective than post-H in introducing hydrogen into *a*-Si, and the highest amount of H is observed in the RT-deposited, Ar/10% H_2 in-situ H film (0.40 at.%). Moreover, a higher degree of inhomogeneity is seen in the depth profile of the post-hydrogenated samples. The non-uniform distribution of hydrogen in post-H films may be attributed to the fact that hydrogen diffusion initiates from the surface, leading to a higher concentration of hydrogen at the front surface compared to the end of the film. The presence of two peaks in

the depth profile may be a consequence of hydrogen becoming trapped at the electronic states that form at the surface of the *a*-Si film and at the interface between the film and the substrate, caused by dangling bonds from the disrupted structure.

The amount of hydrogen incorporated in MS *a*-Si:H films is much lower than that in other studies on in-situ H, including RF sputtered *a*-Si:H (0.5−16 at.%) [139], HWCVD and PECVD *a*-Si:H (∼10 at.% or more) [140], and post-H *a*-Si:H, such as RF sputtered *a*-Si:H films (up to ∼8 at.%) [133] and e-beam *a*-Si:H films (maximum 1.45 at.%) [95]. There are two possible explanations: 1) the hydrogen was introduced into the MS films in molecular form rather than as atomic H in CVD techniques and hydrogen plasma treatment, and 2) the structure of MS *a*-Si has been found to be very compact when grown at low gas pressure (1.5 mTorr), as discussed in Sec. 4.3.1, and such a dense film structure might impede H incorporation both for in-situ H and post-H.

We further investigated the impact of vacuum annealing on hydrogen content. The hydrogen incorporated during in-situ H remains in the film after annealing at 360 °C, for up to 6 hours in high vacuum, as shown in Fig. 6.4. Previously, Molina-Ruiz et al. reported that in HWCVD *a*-Si:H, the hydrogen content does not reduce when annealing the samples at 200 °C [93]. Our results indicate that high-temperature treatments, up to 360 °C, can be conducted on MS *a*-Si:H without significant hydrogen loss. It was also found that the hydrogen content in the MS in-situ H films after post-H remains almost unchanged within the margin of error (∼0.02 at.%).

6.3.2 Dangling bond density

As mentioned before in Sec. 4.3.3, MS *a*-Si films contain a much higher dangling bond density ($\sim 10^{19}$ spins·cm^{-3}) than typical device-quality *a*-Si ($\sim 10^{16}$ spins·cm^{-3}) [129], and also e-beam *a*-Si ($\sim 10^{18}$ spins·cm^{-3}) [95]. Hydrogenation is expected to lower ρ_{DB} due to H passivation of DB. However, inconsistent behavior of ρ_{DB} with H content was observed in in-situ H (using Ar/5% H_2) and post-H MS *a*-Si:H, as illustrated in Fig. 6.5. The unhydrogenated *a*-Si samples grown at RT and 360 °C, as well as the in-situ H sample grown at RT, exhibit similar ρ_{DB}. In contrast, the 360 °C in-situ H sample shows a significantly lower ρ_{DB} (1.8×10^{18} spins·cm^{-3}) despite having a lower H content than the RT-grown in situ-H sample (0.09 vs 0.26 at.% H, see Fig. 6.1).

After vacuum annealing, the hydrogenated sample (RT, Ar+H_2 in Fig. 6.5) exhibits a significant reduction of over one order of magnitude in ρ_{DB}, while the

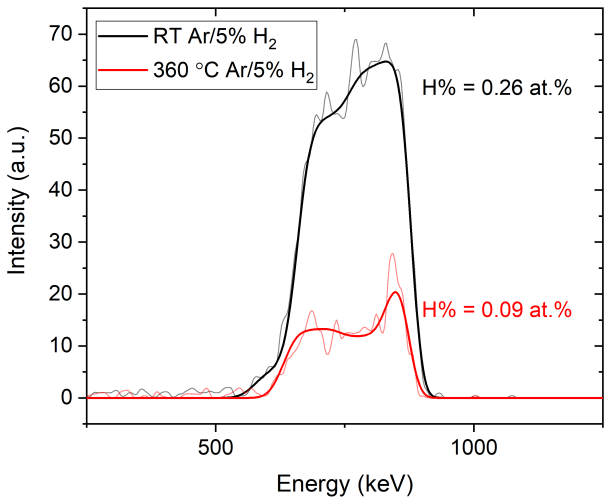

Figure 6.1: The simulated ERDA spectra of MS in-situ H a-Si:H films grown at RT and 360 °C with Ar/5% H_2. The thin lines show the smoothed experimental data. The lower the energy of scattered particles, the deeper in the sample the signal was obtained.

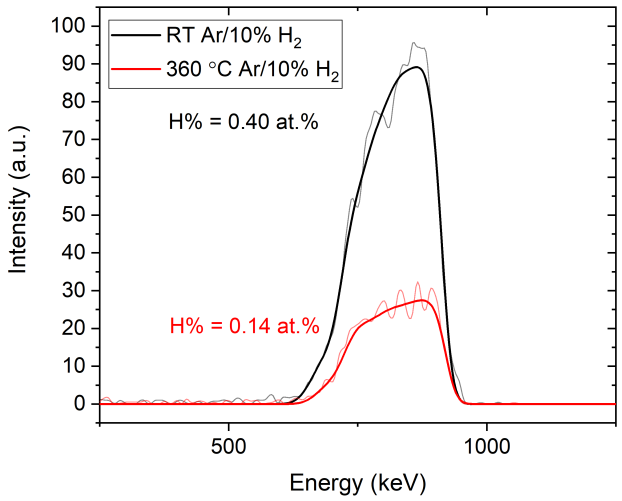

Figure 6.2: The simulated ERDA spectra of MS in-situ H a-Si:H films grown at RT and 360 °C with Ar/10% H_2.

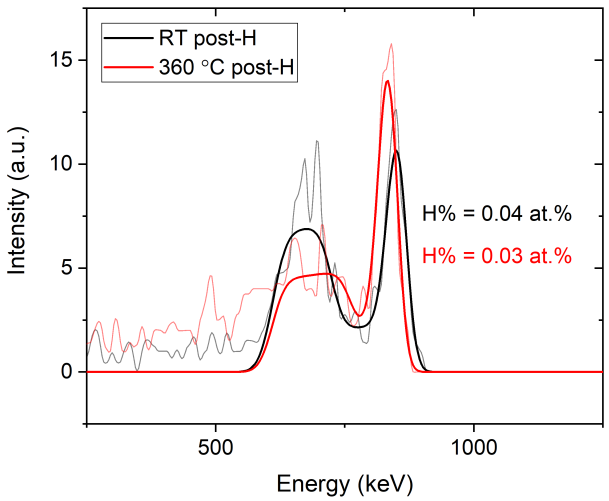

Figure 6.3: The simulated RBS spectra of MS post-H a-Si:H films grown at RT and 360 °C that initially contained no hydrogen in as-deposited state. Hydrogen was introduced only during post-hydrogenation.

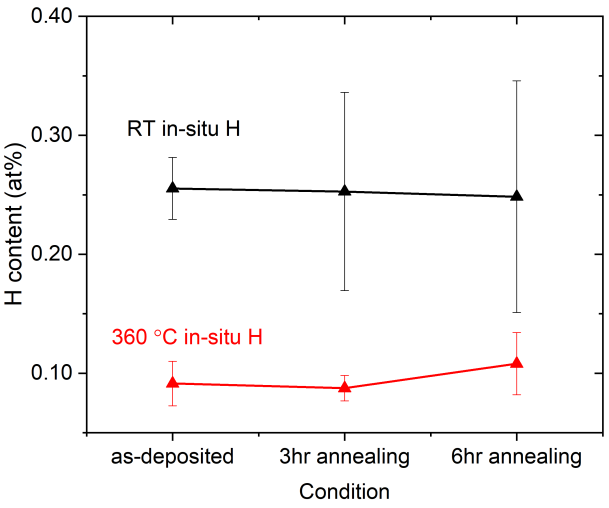

Figure 6.4: Hydrogen content of MS in-situ H a-Si:H samples, as-deposited and after vacuum annealing for 3 and 6 hours.

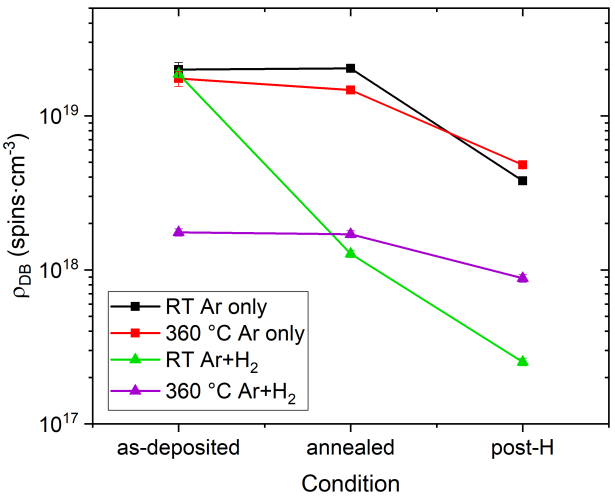

Figure 6.5: Dangling bond density of MS a-Si deposited using pure Ar (Ar only), and a-Si:H deposited using Ar/5% H_2 (Ar+H_2) in their as-deposited, annealed and post-H forms.

ρ_{DB} of the other three samples barely changed. Post-H effectively reduced the ρ_{DB} of the unhydrogenated samples to approximately one fourth of their initial ρ_{DB} value. The extent of reduction in ρ_{DB} of in-situ H samples with post-H strongly depends on the growth temperature; after post-H, ρ_{DB} of the RT-grown in-situ H sample is lower than the 360 °C-grown in-situ H sample, despite its initial much higher value, and reaches an even lower level (2.5×10^{17} spins·cm^{-3}) than the post-H RT e-beam sample (8×10^{17} spins·cm^{-3}) [95].

Overall, three effective means to remove dangling bonds were identified: 1) RT in-situ H followed by vacuum annealing, 2) in-situ H prepared at high T_s, and 3) post-H, with the lowest ρ_{DB} found for RT in-situ H annealed and post-H processed sample. This indicates that effective termination of dangling bonds by hydrogen is contingent upon the provision of thermal energy.

6.3.3 Bond angle deviation and local bond strain

Figure 6.6 shows bond angle deviation of *a*-Si:H films grown under different atmospheres and substrate temperatures. For films grown with pure Ar (0% H_2 in Fig. 6.6), $\Delta\theta$ is reduced with increased T_s, as previously discussed in Chapter 4. Additionally, $\Delta\theta$ is further reduced by both vacuum annealing and post-H treatment for RT-deposited and 360 °C-deposited samples, which is consistent with the findings in e-beam *a*-Si:H [95]. In the in-situ H films, $\Delta\theta$ is initially low in

as-deposited films, and shows no significant improvement with a higher H_2 ratio in the working gas, or with annealing or post-H treatment. This observation holds true for both sets of samples deposited with 5% and 10% H_2 mixed with Ar, both at RT and 360 °C. Overall, after vacuum annealing and post-H, the in-situ H samples deposited at RT shows a slightly lower $\Delta\theta$ compared to the sample that was not hydrogenated during growth; for 360 °C-deposited films, all three samples reach similar levels of $\Delta\theta$, regardless of their initial states.

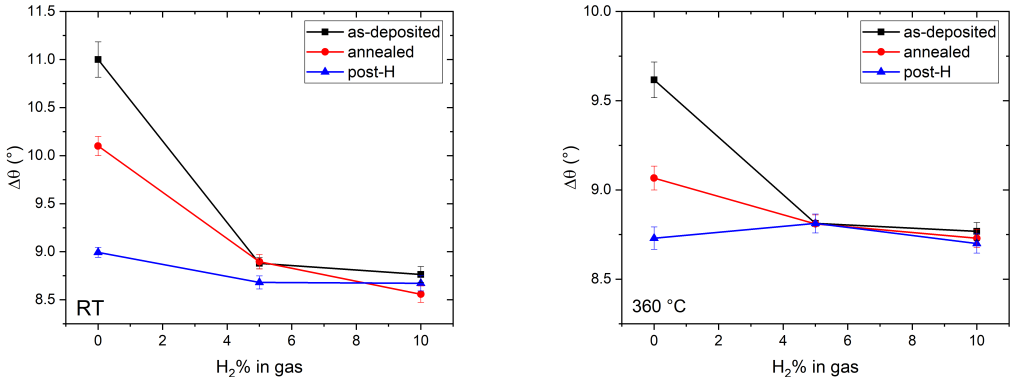

Figure 6.6: Bond angle deviation of MS a-Si:H grown at room temperature (left) and 360 °C (right) vs percentage of H_2 used during deposition.

Local strain analysis of the as-deposited samples revealed that the presence of in-situ hydrogen induces a higher strain in the Si–Si bonds compared to the unhydrogenated *a*-Si. This strain was not dependent on the hydrogen content in the *a*-Si:H films (Fig. 6.7). After annealing and post-H, the initially unhydrogenated samples (0% H_2) show an increase in the local strain compared to their as-deposited state. On the other hand, the in-situ hydrogenated samples (5% and 10% H_2) experience a decrease in total strain, with a greater reduction observed in the *a*-Si:H film grown using Ar/5% H_2. In general, the 360 °C-deposited samples exhibit a lower tr(ε) than the RT-deposited samples in equivalent states, consistent with the results from Ar-deposited *a*-Si presented in Sec. 4.3.2.

6.3.4 Mechanical loss

The mechanical loss at room temperature of MS *a*-Si and in-situ H *a*-Si:H films grown using Ar/5% H_2 is compared in different states: as-deposited, vacuum annealed and post-hydrogenated, as shown in Fig. 6.8. The in-situ H films consistently exhibit lower Q_{RT}^{-1} values than the films deposited with pure Ar in all three states, at the same T_s. Annealing shows a larger improvement in

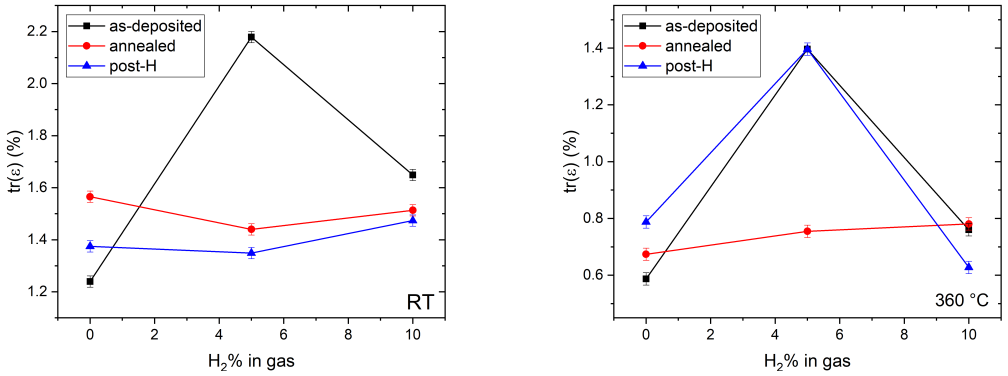

Figure 6.7: Local bond strain of MS a-Si:H grown at room temperature (left) and 360 °C (right) vs the percentage of H_2 used during deposition.

the RT-deposited samples compared to the samples deposited at 360 °C. Post-hydrogenation is effective in reducing Q_{RT}^{-1} of unhydrogenated *a*-Si films, resulting in a 41% reduction for the RT-deposited films and a 25% reduction for the 360 °C-deposited films. Among all the samples, the lowest Q_{RT}^{-1} value of 2.2×10^{-5} is achieved in the in-situ H 360 °C sample after annealing and post-H, which is approximately 4 times lower than the record loss reported for as-deposited *a*-Si grown using Xe at 360 °C and 1.5 mTorr (Fig. 5.5), and approximately 9 times lower than that for e-beam *a*-Si:H deposited at 425 °C, followed by annealing and post-H [95].

Due to limited availability of DPO substrates, investigation of low-T mechanical loss in MS *a*-Si:H films was not conducted. However, a similar study on e-beam *a*-Si:H films has been performed [95]. Molina-Ruiz et al. showed that after annealing and post-H, the plateau loss Q_0^{-1} at 1 K is reduced by a factor of 2 in RT-deposited samples, and there is no decrease in the very low Q_0^{-1} at 1 K observed in the 425 °C-deposited samples. The loss at 100 K, which is close to the proposed operating temperature for LIGO Voyager (123 K) [41], becomes lower after post-H for both the RT- and 425 °C-grown e-beam *a*-Si. Based on these findings, it is reasonable to infer that the introduction of hydrogen to *a*-Si might improve and very likely at least would not worsen the low-T loss, which is promising news for cryogenic GW detectors.

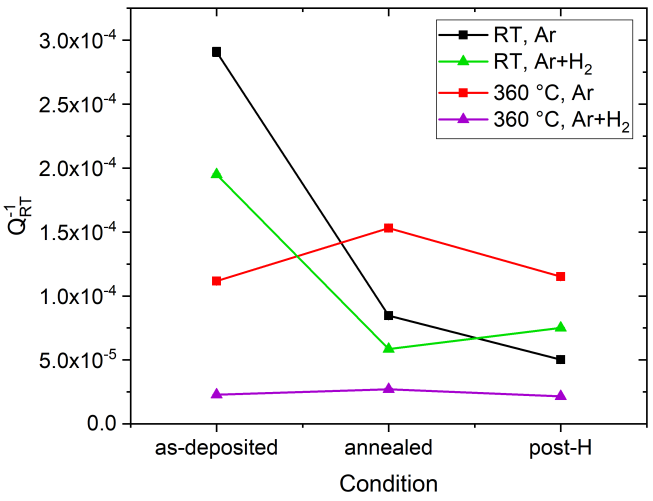

Figure 6.8: Room-temperature mechanical loss of MS a-Si:H grown at RT and 360 °C with Ar/5% H_2 (Ar+H_2) and without H_2 (Ar only), measured in as-deposited, annealed and post-H states.

Deposition conditions	Q_{RT}^{-1} ($\times 10^{-5}$)		
	as-deposited	annealed	post-H
RT, Ar only	29.1±0.4	8.5±0.3	5.0±0.2
360 °C, Ar only	11.2±0.1	15.3±0.1	11.5±0.1
RT, Ar+H_2	19.5±0.1	5.9±0.1	7.5±0.1
360 °C, Ar+H_2	2.3±0.1	2.7±0.1	2.2±0.1

Table 6.1: Room-temperature mechanical loss of MS a-Si:H deposited with pure Ar and Ar/5% H_2, measured in various conditions.

6.3.5 Optical absorption

Optical absorption of MS *a*-Si:H at 1064, 1550 and 2000 nm, normalized to a film thickness of 300 nm, is shown in Fig. 6.9, 6.10, 6.11 and Table 6.2. Comparing the as-deposited samples, in-situ hydrogenation effectively reduces optical absorption in *a*-Si for both T_s. Moreover, increasing the H_2 ratio in the working gas leads to a larger decrease in absorption at all three tested infrared wavelengths. Vacuum annealing is more efficient in suppressing absorption in the RT-deposited samples than in those samples grown at elevated T_s, consistent with findings in e-beam *a*-Si [95]. Post-H treatment is equally effective in reducing absorption in initially unhydrogenated and in-situ hydrogenated samples.

Among all the samples, the RT, in-situ H Ar/10% H_2 *a*-Si:H sample demonstrates the lowest absorption at all three measured infrared wavelengths, after a 3-hour vacuum annealing and subsequent 3-hour post-H treatment (Table 6.2). Its performance at 1550 nm (13 ppm) surpasses that of the e-beam RT-deposited *a*-Si:H sample after vacuum annealing and post-H treatment, which has an absorption of 360 ppm, but shows slightly higher absorption at 2000 nm (32 ppm) compared to that e-beam sample, which has an absorption of less than 10 ppm. The e-beam *a*-Si:H study observed that post-hydrogenation of as-deposited samples achieved the same optical absorption as those annealed and then post-hydrogenated, suggesting the possibility of skipping the vacuum annealing step and simplifying the post-growth treatment process [95].

We observed an interesting phenomenon in the two in-situ H samples with Ar/10% H_2: their absorption at 1550 nm can be lower than that at 2000 nm. This observation contradicts the expected behavior in the Urbach tail model, where optical absorption should exponentially decrease with lower photon energy (Eq. 1.3.2). Notably, this phenomenon is only observed when the absorption level in the two MS *a*-Si:H samples becomes quite low, reaching around 100 ppm. We have ruled out substrate absorption or limitations of the PCI technique used to measure the absorption, confirmed by our collaborators at Stanford, and therefore this difference is likely attributed to our films themselves. Potential mechanisms will be discussed in more detail in Sec. 6.4.

Additional vacuum annealing of RT, Ar- and Ar/5% H_2-deposited films that have undergone post-hydrogenation resulted in a decrease in absorption only at 1064 nm, while the absorption at 1550 nm and 2000 nm remained unchanged. The RT, in-situ H Ar/5% H_2 *a*-Si:H sample, after a total of 27 hours of vacuum annealing and 3 hours of post-H, achieved a lower absorption at 1064 nm with a value of 1562 ppm, compared to 2604 ppm after 3 hours of annealing and 3 hours of post-H for a 300 nm-thick layer.

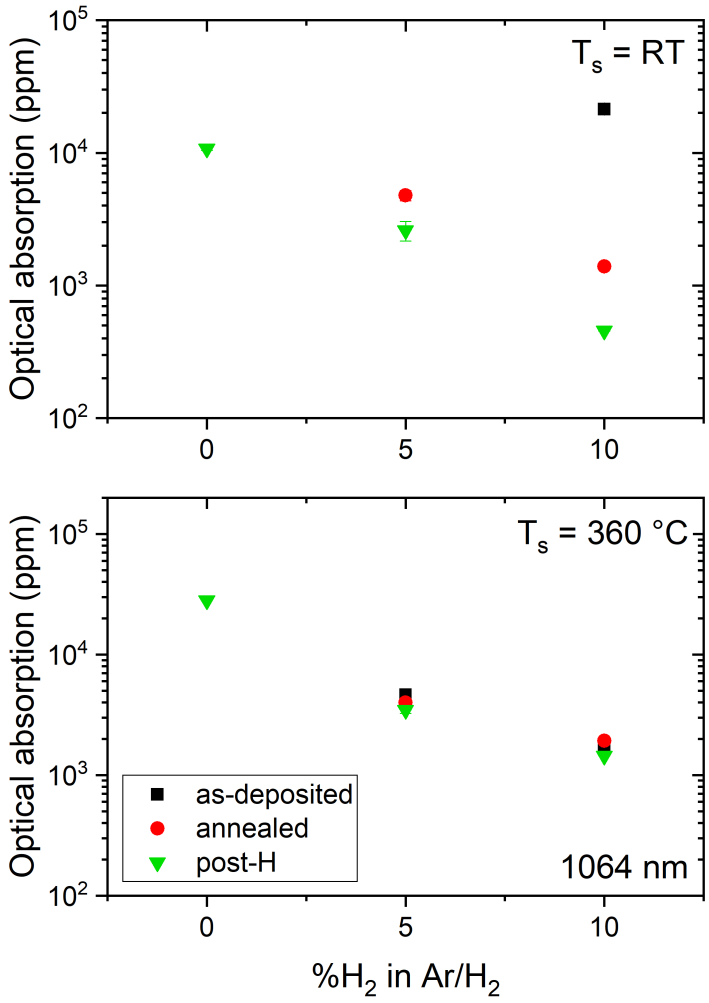

Figure 6.9: Optical absorption of MS a-Si:H films at laser wavelength of 1064 nm in as-deposited, annealed and post-H conditions, normalized to a film thickness of 300 nm. Samples were deposited at two substrate temperatures, RT and 360 °C, and using three types of working gas, pure Ar, Ar/5% H_2 and Ar/10% H_2.

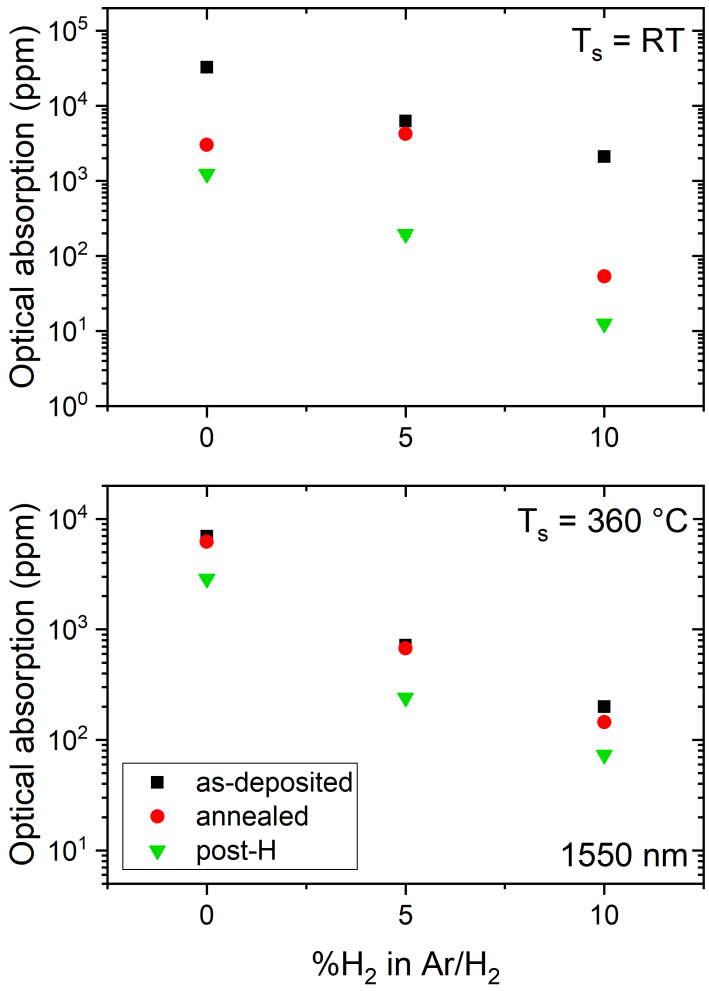

Figure 6.10: Optical absorption of MS a-Si:H films at laser wavelength of 1550 nm in as-deposited, annealed and post-H conditions, normalized to a film thickness of 300 nm. Samples were deposited at two substrate temperatures, RT and 360 °C, and using three types of working gas, pure Ar, Ar/5% H_2 and Ar/10% H_2.

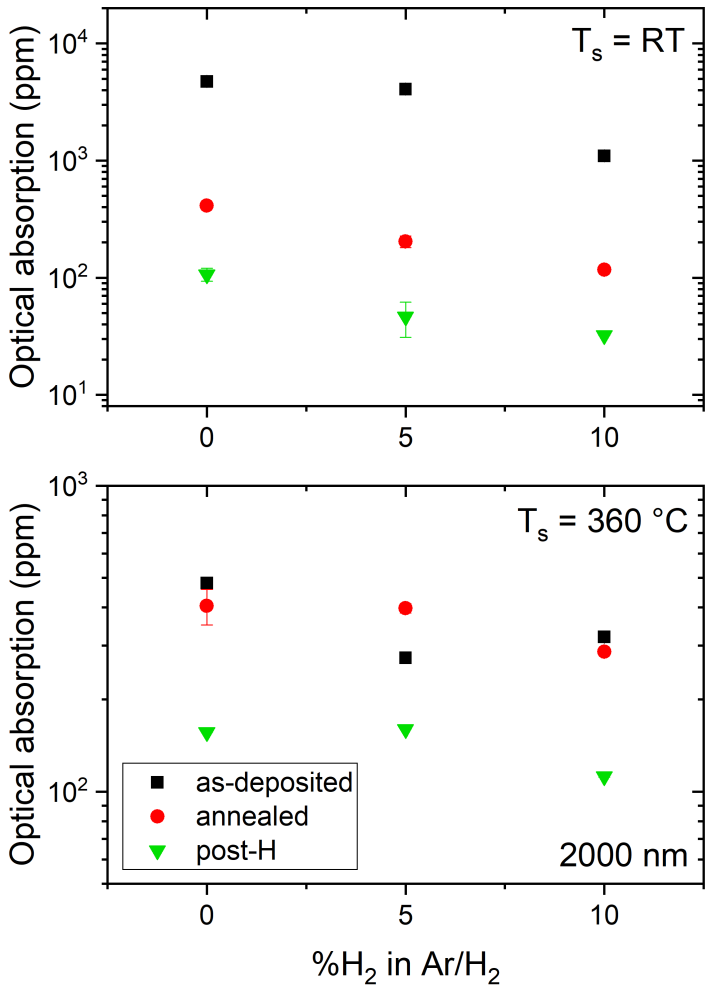

Figure 6.11: Optical absorption of MS a-Si:H films at laser wavelength of 2000 nm in as-deposited, annealed and post-H conditions, normalized to a film thickness of 300 nm. Samples were deposited at two substrate temperatures, RT and 360 °C, and using three types of working gas, pure Ar, Ar/5% H_2 and Ar/10% H_2.

Deposition conditions	as-deposited			vacuum annealed			post-hydrogenated		
	1064 nm	1550 nm	2000 nm	1064 nm	1550 nm	2000 nm	1064 nm	1550 nm	2000 nm
RT Ar		32785	4736		3017	414	10755	1248	107
360 °C Ar		6947	480		6236	404	28134	2864	156
RT Ar/5% H_2		6255	4077	4774	4245	204	2604	197	46
360 °C Ar/5% H_2	4625	719	274	3998	673	397	3456	241	160
RT Ar/10% H_2	21387	2118	1097	1395	54	117	456	13	32
360 °C Ar/10% H_2	1665	200	320	1928	144	287	1446	73	112

Table 6.2: Optical absorption of MS a-Si:H films at laser wavelength of 1064, 1550 and 2000 nm in as-deposited, annealed and post-H states, for a 300 nm-thick film. Deposition conditions indicate their growth temperature, RT or 360 °C, and the working gas used, pure Ar, Ar/5% H_2 or Ar/10% H_2.

6.4 Discussion

We studied the effects of hydrogenation, namely in-situ hydrogenation and post-hydrogenation, on the room-temperature mechanical loss and the optical absorption of *a*-Si, as well as on the structure, specifically dangling bond density and bond angle deviation. In terms of the RT mechanical loss, the as-deposited samples showed that the in-situ hydrogenated films had lower loss compared to the unhydrogenated films for both T_s studied. The difference was particularly notable in the 360 °C-grown samples. A fivefold improvement in Q_{RT}^{-1} for the 360 °C-deposited film grown with Ar/5% H_2 compared to the film deposited with Ar alone (Table 6.1). This significant improvement cannot be solely attributed to the small amount of hydrogen (0.09 at.%) incorporated during growth without any other associated effects or processes leading to the observed enhancement. Moreover, annealing only reduces the Q_{RT}^{-1} of the RT-grown samples, but not the 360 °C-grown ones. Post-H treatment proved more effective for the unhydrogenated samples at both T_s. Overall, the annealed and post-hydrogenated 360 °C, in-situ H Ar/5% H_2 sample showed the lowest mechanical loss (2.2×10^{-5}), though being comparable to its as-deposited state (2.3×10^{-5}).

The photon energies at 1.16, 0.80 and 0.62 eV correspond to wavelengths of 1064, 1550 and 2000 nm, respectively, which are the three wavelengths of interest. These values are below the typical band gap of *a*-Si:H, which is reported to be 1.5−2.0 eV [141, 142], commonly extracted from the Tauc plot of optical absorption versus photon energy, as detailed in Sec. 1.3.1. The band gap of *a*-Si is larger than the indirect band gap of *c*-Si (1.1 eV). It was found that in-situ H leads to lower optical absorption compared to unhydrogenated samples in all states (as-deposited, annealed and post-H) at all three laser wavelengths measured, as shown in Table 6.2. Increasing the H_2 ratio from 5% to 10% in the working gas leads to reduced absorption at all three wavelengths for all states. Remarkably, the changes in absorption were particularly pronounced at 1064 nm and 1550 nm (with over an order of magnitude difference) compared to 2000 nm (with 3-4 fold difference in RT-deposited samples and less than a twofold difference in 360 °C-deposited samples). This discrepancy may be due to the photon energy at 1064 and 1550 nm being closer to the band gap size, making it more susceptible to presence or removal of states contributing towards the Urbach tail (discussed in Sec. 1.3.1).

The RT in-situ H Ar/10% H_2 sample demonstrates the lowest absorption at the three investigated infrared wavelengths after annealing and post-H treatment. It achieves ppm-level absorption at 1550 nm (13 ppm) and 2000 nm (32 ppm) for a 300 nm thick film. Notably, the absorption at 1550 nm is lower than previously reported values for e-beam *a*-Si:H (360 ppm) [95], IBS *a*-Si (2227 ppm) [96] and

RLVIP a-Si (1066 ppm) [91], all normalized to a 300 nm film thickness. Although the absorption at 1064 nm (448 ppm) still exceeds the desired ppm-level absorption, it represents a significant improvement compared to IBS a-Si (11305 ppm) [96], which opens up possibilities for applying the design of multimaterial coatings proposed in Ref. 97 to the current GW detectors.

Dangling bonds are known to create trap states within the band gap of Si, which can act as recombination centers for charge carriers and affect the electrical properties of the material. Given the high DB density in MS a-Si:H (most ranging from $10^{18}-10^{19}$ spins·cm^{-3}), one would expect significant sub-band gap absorption ($0.01-0.1\%$) resulting from localized, mid-gap states associated with these bonds. However, the MS a-Si:H samples exhibit low levels of infrared absorption, on the order of tens of parts per million.

The data also show that the changes in ρ_{DB} do not account for, or even correlate with the observed improvements in optical absorption resulting from in-situ hydrogenation, high growth temperatures, and vacuum annealing. For instance, two samples deposited at room temperature, one unhydrogenated and the other in-situ hydrogenated with 5% H_2, exhibit the same ρ_{DB} but demonstrate different levels of absorption at 1550 nm and 2000 nm. Specifically, the in-situ H sample shows an absorption that is approximately 5 times lower at 1550 nm and approximately 10 times lower at 2000 nm compared to the unhydrogenated sample. Another example is the comparison between two unhydrogenated films grown at RT and 360 °C after vacuum annealing, which show nearly identical DB density (Fig. 6.5). Nevertheless, even in the absence of hydrogen to bond with unpaired electrons, their optical absorption decreases at both measured wavelengths. Moreover, despite their comparable ρ_{DB} values after post-H, these films exhibit notably different absorption levels at all three measured infrared wavelengths, especially at 1064 nm. These observations align with the findings of Seager et al. [143], who reported a reduction in sub-band gap ($0.5-1.0$ eV) optical absorption without any measurable changes in ρ_{DB}. These results suggest that dangling bonds are not the primary source of infrared wavelength photon absorption in a-Si and instead that the a-Si structure more broadly is crucial.

In Sec. 4.3, it was shown that there is lack of correlation between dangling bond density and RT mechanical loss of MS a-Si. We also observed no relationship between these two properties in MS a-Si:H; the three samples that exhibited the same ρ_{DB} in their as-deposited state, RT and 360 °C Ar-deposited a-Si, and RT in-situ H a-Si:H, showed very different Q_{RT}^{-1}, with a difference up to 2.6 times (Fig. 6.8 and Table 6.1). Additionally, our findings suggest that the passivation of dangling bonds in a-Si:H requires both the presence of hydrogen and the supply of heat. However, a lower Q_{RT}^{-1} can be achieved by either of these factors alone,

as seen in Fig. 6.8. This confirms that the loss mechanism at RT is not related to dangling bonds.

Turning now to other aspects of the structure of *a*-Si:H, specifically the bond angle deviation, $\Delta\theta$, we showed that the introduction of hydrogen (in-situ H), the application of heat (high T_s, vacuum annealing), or a combination of both (post-H) leads to a decrease in bond angle deviation, as depicted in Fig. 6.6. Notably, vacuum annealing and post-H cause a significant reduction in $\Delta\theta$ in the initially unhydrogenated samples, bringing their $\Delta\theta$ down to a similar level as that of the in-situ H samples. Molecular dynamics simulations by Sriraman et al. proposed mechanisms through which hydrogen can insert into strained Si–Si bonds, facilitating bond breakage and formation and promoting a transition to a more energetically stable configuration [83, 85]. The similar $\Delta\theta$ observed in Ar/5% H_2 and Ar/10% H_2 in-situ H films, despite their quite different hydrogen content, implies that the effectiveness of hydrogenation in promoting structural relaxation is not associated with the amount of hydrogen remaining in the film. This suggests that hydrogen acts as a catalyst, lowering the energy barrier for atomic rearrangement. It diffuses to other sites and initiates the process again after leaving the affected bond. Consequently, the resulting structure exhibits a higher degree of order compared to unhydrogenated *a*-Si. The absence of further improvement with subsequent processing steps (annealing and post-H) suggests that the structural ordering of MS *a*-Si:H films may have reached a limit.

In Chapter 4 and 5 we discussed how Q_{RT}^{-1} is related to the network rigidity, which can be viewed from two aspects, the resistance of the bonds to movement, described by the bond stiffness, and the flexibility of individual atom movement, subject to its adjacent environment. The RT dissipation mechanism is found to be reduced by a more ordered film structure and a rigid Si–Si bonding network, reflected by a lower bond angle deviation and higher shear modulus. As seen in Fig. 6.6, $\Delta\theta$ of as-deposited in-situ H samples is much lower than those deposited without H_2, which accounts for their lower Q_{RT}^{-1}. However, subsequent post-H introduces a much smaller improvement in $\Delta\theta$ of in-situ H *a*-Si:H than those Ar-deposited films. This observation correlates well with the changes seen in Q_{RT}^{-1}: the Ar-deposited *a*-Si experienced a decrease in Q_{RT}^{-1} after post-H, whereas Q_{RT}^{-1} of the in-situ H samples is not improved with post-H. These observations are true for both growth temperatures studied in this work.

This hydrogen-induced structural ordering is found to play a crucial role in suppressing sub-band gap absorption as well. Growing the samples with hydrogen (comparing in-situ H samples to unhydrogenated samples) and performing vacuum annealing (specifically in RT-deposited samples) result in lower absorption at infrared wavelengths. These changes in absorption are correlated with varia-

tions in $\Delta\theta$. Interestingly, post-H treatment proves equally effective in reducing optical absorption at all three studied wavelengths in films deposited at the same T_s, regardless of their initial hydrogen content. This suggests that exposure to a hydrogen-rich environment at high temperature assists the gradual removal of band-tail states near the band edge over time, even without a significant improvement in structural order (measured by $\Delta\theta$). Therefore, it is clear that defects that are distinct from dangling bonds, which show no correlation with optical absorption at infrared wavelengths, and not directly reflected in $\Delta\theta$, create electronic states that contribute to the Urbach tail and the associated photon absorption in *a*-Si:H. We propose that these defects are likely charged point defects, similar to those observed in *c*-Si, where charged divacancies introduce states near the valence and conduction band edges, or in the middle of the band gap, depending on their charge state and the foreign atom trapped in them [144–146].

The higher absorption at 1550 nm compared to 2000 nm in MS RT- and 360 °C-deposited Ar/10% in-situ H *a*-Si:H, when the film absorption is at the level of 100 ppm (Table 6.2), is not explained by the band tail model. In *c*-Si, extensive studies have shown that dopants and point defects create electronic states, and carriers are excited from these localized states into the conduction band by absorbing light [147, 148]. The possibility of impurities in our MS *a*-Si:H films being responsible for the excess absorption at the longer wavelength of 2000 nm, compared to 1550 nm, exists. Obtaining a full optical spectrum in the infrared and near-visible wavelength range would be helpful to precisely identify these defects and their specific contributions to the optical absorption of *a*-Si:H.

6.5 Summary

In summary, the investigation of hydrogenation in magnetron sputtered *a*-Si films, both during growth and post-growth, highlighted the significant role of hydrogen in enhancing the performance of *a*-Si:H, specifically in terms of its room-temperature mechanical loss and optical absorption at infrared wavelengths. The RT-deposited, in-situ hydrogenated *a*-Si:H using Ar mixed with 10% H_2 exhibits a very low, ppm-level absorption after annealing and post-hydrogenation at two critical infrared wavelengths (1550 nm and 2000 nm) of interest in GW detector designs. This low absorption positions it as a highly promising candidate for future GW detectors. Its improved absorption at 1064 nm compared to previous studies also suggests the potential for utilizing multimaterial coating designs in the upgrade of current GW detectors. Additionally, the 360 °C, in-situ H sample reports the lowest RT mechanical loss found in *a*-Si and *a*-Si:H, which is 2.2×10^{-5}.

Changes in dangling bond density and structural ordering of MS *a*-Si:H suggest the dual role of hydrogen in *a*-Si: it not only bonds with dangling bonds and saturates them, which is effective only at elevated temperatures, but also facilitates the rearrangement of Si–Si bonds, resulting in a lower deviation in bond angle. The hydrogen-induced structural relaxation is observed to be independent of hydrogen content, implying that the improvement in structural order of *a*-Si:H is not achieved through hydrogen permanently bonding to Si atoms. Instead, hydrogen likely functions as a catalyst in promoting the relaxation and rearrangement of strained Si–Si bonds, and leaves and diffuses to other sites to further assist such processes. Nonetheless, prolonged annealing in vacuum or in a hydrogen-rich environment reaches a point where the structural order improvement plateaus, while the infrared absorption continues to improve. These results indicate that the band-tail states, which may be related to specific structural features beyond structural ordering, possibly charged point defects, also contribute to infrared absorption in *a*-Si:H. Overall, these findings shed light on the mechanisms underlying photon absorption and energy dissipation in *a*-Si:H, and have significant implications for optimizing *a*-Si:H-based devices in various applications beyond GW detectors.

CHAPTER 7

EXPLORING AMORPHOUS SILICON CARBIDE AS A NEW OPTION

7.1 Introduction

The investigation of amorphous silicon carbide (a-Si_xC_{1-x}, where x represents the Si composition) coating is primarily driven by its larger band gap compared to pure a-Si, which would effectively reduce absorption at infrared wavelengths [149]. In addition, if the dominant bonding type in a-Si_xC_{1-x} is sp^3 bonding with a tetrahedral coordination, similar to that in diamond structure, we expected that a-Si_xC_{1-x} would retain the excellent loss properties observed in a-Si. Moreover, the advantage of being able to grow a-Si_xC_{1-x} at significantly higher substrate temperatures (around 900 °C) without forming nanocrystals presents an opportunity to exploit the benefits of high temperatures in improving the optical and mechanical properties of a-Si_xC_{1-x} [150]. This motivates the deposition of a-Si_xC_{1-x} at temperatures surpassing what could be achieved in a-Si before crystallization.

Amato previously investigated CVD polycrystalline 3C-SiC as a potential option for GW detector mirror coatings but found its optical absorption to be too high [151]. Favaro et al. explored near stoichiometric ion-beam sputtered and magnetron sputtered a-Si_xC_{1-x} films with varying silicon content (ranging from 42.5 to 53.5 at.% Si) and observed high absorption at 1064 nm, with only slight improvement in MS samples after annealing at 500 °C [152]. Interestingly, the RT mechanical loss measured by GeNS showed contrasting trends between IBS and MS a-Si_xC_{1-x}; the IBS samples exhibited decreasing loss with resonant frequency, while the MS sample showed increasing loss. However, the reasons for these differing behaviors were not explained. The overall loss angle of the studied samples is close to 10^{-3} at 10 kHz, which is much higher than that of pure a-Si (Table 4.1 and 5.2) and a-Si:H (Table 6.1). Despite these initial unpromising results, there remain several unexplored parameters, such as deposition conditions, Si-rich compositions, and post-growth processing. Therefore, our study aims to provide a more comprehensive investigation of a-Si_xC_{1-x} as a high-index layer material for GW detector mirror coatings.

In this chapter, results from MS a-Si_xC_{1-x} films, deposited using Ar and Ar/H_2 under various conditions, are presented and discussed. The objective is to develop a-Si_xC_{1-x} films with reduced mechanical loss and optical absorption, particularly at 1064 nm, making them suitable for direct application in upgrading the current aLIGO detectors.

7.2 Experimental details

Stoichiometric SiC sputtering targets (purity: 99.5%) and undoped Si targets (purity: 99.999%) were utilized to fabricate a-Si_xC_{1-x} films with various compositions, aiming for $x \geq 0.5$. The sputtering gas used was Ar or Ar mixed with H_2, with a total gas flow set at 10 sccm. The gas pressure was varied from 1.5 to 4.0 mTorr to investigate its impact and compare it to that on a-Si, as discussed in Chapter 4. By introducing carbon, SiC is able to maintain its amorphous state at much higher substrate temperatures compared to Si (approximately 450 °C for Si) [150]. Therefore, the highest attempted T_s was 660 °C, limited by the maximum heater temperature in our magnetron sputtering system. In-situ hydrogenation was conducted by sputtering using an Ar gas mixture H_2 concentrations of 0.5%, 1% and 5%. The growth rate was maintained at around 0.25−0.40 Å/s when sputtering from only the SiC target, and roughly 0.50 Å/s when co-sputtering from SiC and Si targets.

Interestingly, the MS a-Si_xC_{1-x} films deposited only from the stoichiometric SiC target appear semi-transparent to visible light, as shown in Fig. 7.1, contrary to the pure MS a-Si films which look metallic gray. This suggests that these MS a-Si_xC_{1-x} samples have a larger band gap than that of MS a-Si, resulting in lower absorption at visible wavelengths. The transparency of Ar 1.5 and 4.0 mTorr samples deposited at the same T_s shows no significant difference.

7.3 Results

7.3.1 Bonding environment in a-Si_xC_{1-x}

We prepared a-Si_xC_{1-x} samples sputtered from a stoichiometric SiC target, and they have a composition of 47−47.5 at.% in Si, determined by XPS, referred to as a-$Si_{47}C_{53}$. Their bonding information is shown in Fig. 7.2. At higher Ar pressure (4.0 mTorr), there is a slight preference for the formation of sp^3 bonding over sp^2 bonding in C–C interactions. This means that a higher proportion of carbon

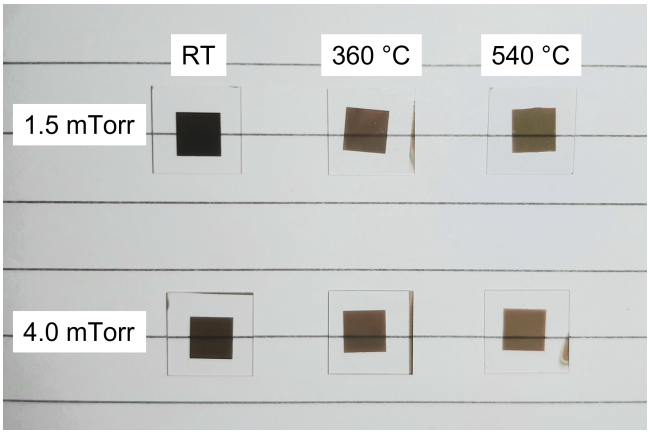

Figure 7.1: Photo of MS a-$Si_{47}C_{53}$ films grown on fused silica substrates at various deposition temperatures and Ar pressure.

atoms is bonded with three other carbon atoms, forming a tetrahedral network. On the other hand, increasing T_s from RT to 360 °C promotes the bonding of Si with C, favoring Si–C bonds (sp^3) in the material, further enhancing the tetrahedral coordination. The native oxide layer on the surface was removed via Ar^+ ion sputtering prior to conducting XPS measurements. The plots presented here do not include the percentage of bonds to oxygen, as the remaining amount of oxygen in the film is small (below 3 at.%).

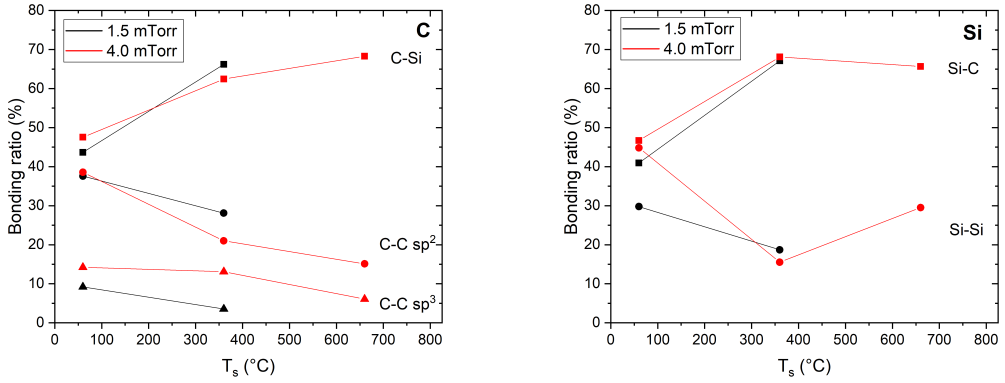

Figure 7.2: Changes in bonding ratios of C (left), and Si (right) with substrate temperature, RT, 360 °C and 660 °C for MS a-$Si_{47}C_{53}$. The black line corresponds to a-$Si_{47}C_{53}$ grown at Ar 1.5 mTorr, while the red line represents those grown at Ar 4.0 mTorr.

At an even higher T_s (660 °C), it was observed that crystallization did not occur, as confirmed by no *c*-Si resonant peak showing in Raman spectrum of this sample. Increased growth temperature facilitates a stronger and more extensive formation of chemical bonds between Si and C atoms, resulting in an increased proportion of Si–C bonding, as demonstrated in Fig. 7.2. Nonetheless, as T_s increases further from 360 to 660 °C, the magnitude of these changes in bonding composition becomes less noticeable.

We also deposited Si-rich *a*-Si_xC_{1-x} by co-sputtering a stoichiometric SiC target and a Si target at an Ar pressure of 1.5, 2.0 and 4.0 mTorr and RT. The change in bonding environment is shown in Fig. 7.3 for various ratios of the two rates, yielding various compositions from $x = 0.47$ to 0.92. As Si composition increases, the percentage of Si–Si bonds increases. In addition, the percentage of C–Si bonds shows an increase with higher Si content. However, it should be noticed that a higher Si composition does not necessarily result in a larger fraction of sp^3 bonding in C–C bonds.

The sample with a Si-rich composition of 89.7 at.% Si and 10.3 at.% C, prepared at room temperature with an Ar pressure of 1.5 mTorr, was selected for optical measurements to compare with *a*-$Si_{47}C_{53}$, and will be referred to as *a*-$Si_{90}C_{10}$ in the following discussion. The bonding composition of this sample is very similar to that of the one deposited at 2.0 mTorr with a very close composition (91.8 at.% Si), which is shown in Fig. 7.3. In *a*-$Si_{90}C_{10}$, Si–Si bonds are dominant, accounting for 87.5% of the Si-related bonds, while C–Si bonds dominate the C-related bonds. The presence of C–C bonds in both sp^2 and sp^3 hybridizations is relatively small, comprising only 6.8% and 4.7% of the total, respectively.

Figure 7.4 illustrates the C–C sp^2 to sp^3 bonding ratio for various Si compositions. We previously thought that the increase in Si–C bonding ratio would promote the formation of C–C sp^3 bonds, however there is no dependence of the C–C sp^2/sp^3 ratio on the Si composition.

We performed vacuum annealing at 360 °C on two Ar 4.0 mTorr *a*-$Si_{47}C_{53}$ samples, one grown at RT, and the other at 360 °C, and found that annealing promotes the formation of Si–C bonds at the sacrifice of Si–Si and C–C bonds, similar to the effect of growing at high T_s. The RT-deposited sample showed a slight shift towards sp^3 bonding in the remaining C–C bonds after annealing (2.7 in as-deposited state and 1.5 in annealed state), whereas the annealed 360 °C-deposited sample showed the same sp^2/sp^3 ratio as its as-deposited form (1.6).

In summary, sp^3 bonding (Si–Si, Si–C and C–C sp^3) in *a*-Si_xC_{1-x} is influenced

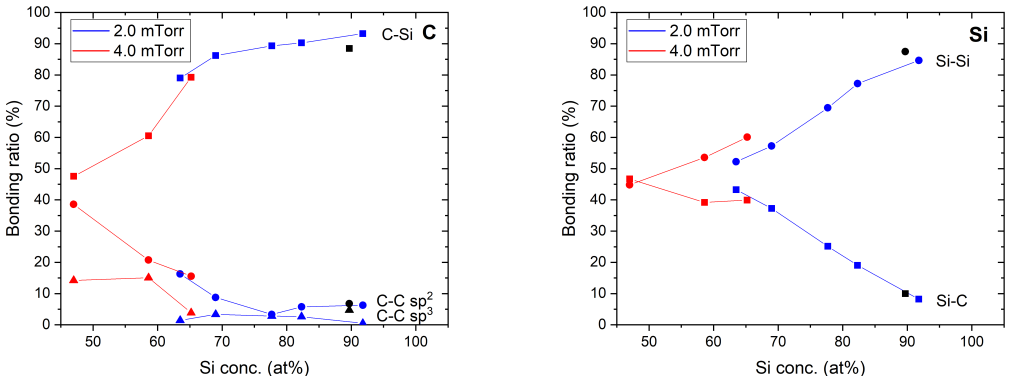

Figure 7.3: Bonding ratios of C (left), and Si (right) of MS a-Si_xC_{1-x} deposited at RT, Ar 2.0 and 4.0 mTorr, with varying Si compositions. The bonding ratios of the RT, Ar 1.5 mTorr a-$Si_{90}C_{10}$ are shown as black symbols in the plots.

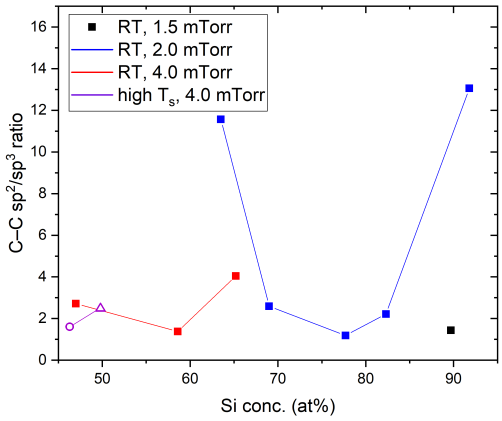

Figure 7.4: C–C sp^2 to sp^3 bonding ratio for various Si compositions. High T_s refers to the samples deposited at 360 °C (open circle) and 660 °C (open triangle).

by four factors: Ar pressure, substrate temperature, Si composition and annealing. Higher Ar pressure during deposition, which reduces the kinetic energy of the adatoms, slightly increases the proportion of tetrahedrally coordinated sp^3 bonds. Increasing substrate temperature promotes bonding between Si and C atoms, favoring the formation of sp^3 bonds. Higher Si composition increases the likelihood of Si atoms participating in bonding, leading to a greater proportion of sp^3 bonding in a-Si_xC_{1-x}. However, the factors mentioned above do not appear to have a significant impact on the preference for the formation of C–C sp^2

bonds in a-Si_xC_{1-x}, apart from annealing, which slightly promotes sp^3 bonding for the RT-deposited sample. As shown in Fig. 7.4, the lowest sp^2/sp^3 ratio is not observed in the sample with the highest Si content, but rather in the one with 77.7 at.% Si deposited at RT and 2.0 mTorr. The sample deposited at RT and 4.0 mTorr with a Si content of 58.6 at.% exhibits a similarly low sp^2/sp^3 ratio.

7.3.2 Mechanical loss

We investigated the mechanical loss at room temperature of both as-deposited and annealed a-$Si_{47}C_{53}$ films under different deposition conditions. These conditions included two different Ar pressures (1.5 and 4.0 mTorr) and three substrate temperatures (RT, 360 °C and 660 °C). Figure 7.5 presents the results of this investigation.

The addition of C to Si increased the RT mechanical loss for all growth conditions. Surprisingly, increasing the Ar pressure during deposition did not have any effect on the loss behavior of the a-$Si_{47}C_{53}$ films, unlike pure MS a-Si, where lower Ar pressure reduced the Q_{RT}^{-1} of the as-deposited a-Si (green dashed line in Fig. 7.5).

When the substrate temperature was raised, two changes in Q_{RT}^{-1} were observed at different T_s. At 360 °C, the RT loss was reduced compared to RT growth, while an unexpected increase in Q_{RT}^{-1} was found when we continued to increase T_s from 360 to 660 °C. This finding suggests the possibility of a structural evolution above certain substrate temperature. The structural evolution, not evident from the bonding information, may contribute to the variations in the Q_{RT}^{-1} of a-$Si_{47}C_{53}$ in different temperature regimes. Further investigation into additional structural parameters beyond the bonding configuration may be required to comprehensively understand the underlying mechanisms driving this phenomenon.

Similar to growing at high T_s (360 °C), annealing the RT-deposited samples at 360 °C has a comparable effect on the Q_{RT}^{-1} of a-$Si_{47}C_{53}$, as demonstrated in Fig. 7.5. This consistency aligns with the findings in e-beam a-Si [95] and MS a-Si (orange dashed line in Fig. 7.5).

Figure 7.6 shows the low-temperature mechanical loss measured by DPOs, from 0.3 to 110 K for a-$Si_{47}C_{53}$ grown under various conditions, compared to similar data for pure MS a-Si. It shows that Q_0^{-1} in a-$Si_{47}C_{53}$ is significantly higher compared to a-Si grown under equivalent conditions. Q_0^{-1} of a-$Si_{47}C_{53}$ is just below the lower end of the glassy range, where the plateau loss is in the range of 10^{-4}. Changing Ar pressure did not have a significant impact on Q_0^{-1} of a-

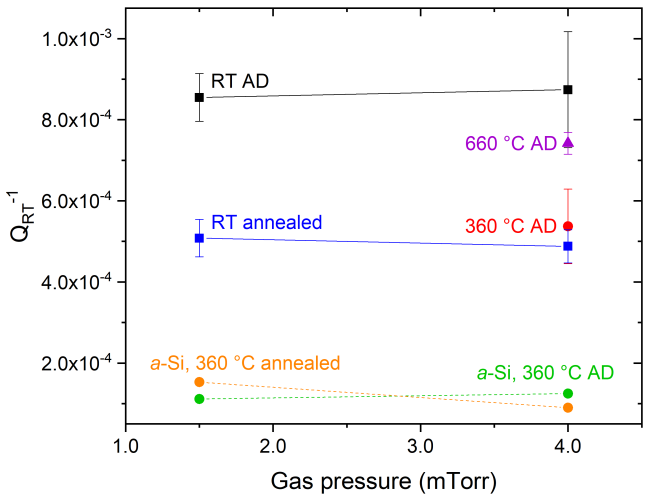

Figure 7.5: RT mechanical loss of MS a-$Si_{47}C_{53}$ grown at two Ar 1.5 and 4.0 mTorr, and RT, 360 °C and 660 °C, in their as-deposited and annealed states. The two dashed lines show the Q_{RT}^{-1} of MS 360 °C-grown a-Si in as-deposited (AD) state (green) and annealed state (orange).

$Si_{47}C_{53}$. Moreover, T_s has a much smaller influence on Q_0^{-1} in *a*-$Si_{47}C_{53}$ compared to its impact on that in MS *a*-Si, which was in turn much less affected by T_s than e-beam *a*-Si where orders of magnitude improvement have been found [77].

7.3.3 Optical absorption

The optical absorption of *a*-$Si_{47}C_{53}$ films at wavelengths 1064 and 2000 nm, corrected for the interference effect of PCI (Appendix A) and normalized to a thickness of 300 nm, is shown in Table 7.1. The absorption level of all as-deposited samples is extremely high at these infrared wavelengths, reaching percentage levels, which is much higher than the ppm-level requirement. This high absorption is likely related to the significant presence of C–C sp^2 bonding in these films (ranging from 20 to 40%, as shown in Fig. 7.2), resembling the structure of graphite, which is a conductor.

There is an improvement in the optical absorption after vacuum annealing, which is consistent with the drop in C–C bonding, particularly sp^2 bonding, and post-hydrogenation. However, the reduction in absorption is not sufficient to surpass the absorption level achieved in *a*-Si films. It was found that regardless of the

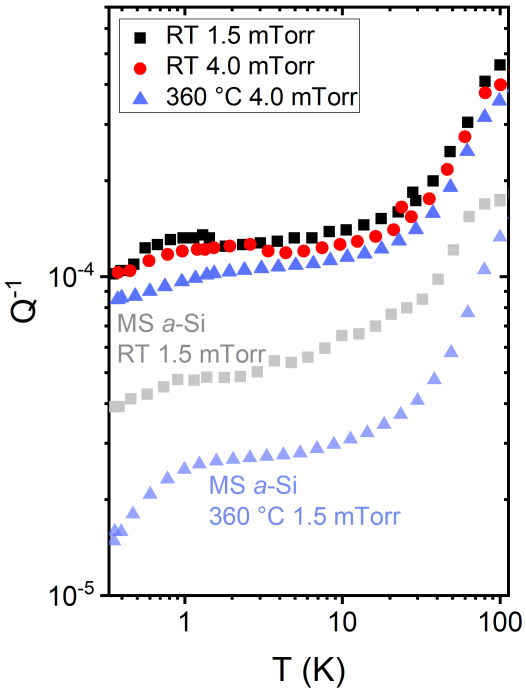

Figure 7.6: Low-temperature mechanical loss of a-$Si_{47}C_{53}$ grown at two Ar pressures, 1.5 and 4.0 mTorr, and RT and 360 °C, in their as-deposited states.

initial deposition conditions, all the studied *a*-$Si_{47}C_{53}$ films exhibit similar levels of absorption after annealing and post-H (Table 7.1). It is also worth noting that the reduction in absorption with post-growth processing in *a*-$Si_{47}C_{53}$ is much smaller compared to the improvement observed in *a*-Si:H films, which can be over one order of magnitude for RT-deposited films at both 1064 and 2000 nm (Table 6.2).

Deposition conditions	as-deposited		vacuum annealed		post-hydrogenated	
	1064 nm	2000 nm	1064 nm	2000 nm	1064 nm	2000 nm
RT Ar 1.5 mTorr	21.26	6.90	11.89	5.69	5.69	0.95
RT Ar 4.0 mTorr	16.66	6.91	15.18	5.36	5.79	0.86
360 °C Ar 4.0 mTorr	15.06	5.29			7.67	0.91

Table 7.1: Optical absorption of MS a-$Si_{47}C_{53}$ films of 300 nm thickness at two infrared wavelengths in %.

Attempts were made to increase the Si content in a-Si_xC_{1-x} to seek improvement in its infrared absorption by reducing the C–C sp^2 bonding fraction. The absorption characteristics of this sample were compared to those of pure a-Si and a-$Si_{47}C_{53}$, and the results are summarized in Table 7.2. Surprisingly, only the absorption at 1064 nm is reduced with the higher Si percentage compared to a-$Si_{47}C_{53}$, while the absorption at 2000 nm remains higher than that of a-$Si_{47}C_{53}$, and at all wavelengths, the absorption of a-Si_xC_{1-x} ($x = 0.47$ and 0.90) remains significantly higher compared to that of pure a-Si.

Sample information	Optical absorption (%)		
	1064 nm	1550 nm	2000 nm
a-Si		3.28	0.47
a-$Si_{47}C_{53}$	21.26		6.90
a-$Si_{90}C_{10}$	10.50	10.45	10.94

Table 7.2: Optical absorption of MS pure a-Si, a-$Si_{47}C_{53}$ and a-$Si_{90}C_{10}$ grown at RT and Ar 1.5 mTorr for a 300 nm-thick film, measured in their as-deposited form.

With vacuum annealing and post-hydrogenation, the absorption of the a-$Si_{90}C_{10}$ sample at 1550 and 2000 nm improved, as indicated in Table 7.3, but not at 1064 nm. However, it remains at the level of ∼1% (10^4 ppm), making it unsuitable for application in GW detector mirrors.

Sample state	Optical absorption (%)		
	1064 nm	1550 nm	2000 nm
as-deposited	10.50	10.45	10.94
vacuum annealed	31.50	4.58	6.91
post-hydrogenated	14.18	1.41	1.84

Table 7.3: Optical absorption of MS a-$Si_{90}C_{10}$ grown at RT and Ar 1.5 mTorr, measured in three different states, normalized to thickness of 300 nm.

We also performed in-situ hydrogenation on a-$Si_{47}C_{53}$ with Ar mixed with 0.5%, 1% and 5% of H_2 to compare with the post-H method. Our findings on a-$Si_{47}C_{53}$:H revealed that for films deposited at 360 °C and 4.0 mTorr, both in-situ and post-H methods led to reduced absorption at 1064 and 2000 nm, but as the concentration of H_2 approached the level used in post-hydrogenation (5% H_2 in N_2), the difference between the two methods becomes less pronounced, as illustrated in Fig. 7.7. This is different from what has been seen in MS a-Si:H, where the as-deposited, RT-grown Ar/5% H_2 in-situ H sample exhibits higher

absorption than the annealed and post-H sample initially prepared at RT using Ar, while in the high T-deposited samples, the as-deposited, 360 °C-grown in-situ H film shows lower absorption at 1550 and 2000 nm compared to the annealed, post-H sample deposited with pure Ar at 360 °C (Table 6.2).

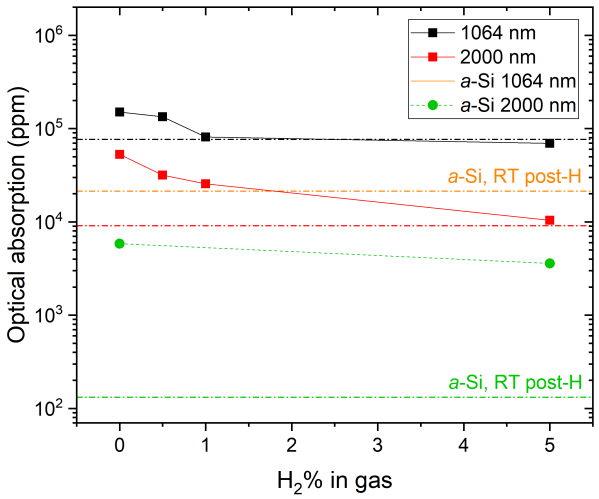

Figure 7.7: Optical absorption of MS in-situ H a-$Si_{47}C_{53}$ grown at 360°C and 4.0 mTorr, measured in the as-deposited state at 1064 and 2000 nm. The H_2 ratio in the working gas for in-situ H varies from 0.5% to 5%. The MS RT, 1.5 mTorr a-Si data from Sec. 6.3.5 is shown as orange (at 1064 nm) and green (at 2000 nm). The MS in-situ H a-Si:H samples are plotted against the same x-axis (data available only at 2000 nm). The black and red dashed lines represent the absorption at 1064 and 2000 nm respectively of equivalent samples deposited without in-situ H after post-H treatment.

7.4 Discussion

The bonding environment of a-Si_xC_{1-x} exhibits variations with different growth parameters and post-growth processing. Higher Ar pressure slightly favors the formation of Si–C bonds, and growing at elevated T_s and vacuum annealing both promote Si–C bond and C–C sp^3 formation. Changing the Si content in a-Si_xC_{1-x} has a greater influence on the bonding ratios, with a higher Si content promoting the formation of Si–Si and C–Si bonding, as shown in Fig. 7.3. This represents a larger proportion of sp^3 bonding in the network. However, the ratio of sp^2 to sp^3 C–C bonding in a-Si_xC_{1-x} shows no dependence on Si content (Fig. 7.4),

suggesting that connecting more C to Si has a limited influence on shifting the overall C–C bonding environment towards a higher proportion of tetrahedral sp^3 bonding.

The physical properties of a-Si_xC_{1-x}, including mechanical loss and optical absorption, exhibit less sensitivity to deposition conditions than a-Si. The higher mechanical loss observed in a-$Si_{47}C_{53}$ at both low temperatures and room temperature can be attributed to the presence of graphite-like C–C sp^2 bonds. These weaker bonds in a-$Si_{47}C_{53}$ make the material more susceptible to thermal activation of atomic movement and subsequent energy loss. This explains the higher Q_{RT}^{-1} in a-$Si_{47}C_{53}$ compared to a-Si at equivalent growth temperatures (Fig. 7.5). The low-T mechanical loss is also influenced by the C–C sp^2 bonds and defects resulting from the disruption of the Si bonding network caused by the addition of C. Increasing T_s promotes bonding between Si and C atoms, as shown in Fig. 7.3, which leads to slightly lower Q_0^{-1} in the 360 °C, Ar 4.0 mTorr a-$Si_{47}C_{53}$ sample compared to the RT-deposited samples (Fig. 7.6).

Vacuum annealing renders the same Q_{RT}^{-1} between a-$Si_{47}C_{53}$ samples deposited at RT and 360 °C, as shown in Fig. 7.5. However, it does not eliminate the difference in the Q_{RT}^{-1} between a-$Si_{47}C_{53}$ and a-Si, indicating that the higher loss observed in a-$Si_{47}C_{53}$ compared to a-Si is likely intrinsic to the material itself.

Both the RT-deposited a-$Si_{47}C_{53}$ and a-$Si_{90}C_{10}$ samples exhibit significantly higher absorption at infrared wavelengths compared to pure a-Si, and they show similar absorption levels at 2000 nm, despite being shown by experiments that adding C to Si would increase its band gap [149], which is confirmed by the observed transparency of a-$Si_{47}C_{53}$ under visible light (Fig. 7.1).

The band gap extracted by the Tauc plot, as reported in Ref. 149, mainly focuses on the large increase in the absorption coefficient near the Tauc band gap. However, for the three infrared wavelengths of interest in this work, we are examining the absorption occurring in the Urbach tail (Fig. 1.5). In fact, the optical absorption spectrum of all forms of amorphous carbon (a-C) shows a long tail, as depicted in Fig. 7.8 (a). Robertson discussed a cluster model proposed by Tagliaferro and coworkers [153–155] that potentially explains the broad absorption tail observed in a-C [156]. According to this model, the presence of C–C sp^2 bonding creates an inhomogeneous disorder within the network. Depending on the configuration of each sp^2 cluster, the band gap of each cluster varies, resulting in a broad absorption tail observed experimentally, as opposed to the sharp edge seen in a-Si.

Additionally, PECVD-grown a-Si_xC_{1-x}:H films have also been reported to ex-

hibit a broad absorption tail [157], with the breadth of the tail showing small variation with changes in the Si composition (Fig. 7.8 (b)). This finding further supports the notion of a similar inhomogeneous disorder in a-Si_xC_{1-x}, attributed to the presence of C–C sp^2 bonds, as observed in a-C. These results confirm our initial hypothesis that the presence of C–C sp^2 bonds in a-$Si_{47}C_{53}$ is responsible for the observed high absorption in the infrared wavelength range.

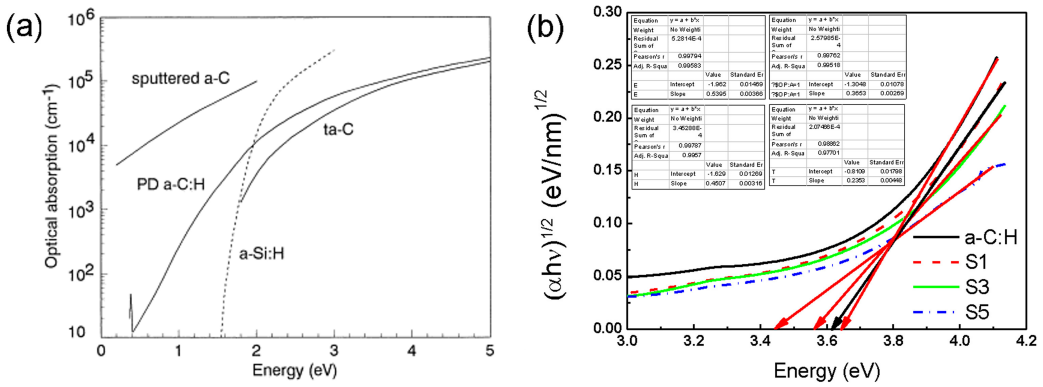

Figure 7.8: (a) Optical absorption spectra of sputtered a-C, tetrahedral amorphous carbon (ta-C), and an a-C:H film, compared to the sharper edge of a-Si:H [156]. (b) Tauc plot of PECVD-grown a-C:H and a-Si_xC_{1-x}:H films with various compositions (Si content of 21, 25 and 53 at.% for S1, S3 and S5 in the graph, respectively) [157]. The lines serve as guides for Tauc band gap extraction.

However, the a-$Si_{90}C_{10}$ sample, despite showing a relatively low ratio of C–C sp^2 to sp^3 bonds (Fig. 7.4), still exhibits very high absorption compared to MS a-Si deposited under similar conditions (Table 7.2). This suggests that the presence of C–C sp^2 bonds alone cannot explain the observed phenomenon. One possible explanation is that there are other localized electronic states contributing to the absorption in the infrared wavelength range. These states may arise from various defects, such as vacancies or disordered arrangements of Si and C atoms. Further investigation and characterization of the structural and optical properties of a-Si_xC_{1-x} films are needed to fully understand the mechanisms behind their high infrared absorption.

In contrast to a-Si, where hydrogen plays a crucial role in reducing optical absorption and mechanical loss, related to assisting the relaxation of the structure and enhancing its order, its impact on a-Si_xC_{1-x} appears to be small (Fig. 7.7). The smaller extent of improvement in optical absorption with hydrogenation suggests that hydrogen is less effective in removing the tail states responsible for photon

absorption. The structural features in a-Si_xC_{1-x} that create those sub-band gap states, such as C–C sp^2 bonds and defects caused by disorder, seem to be more resistant to hydrogen-induced atomic rearrangement. Consequently, the reduction in optical absorption achieved through hydrogenation in a-Si_xC_{1-x} is much less prominent than that in a-Si.

7.5 Summary

This chapter focused on the investigation of magnetron sputtered amorphous silicon carbide coatings. The bonding ratios of MS a-Si_xC_{1-x} were found to be somewhat influenced by deposition conditions such as substrate temperature and Ar pressure. The chemical composition had a greater impact on the bonding environment, with an increase in Si content favoring Si–C bonds but having a limited effect on the ratio of sp^2 (graphite-like) to sp^3 (diamond-like) bonding for C–C bonds.

The mechanical loss of MS a-$Si_{47}C_{53}$ was found to be higher than that of a-Si, at both low temperatures and room temperature; it shows minimal variation with working gas pressure and exhibits a smaller improvement with higher T_s compared to MS and e-beam a-Si. These findings suggest that the high mechanical loss of a-$Si_{47}C_{53}$ is likely intrinsic to the material, resulting from the disruption of the rigid, tetrahedral bonding network caused by the addition of C to Si.

Regarding optical absorption at infrared wavelengths, slight improvements were observed with higher T_s but not with changes in Ar pressure. Higher Si content (90 at.%) results in lower absorption at 1064 nm, while absorption at 2000 nm remains relatively unchanged compared to a-$Si_{47}C_{53}$. Overall, a-Si_xC_{1-x} exhibited higher absorption than a-Si at all three infrared wavelengths studied. We attributed this to the broad absorption edge associated with C–C sp^2 bonds.

In-situ hydrogenation was conducted using different concentrations of hydrogen gas mixed with argon. A comparison was made with post-hydrogenation, and it was observed that the difference in optical absorption between the two methods diminishes as the hydrogen concentration approached the level used in post-H. Further research efforts are essential to optimize the properties of a-Si_xC_{1-x} and enhance its performance to meet the stringent requirements of GW detector mirror coatings. Exploring PVD techniques known for promoting sp^3 bonding in ta-C, such as filtered cathodic vacuum arc [158] and pulsed laser deposition [159], may offer opportunities to grow a-Si_xC_{1-x} films with an improved sp^3 bonding ratio. This enhancement in sp^3 bonding could potentially lead to lower mechani-

cal loss at both cryogenic temperatures and room temperature, a sharper optical absorption edge, and as a result, lower optical absorption at infrared wavelengths.

CHAPTER 8

CONCLUSIONS AND FUTURE WORK

8.1 Conclusions

Finding new coating materials, particularly high-refractive-index materials with low thermal noise, low optical absorption, and low scattering, is crucial for enhancing the sensitivity and performance of interferometric gravitational-wave detectors. These materials must possess low mechanical loss to minimize thermal noise in GW detection. Additionally, achieving low optical absorption in mirror coatings is important as it minimizes the conversion of light energy into heat. This is vital for preserving the stability and precision of interferometric measurements, as absorbed energy introduces thermal fluctuations and noise into the system. The development of novel high-index coating materials with enhanced mechanical and optical properties, compared to the current material *a*-Ti:Ta_2O_5, holds significant potential for advancing GW detection, enabling more precise measurements and a deeper understanding of astrophysical phenomena that give rise to these elusive signals.

This study examined the structural and mechanical properties of amorphous silicon (*a*-Si), hydrogenated amorphous silicon (*a*-Si:H), and amorphous silicon carbide (*a*-SiC) films grown using magnetron sputtering, a PVD technique. We aimed to explore the potential of *a*-Si as a material for GW detectors, both at cryogenic temperatures (e.g. LIGO Voyager, KAGRA and Einstein Telescope) and at room temperature (e.g. LIGO and Virgo). Our objective was to investigate how various deposition parameters, such as working gas, sputtering pressure, substrate temperature, and post-growth treatments like vacuum annealing and post-hydrogenation, could improve the relevant properties for GW detectors, particularly mechanical loss and optical absorption at infrared wavelengths. *a*-Si has shown low mechanical loss at cryogenic temperatures, making it promising for high-index coating layers, as proposed in the LIGO Voyager design. We aimed to further reduce its loss, ideally at both low temperatures and room temperature. Moreover, the high infrared absorption of *a*-Si has limited its use in upgrading the current LIGO detectors. By studying hydrogenation and carbon addition in

a-Si, we sought to explore the potential for enabling its use not only in cryogenic GW detectors with longer operating wavelengths, but also in upgrading existing GW detectors, possibly through multimaterial coating designs.

The choice of working gas and its pressure significantly impacts the properties of the deposited films by affecting the kinetic energy of sputtered atoms when they reach the substrate. Different PVD techniques have different energy levels per incoming particle, ranging from thermal energies in electron-beam evaporation ($\sim$10's of meV per atom) to much higher energies in magnetron sputtering (typically 100 times higher than e-beam) and even higher energies in ion-beam sputtering (up to 1000 times higher than magnetron sputtering). Energetic incoming atoms lead to compressive macroscopic stress and film densification, known as the atomic peening effect. The dominant defects transition from nanovoids in e-beam *a*-Si to divacancies and self-interstitials in MS *a*-Si. By selecting appropriate working gases and deposition conditions, such as low gas pressure, it is possible to suppress the formation of open-volume defects, supported by the overdensity seen in MS RT, Ar 1.5 and 2.0 mTorr *a*-Si. Additionally, the structural order of the film is enhanced by growing at low gas pressure and high substrate temperature, as reflected by a reduction in bond angle deviation compared to the tetrahedral angle.

Increasing the incident atom kinetic energy, in conjunction with high growth temperature, improves both the low-temperature and room-temperature mechanical loss. However, there seems to be a limit to the improvement in the RT loss, while the low-T loss shows potential for further enhancement. Vacuum annealing has a smaller effect on the structural properties compared to high-T deposition, as well as on the low-T mechanical loss. However, it appears to reduce the RT mechanical loss to a similar level as depositing at high substrate temperature.

We propose that defects, such as divacancies and self-interstitials in MS *a*-Si, give rise to the formation of tunneling two-level systems, which contribute to the energy dissipation at cryogenic temperatures. In contrast, the RT mechanical loss is influenced by the rigidity of the bonding network, which is determined by the stiffness of bonds and the flexibility of movement of individual atoms, which is either enabled or suppressed by their proximity to defects and neighboring atoms.

The introduction of hydrogen to *a*-Si was found to greatly reduce its optical absorption at infrared wavelengths and RT mechanical loss, with both in-situ and post-hydrogenation being found effective. We propose that hydrogen serves a dual role in *a*-Si:H, acting as a passivating agent for dangling bonds (specifically enabled by high temperatures) and facilitating the relaxation of the Si bonding network. The mechanism by which hydrogen promotes structural reorganization

involves acting as a catalyst, effectively reducing the energy barrier for atomic rearrangement and facilitating the elimination of strained Si–Si bonds that may contribute to the creation of electronic states near the band edges. It is worth noting that the reduction in optical absorption is not solely dependent on hydrogen content and structural ordering, which indicates the involvement of other structural features in the formation of localized states within the band gap.

The incorporation of carbon in MS *a*-SiC films results in higher mechanical loss and optical absorption compared to pure *a*-Si films. This can be attributed to the presence of graphite-like C–C sp^2 bonds, which results in increased energy dissipation and photon absorption. The observed mechanical loss is inherent to the material itself and is minimally affected by deposition conditions. The bonding environment in *a*-SiC is influenced by its composition, with higher silicon content favoring Si–Si and Si–C bonding. However, despite increased Si content, there is only a slight improvement in the proportion of tetrahedral sp^3 bonding in C–C bonding. Enhancing the formation of C–C sp^3 bonding is crucial to fully unlock the potential of *a*-SiC for use in GW detector mirror coatings, as the poor performance of *a*-SiC is likely caused by C–C sp^2 bonding.

In conclusion, this research provides valuable insights into the underlying mechanisms of mechanical loss at low temperatures and room temperature, as well as optical absorption at infrared wavelengths, in *a*-Si-related materials. Furthermore, it offers potential solutions for optimizing the performance of *a*-Si-based coatings to be utilized in GW detector mirrors. These findings contribute to the development of improved coating materials with low mechanical loss and low optical absorption, ultimately enhancing the sensitivity and precision of GW measurements.

8.2 Future work

The following are some potential directions for future investigations:

- We have shown that increasing the kinetic energy of incident atoms, in combination with high-T deposition, reduces mechanical loss at low temperatures. Furthermore, we have not observed any plateauing in the value of Q_0^{-1} as the kinetic energy of incident atoms increases. Based on these findings, it is worthwhile to explore the deposition of *a*-Si using other PVD techniques that provide more energy to the Si adatoms, such as ion-beam sputtering, in which the gas ions are directed towards the target and are mostly separated from the sputtered atoms. By selecting a gas with a similar atomic weight to Si and utilizing a high accelerating voltage, it may be

possible to further improve the Q_0^{-1} of sputtered a-Si with a higher incident atom kinetic energy, potentially approaching the values achieved with e-beam a-Si grown at high substrate temperature.

- The study on MS a-Si:H has demonstrated the effectiveness of hydrogenation of Si, both in-situ and post-hydrogenation, on improving both its mechanical and optical properties. Future studies may attempt a higher H_2 ratio in the working gas to seek a larger reduction in both low-T and RT mechanical loss and infrared absorption. In addition, since post-hydrogenation serves the same purpose as vacuum annealing, which is to induce structural relaxation, the annealing step of a-Si:H might be skipped or replaced by longer hours of post-H. This requires further investigation.

- In the design of GW mirror coating stacks, it is important to consider the treatment of high-index and low-index layers together after growth. The impact of post-growth treatments, such as annealing and post-hydrogenation, which are effective on the high-index a-Si layers, should not be neglected for the low-index layers. Therefore, it is essential to understand their effects on the low-index layers, for example the currently used a-SiO_2, to properly evaluate the overall performance of the coating stack and make sure that the final coating meets the necessary requirements.

- This work primarily focused on investigating the optical absorption of a-Si:H. However, it is important to note that the refractive index of the coatings is also a crucial parameter in mirror coating design. A higher refractive index in the coating layers allows for thinner layers to achieve the same reflectivity, reducing the contribution of thermal noise from the coating stack, as thermal noise is proportional to film thickness. Therefore, valuable information on the refractive index of the samples could be obtained through ellipsometry measurements in the infrared wavelength range. It would also be useful to obtain a full optical spectrum over the infrared wavelengths and the near-visible light range (showing the rapid increase in absorption coefficient), which may reveal any absorption peaks related to defects in a-Si:H beyond the Urbach tail. Moreover, conducting optical absorption measurements at low temperatures would also shed light on the absorption mechanisms responsible for infrared wavelengths in a-Si:H, and offer essential data for cryogenic GW detectors like LIGO Voyager. In summary, conducting these experiments would provide a comprehensive understanding of the optical properties of a-Si:H.

BIBLIOGRAPHY

[1] A. Einstein. Die grundlage der allgemeinen relativitätstheorie. *Annalen der Physik*, 354(7):769–822, 1916.

[2] Peter R Saulson. *Fundamentals of Interferometric Gravitational Wave Detectors*. WORLD SCIENTIFIC, 1994.

[3] Kazuaki Kuroda, Wei-Tou Ni, and Wei-Ping Pan. Gravitational waves: Classification, methods of detection, sensitivities and sources. *International Journal of Modern Physics D*, 24(14):1530031, 2015.

[4] J. Weber. Detection and generation of gravitational waves. *Phys. Rev.*, 117:306–313, Jan 1960.

[5] Richard L. Garwin and James L. Levine. Single gravity-wave detector results contrasted with previous coincidence detections. *Phys. Rev. Lett.*, 31:176–180, Jul 1973.

[6] J. H. Taylor, L. A. Fowler, and P. M. McCulloch. Measurements of general relativistic effects in the binary pulsar PSR1913+16. *Nature*, 277(5696):437–440, 1979.

[7] J. Weisberg and J. Taylor. The Relativistic Binary Pulsar B1913+16: Thirty Years of Observations and Analysis. 08 2004.

[8] R A Hulse and J H Taylor. Discovery of a pulsar in a binary system. *Astrophys. J., Lett., v. 195, no. 2, pp. L51-L53.*

[9] J. H. Taylor, R. A. Hulse, L. A. Fowler, G. E. Gullahorn, and J. M. Rankin. Further observations of the binary pulsar PSR 1913+16. , 206:L53–L58, May 1976.

[10] J. H. Taylor and J. M. Weisberg. A new test of general relativity - Gravitational radiation and the binary pulsar PSR 1913+16. , 253:908–920, February 1982.

[11] J Aasi et al. Advanced LIGO. *Classical and Quantum Gravity*, 32(7):074001, 4 2015.

[12] F. Acernese et al. Advanced Virgo: a second-generation interferometric gravitational wave detector. *Classical and Quantum Gravity*, 32(2):024001, 1 2015.

[13] H Grote and (for the LIGO Scientific Collaboration). The GEO 600 status. *Classical and Quantum Gravity*, 27(8):084003, apr 2010.

[14] T. Akutsu, M. Ando, K. Arai, Y. Arai, S. Araki, A. Araya, N. Aritomi, H. Asada, Y. Aso, S. Atsuta, and et al. Kagra: 2.5 generation interferometric gravitational wave detector. *Nature Astronomy*, 3(1):35–40, 2019.

[15] Stuart Reid and Iain W Martin. Development of Mirror Coatings for Gravitational Wave Detectors. 2016.

[16] R. W. P. Drever, J. Hought, A. J. Munley, S.-A. Lee, R. Spero, S. E. Whitcomb, H. Ward, G. M. Ford, M. Hereld, N. A. Robertson, I. Kerr, J. R. Pugh, G. P. Newton, B. Meers, E. D. Brooks, and Y. Gursel. *Gravitational Wave Detectors Using Laser Interferometers and Optical Cavities: Ideas, Principles and Prospects*, pages 503–514. Springer US, Boston, MA, 1983.

[17] Gravitational Wave Interferometer Noise Calculator, `https://git.ligo.org/gwinc/pygwinc`, Accessed: 2023-06-04.

[18] M Beccaria, M Bernardini, S Braccini, C Bradaschia, A Bozzi, C Casciano, G Cella, A Ciampa, E Cuoco, G Curci, E D'Ambrosio, V Dattilo, G De Carolis, R De Salvo, A Di Virgilio, A Delapierre, D Enard, A Errico, G Feng, I Ferrante, F Fidecaro, F Frasconi, A Gaddi, A Gennai, G Gennaro, A Giazotto, P La Penna, G Losurdo, M Maggiore, S Mancini, F Palla, H B Pan, F Paoletti, A Pasqualetti, R Passaquieti, D Passuello, R Poggiani, P Popolizio, F Raffaelli, S Rapisarda, A Viceré, and Z Zhang. Relevance of newtonian seismic noise for the Virgo interferometer sensitivity. *Classical and Quantum Gravity*, 15(11):3339, nov 1998.

[19] Peter R. Saulson. Terrestrial gravitational noise on a gravitational wave antenna. *Phys. Rev. D*, 30:732–736, Aug 1984.

[20] B. Sathyaprakash et al. Scientific Objectives of Einstein Telescope. 2012.

[21] M Armano et al. The LISA Pathfinder Mission. *Journal of Physics: Conference Series*, 610(1):012005, apr 2015.

[22] W A Edelstein, J Hough, J R Pugh, and W Martin. Limits to the measurement of displacement in an interferometric gravitational radiation detector. *Journal of Physics E: Scientific Instruments*, 11(7):710, jul 1978.

[23] Carlton M. Caves. Quantum-mechanical noise in an interferometer. *Phys. Rev. D*, 23:1693–1708, Apr 1981.

[24] J. Aasi et al. Enhanced sensitivity of the LIGO gravitational wave detector by using squeezed states of light. *Nature Photonics*, 7(8):613–619, 2013.

[25] Gregory M. Harry, Andri M. Gretarsson, Peter R. Saulson, Scott E. Kittelberger, Steven D. Penn, William J. Startin, Sheila Rowan, Martin M. Fejer, D. R.M. Crooks, Gianpietro Cagnoli, Jim Hough, and Norio Nakagawa. Thermal noise in interferometric gravitational wave detectors due to dielectric optical coatings. *Classical and Quantum Gravity*, 19(5):897–917, 2002.

[26] Rana X. Adhikari. Gravitational radiation detection with laser interferometry. *Rev. Mod. Phys.*, 86:121–151, Feb 2014.

[27] Garrett D. Cole, Wei Zhang, Michael J. Martin, Jun Ye, and Markus Aspelmeyer. Tenfold reduction of brownian noise in high-reflectivity optical coatings. *Nature Photonics*, 7(8):644–650, 2013.

[28] Steven D. Penn, Maya M. Kinley-Hanlon, Ian A. O. MacMillan, Paula Heu, David Follman, Christoph Deutsch, Garrett D. Cole, and Gregory M. Harry. Mechanical ringdown studies of large-area substrate-transferred GaAs/AlGaAs crystalline coatings. *J. Opt. Soc. Am. B*, 36(4):C15–C21, Apr 2019.

[29] P. W. Anderson. Absence of diffusion in certain random lattices. *Phys. Rev.*, 109:1492–1505, Mar 1958.

[30] Franz Urbach. The long-wavelength edge of photographic sensitivity and of the electronic absorption of solids. *Phys. Rev.*, 92:1324–1324, Dec 1953.

[31] Sadao Adachi. *Optical properties of crystalline and amorphous semiconductors: Materials and fundamental principles*. Kluwer Academic Publishers, 1999.

[32] D. L. Wood and J. Tauc. Weak absorption tails in amorphous semiconductors. *Phys. Rev. B*, 5:3144–3151, Apr 1972.

[33] J. Tauc. Optical properties and electronic structure of amorphous ge and si. *Materials Research Bulletin*, 3(1):37–46, 1968.

[34] Sándor Kugler and Koichi Shimakawa. *Electronic structure*, page 86–116. Cambridge University Press, 2015.

[35] I. Milostnaya, T. Allen, F. Gaspari, N.P. Kherani, D. Yeghikyan, W.L. Roes, T. Kosteski, and S. Zukotynski. Electrical and optical properties of amorphous and microcrystalline hydrogenated silicon films deposited using saddle field glow discharge. *MRS Proceedings*, 762, 2003.

[36] A. S. Nowick, B. S. Berry, and J. Lawrence Katz. Anelastic Relaxation in Crystalline Solids. *Journal of Applied Mechanics*, 42(3):750–751, 09 1975.

[37] Peter R. Saulson. Thermal noise in mechanical experiments. *Phys. Rev. D*, 42:2437–2445, Oct 1990.

[38] K. S. Gilroy and W. A. Phillips. An asymmetric double-well potential model for structural relaxation processes in amorphous materials. *Philosophical Magazine B*, 43(5):735–746, 1981.

[39] W. A. Phillips. Tunneling states in amorphous solids. *Journal of Low Temperature Physics*, 7(3-4):351–360, 1972.

[40] P. W. Anderson, B. I. Halperin, and C. M. Varma. Anomalous low-temperature thermal properties of glasses and spin glasses. *Philosophical Magazine*, 25(1):1–9, 1972.

[41] R X Adhikari et al. A cryogenic silicon interferometer for gravitational-wave detection. *Classical and Quantum Gravity*, 37(16):165003, 2020.

[42] Scott A. Hughes. Listening to the universe with gravitational-wave astronomy. *Annals of Physics*, 303(1):142–178, 2003.

[43] Robert Brown. Xxvii. a brief account of microscopical observations made in the months of june, july and august 1827, on the particles contained in the pollen of plants; and on the general existence of active molecules in organic and inorganic bodies. *The Philosophical Magazine*, 4(21):161–173, 1828.

[44] A. Einstein. Über die von der molekularkinetischen theorie der wärme geforderte bewegung von in ruhenden flüssigkeiten suspendierten teilchen. *Annalen der Physik*, 322(8):549–560, 1905.

[45] Herbert B. Callen and Theodore A. Welton. Irreversibility and generalized noise. *Phys. Rev.*, 83:34–40, Jul 1951.

[46] Herbert B. Callen and Richard F. Greene. On a theorem of irreversible thermodynamics. *Phys. Rev.*, 86:702–710, Jun 1952.

[47] R Kubo. The fluctuation-dissipation theorem. *Reports on Progress in Physics*, 29(1):255, jan 1966.

[48] Levin Yu. Internal thermal noise in the LIGO test masses: A direct approach. *Physical Review D - Particles, Fields, Gravitation and Cosmology*, 57(2):1–4, 1998.

[49] Thomas Kessler, Thomas Legero, and Uwe Sterr. Thermal noise in optical cavities revisited. *Journal of the Optical Society of America B*, 29(1):178, 2012.

[50] Clarence Zener. Internal Friction in Solids. I. Theory of Internal Friction in Reeds. *Physical Review*, 52(3):230–235, 8 1937.

[51] Clarence Zener. Internal Friction in Solids. II. General Theory of Thermoelastic Internal Friction. *Physical Review*, 53(1):90–99, 1 1938.

[52] Ron Lifshitz and M. L. Roukes. Thermoelastic damping in micro- and nanomechanical systems. *Physical Review B*, 61(8):5600–5609, 2 2000.

[53] S.J. Wong, C.H.J. Fox, and S. McWilliam. Thermoelastic damping of the in-plane vibration of thin silicon rings. *Journal of Sound and Vibration*, 293(1-2):266–285, 5 2006.

[54] Surabhi Joshi, Sherman Hung, and Srikar Vengallatore. Design strategies for controlling damping in micromechanical and nanomechanical resonators. *EPJ Techniques and Instrumentation*, 1(1):5, 12 2014.

[55] M. M. Fejer, S. Rowan, G. Cagnoli, D. R.M. M. Crooks, A. Gretarsson, G. M. Harry, J. Hough, S. D. Penn, P. H. Sneddon, and S. P. Vyatchanin. Thermoelastic dissipation in inhomogeneous media: Loss measurements and displacement noise in coated test masses for interferometric gravitational wave detectors. *Physical Review D*, 70(8):1–19, 10 2004.

[56] Kentaro Somiya and Kazuhiro Yamamoto. Coating thermal noise of a finite-size cylindrical mirror. *Physical Review D*, 79(10):102004, 5 2009.

[57] Thomas H. Metcalf and Xiao Liu. An ultra-high Q silicon compound cantilever resonator for Young's modulus measurements. *Review of Scientific Instruments*, 84(7), 07 2013. 075001.

[58] R Nawrodt, C Schwarz, S Kroker, I W Martin, R Bassiri, F Brückner, L Cunningham, G D Hammond, D Heinert, J Hough, T Käsebier, E-B Kley, R Neubert, S Reid, S Rowan, P Seidel, and A Tünnermann. Investigation of mechanical losses of thin silicon flexures at low temperatures. *Classical and Quantum Gravity*, 30(11):115008, may 2013.

[59] R Zhou, M Molina-Ruiz, and F Hellman. Strategies to reduce the thermoelastic loss of multimaterial coated finite substrates. *Classical and Quantum Gravity*, 40(14):144001, jun 2023.

[60] V.B. Braginsky, M.L. Gorodetsky, and S.P. Vyatchanin. Thermo-refractive noise in gravitational wave antennae. *Physics Letters A*, 271(5):303–307, 2000.

[61] Clarence Zener. *Elasticity and Anelasticity of metals*. University of Chicago Press, 1965.

[62] D. R. Queen, X. Liu, J. Karel, T. H. Metcalf, and F. Hellman. Excess specific heat in evaporated amorphous silicon. *Physical Review Letters*, 110(13):135901, 3 2013.

[63] D. R. Queen, X. Liu, J. Karel, H. C. Jacks, T. H. Metcalf, and F. Hellman. Two-level systems in evaporated amorphous silicon. *Journal of Non-Crystalline Solids*, 426:19–24, 2015.

[64] R. C. Zeller and R. O. Pohl. Thermal Conductivity and Specific Heat of Noncrystalline Solids. *Physical Review B*, 4(6):2029–2041, 9 1971.

[65] Daniel Robert Queen. *The specific heat of pure and hydrogenated amorphous silicon*. PhD thesis, 2011.

[66] Grigorij J. Grabovskij, Torben Peichl, Jürgen Lisenfeld, Georg Weiss, and Alexey V. Ustinov. Strain tuning of individual atomic tunneling systems detected by a superconducting qubit. *Science*, 338(6104):232–234, 2012.

[67] Clemens Müller, Jared H Cole, and Jürgen Lisenfeld. Towards understanding two-level-systems in amorphous solids: insights from quantum circuits. *Reports on Progress in Physics*, 82(12):124501, oct 2019.

[68] B. E. White and R. O. Pohl. Internal friction of subnanometer a-SiO_2 films. *Physical Review Letters*, 75(24):4437–4439, 1995.

[69] Michael W. Klein, Baruch Fischer, A. C. Anderson, and P. J. Anthony. Strain interactions and the low-temperature properties of glasses. *Phys. Rev. B*, 18:5887–5891, Nov 1978.

[70] J. J. Freeman and A. C. Anderson. Thermal conductivity of amorphous solids. *Phys. Rev. B*, 34:5684–5690, Oct 1986.

[71] Clare C. Yu. Interacting defect model of glasses: Why do phonons go so far? *Phys. Rev. Lett.*, 63:1160–1163, Sep 1989.

[72] Anthony J. Leggett. Amorphous materials at low temperatures: why are they so similar? *Physica B: Condensed Matter*, 169(1):322–327, 1991.

[73] S. N. Coppersmith. Frustrated interactions and tunneling: Two-level systems in glasses. *Phys. Rev. Lett.*, 67:2315–2318, Oct 1991.

[74] G. K. White and M. L. Minges. Thermophysical properties of some key solids: An update. *Int. J. Thermophys.*, 18(5):1269–1327, 1997.

[75] Thomas Middelmann, Alexander Walkov, Guido Bartl, and René Schödel. Thermal expansion coefficient of single-crystal silicon from 7 K to 293 K. *Phys. Rev. B*, 92(17):174113, 2015.

[76] Xiao Liu, B. E. White, R. O. Pohl, E. Iwanizcko, K. M. Jones, A. H. Mahan, B. N. Nelson, R. S. Crandall, and S. Veprek. Amorphous solid without low energy excitations. *Physical Review Letters*, 78(23):4418–4421, 1997.

[77] Xiao Liu, Daniel R. Queen, Thomas H. Metcalf, Julie E. Karel, and Frances Hellman. Hydrogen-free amorphous silicon with no tunneling states. *Physical Review Letters*, 113(2):1–5, 2014.

[78] Manel Molina-Ruiz, Y. J. Rosen, H. C. Jacks, M. R. Abernathy, T. H. Metcalf, X. Liu, J. L. DuBois, and F. Hellman. Origin of mechanical and dielectric losses from two-level systems in amorphous silicon. *Physical Review Materials*, 5(3):035601, 3 2021.

[79] Martin A. Green and Mark J. Keevers. Optical properties of intrinsic silicon at 300 k. *Progress in Photovoltaics: Research and Applications*, 3(3):189–192, 1995.

[80] M. Vaněček, A. Poruba, Z. Remeš, N. Beck, and M. Nesládek. Optical properties of microcrystalline materials. *Journal of Non-Crystalline Solids*, 227-230:967–972, 1998.

[81] D. T. Pierce and W. E. Spicer. Electronic structure of amorphous si from photoemission and optical studies. *Phys. Rev. B*, 5:3017–3029, Apr 1972.

[82] G. D. Cody, T. Tiedje, B. Abeles, B. Brooks, and Y. Goldstein. Disorder and the optical-absorption edge of hydrogenated amorphous silicon. *Physical Review Letters*, 47(20):1480–1483, 1981.

[83] Saravanapriyan Sriraman, Sumit Agarwal, Eray S. Aydil, and Dimitrios Maroudas. Mechanism of hydrogen-induced crystallization of amorphous silicon. *Nature*, 418(6893):62–65, 2002.

[84] Mayur Valipa, Saravanapriyan Sriraman, Eray Aydil, and Dimitrios Maroudas. Hydrogen-induced crystallization of amorphous Si thin films. II. Mechanisms and energetics of hydrogen insertion into Si–Si bonds. *Journal of Applied Physics*, 100:053515–053515, 09 2006.

[85] Saravanapriyan Sriraman, Mayur S. Valipa, Eray S. Aydil, and Dimitrios Maroudas. Hydrogen-induced crystallization of amorphous silicon thin films. I. Simulation and analysis of film postgrowth treatment with H_2 plasmas. *Journal of Applied Physics*, 100(5), 09 2006. 053514.

[86] P. A. Khomyakov, Wanda Andreoni, N. D. Afify, and Alessandro Curioni. Large-scale simulations of a-Si:H: The origin of midgap states revisited. *Physical Review Letters*, 107(25):1–4, 2011.

[87] I Martin, H Armandula, C Comtet, M M Fejer, A Gretarsson, G Harry, J Hough, J-M M Mackowski, I MacLaren, C Michel, J-L Montorio, N Morgado, R Nawrodt, S Penn, S Reid, A Remillieux, R Route, S Rowan, C Schwarz, P Seidel, W Vodel, and A Zimmer. Measurements of a low-temperature mechanical dissipation peak in a single layer of ta2o5 doped with tio2. *Classical and Quantum Gravity*, 25(5):055005, feb 2008.

[88] I W Martin, R Nawrodt, K Craig, C Schwarz, R Bassiri, G Harry, J Hough, S Penn, S Reid, R Robie, and S Rowan. Low temperature mechanical dissipation of an ion-beam sputtered silica film. *Classical and Quantum Gravity*, 31(3):035019, jan 2014.

[89] H. C. Jacks, M. Molina-Ruiz, M. H. Weber, J. J. Maldonis, P. M. Voyles, M. R. Abernathy, T. H. Metcalf, X. Liu, and F. Hellman. Structural tunability and origin of two-level systems in amorphous silicon. *Physical Review Materials*, 6(4):1–27, 2022.

[90] Peter G. Murray, Iain W. Martin, Kieran Craig, James Hough, Raymond Robie, Sheila Rowan, Matt R. Abernathy, Teal Pershing, and Steven Penn. Ion-beam sputtered amorphous silicon films for cryogenic precision measurement systems. *Physical Review D*, 92(6):062001, 9 2015.

[91] J. Steinlechner, I. W. Martin, A. S. Bell, J. Hough, M. Fletcher, P. G. Murray, R. Robie, S. Rowan, and R. Schnabel. Silicon-Based Optical Mirror Coatings for Ultrahigh Precision Metrology and Sensing. *Physical Review Letters*, 120(26):263602, 2018.

[92] Xiao Liu, Matthew R. Abernathy, Thomas H. Metcalf, Battogtokh Jugdersuren, James C. Culbertson, Manel Molina-Ruiz, and Frances Hellman. Comparing amorphous silicon prepared by electron-beam evaporation and sputtering toward eliminating atomic tunneling states. *Journal of Alloys and Compounds*, 855:157431, 2021.

[93] M. Molina-Ruiz, H. C. Jacks, D. R. Queen, T. H. Metcalf, X. Liu, and F. Hellman. Decoupling between propagating acoustic waves and two-level

systems in hydrogenated amorphous silicon. *Physical Review B*, 104(2):1–14, 2021.

[94] M Granata, A Amato, L Balzarini, M Canepa, J Degallaix, D Forest, V Dolique, L Mereni, C Michel, L Pinard, B Sassolas, J Teillon, and G Cagnoli. Amorphous optical coatings of present gravitational-wave interferometers. *Classical and Quantum Gravity*, 37(9):095004, apr 2020.

[95] M. Molina-Ruiz, A. Markosyan, R. Bassiri, M. M. Fejer, M. Abernathy, T. H. Metcalf, X. Liu, G. Vajente, A. Ananyeva, and F." Hellman. Hydrogen-induced ultra-low optical absorption and mechanical loss in amorphous silicon for gravitational-wave detectors. 2023.

[96] Jessica Steinlechner, Iain W. Martin, Riccardo Bassiri, Angus Bell, Martin M. Fejer, Jim Hough, Ashot Markosyan, Roger K. Route, Sheila Rowan, and Zeno Tornasi. Optical absorption of ion-beam sputtered amorphous silicon coatings. *Physical Review D*, 93(6):1–9, 2016.

[97] Jessica Steinlechner, Iain W. Martin, Jim Hough, Christoph Krüger, Sheila Rowan, and Roman Schnabel. Thermal noise reduction and absorption optimization via multimaterial coatings. *Physical Review D*, 91(4):042001, 2 2015.

[98] D. T. Pierce and W. E. Spicer. Electronic Structure of Amorphous Si from Photoemission and Optical Studies. *Phys. Rev. B*, 5(8):3017, 1972.

[99] Michael A. Lieberman and Alan J. Lichtenberg. *Principles of plasma discharges and Materials Processing, 2nd edition.* John Wiley amp; Sons, 2005.

[100] Benjamin K. Derby, Terry G. Holesinger, James A. Valdez, Blas P. Uberuaga, and Cortney R. Kreller. Microstructural analysis of novel $Gd_2Ti_2O_7$ thin films processed via sputter deposition. *Materials Design*, 199:109430, 2021.

[101] P. C. Zalm. Energy dependence of the sputtering yield of silicon bombarded with neon, argon, krypton, and xenon ions. *Journal of Applied Physics*, 54(5):2660–2666, 1983.

[102] Nastja Mahne, Miha Čekada, and Matjaž Panjan. Total and differential sputtering yields explored by SRIM simulations. *Coatings*, 12(10), 2022.

[103] John A. Thornton and James L. Lamb. Substrate heating rates for planar and cylindrical-post magnetron sputtering sources. *Thin Solid Films*, 119(1):87–95, 1984.

[104] John A. Thornton and D. W. Hoffman. Stress-related effects in thin films. *Thin Solid Films*, 171(1):5–31, 1989.

[105] Y.G Shen. Effect of deposition conditions on mechanical stresses and microstructure of sputter-deposited molybdenum and reactively sputter-deposited molybdenum nitride films. *Materials Science and Engineering: A*, 359:158–167, 10 2003.

[106] D. W. Hoffman and John A. Thornton. Internal stresses in Cr, Mo, Ta, and Pt films deposited by sputtering from a planar magnetron source. *Journal of Vacuum Science and Technology*, 20(3):355–358, 03 1982.

[107] K. Takimoto, A. Fukuta, Y. Yamamoto, N. Yoshida, T. Itoh, and S. Nonomura. Linear thermal expansion coefficients of amorphous and microcrystalline silicon films. *Journal of Non-Crystalline Solids*, 299-302:314–317, 2002. 19th International Conference on Amorphous and Microcrystalline Semiconductors.

[108] Matej Mayer. SIMNRA User ' s Guide, 1997.

[109] George Gerald Stoney. The tension of metallic films deposited by electrolysis. *Proc. R. Soc. London, Ser. A*, 82(553):172–175, 1909.

[110] L. B. Freund and Subra Suresh. *Thin film materials: Stress, defect formation and surface evolution*. Cambridge University Press, 2003.

[111] D. Beeman, R. Tsu, and M. F. Thorpe. Structural information from the Raman spectrum of amorphous silicon. *Physical Review B*, 32(2):874–878, 1985.

[112] David A. Strubbe, Eric C. Johlin, Timothy R. Kirkpatrick, Tonio Buonassisi, and Jeffrey C. Grossman. Stress effects on the Raman spectrum of an amorphous material: Theory and experiment on a-Si:H. *Physical Review B - Condensed Matter and Materials Physics*, 92(24):1–6, 2015.

[113] B. Lesiak, L. Kövér, J. Tóth, J. Zemek, P. Jiricek, A. Kromka, and N. Rangam. C sp^2/sp^3 hybridisations in carbon nanomaterials – XPS and (X)AES study. *Applied Surface Science*, 452:223–231, 2018.

[114] Toshiro Maruyama and Shunsuke Mitani. The network structure of amorphous silicon–carbon alloy. *Journal of Non-Crystalline Solids*, 319(3):219–224, 2003.

[115] E. Cesarini, M. Lorenzini, E. Campagna, F. Martelli, F. Piergiovanni, F. Vetrano, G. Losurdo, and G. Cagnoli. A "gentle" nodal suspension for measurements of the acoustic attenuation in materials. *Review of Scientific Instruments*, 80(5), 2009.

[116] Tianjun Li, Felipe A. Aguilar Sandoval, Mickael Geitner, Ludovic Bellon, Gianpietro Cagnoli, Jérôme Degallaix, Vincent Dolique, Raffaele Flaminio, Danièle Forest, Massimo Granata, Christophe Michel, Nazario Morgado, and Laurent Pinard. Measurements of mechanical thermal noise and energy dissipation in optical dielectric coatings. *Phys. Rev. D*, 89:092004, May 2014.

[117] Gabriele Vajente. Notes on measuring coatings with a nodal suspension. Technical report, 2019.

[118] Xiao Liu, S. F. Morse, J. F. Vignola, D. M. Photiadis, A. Sarkissian, M. H. Marcus, and B. H. Houston. On the modes and loss mechanisms of a high Q mechanical oscillator. *Applied Physics Letters*, 78(10):1346–1348, 2001.

[119] A. Alexandrovski, Martin Fejer, A. Markosian, and Roger Route. Photothermal common-path interferometry (PCI): new developments. *Solid State Lasers XVIII: Technology and Devices*, 7193(February 2009):71930D, 2009.

[120] Henry Windischmann. Intrinsic Stress in Sputter-Deposited Thin Films. *Critical Reviews in Solid State and Materials Sciences*, 17(6):547–596, 1992.

[121] B. J. Coomer, A. Resende, J. P. Goss, R. Jones, S. Öberg, and P. R. Briddon. The divacancy in silicon and diamond. *Physica B: Condensed Matter*, 273-274:520–523, 1999.

[122] D. R. Queen, X. Liu, J. Karel, Q. Wang, R. S. Crandall, T. H. Metcalf, and F. Hellman. Light-induced metastability in pure and hydrogenated amorphous silicon. *Epl*, 112(2), 2015.

[123] M. Molina-Ruiz and F. Hellman. Unpublished results. 2017-2018.

[124] R. Poirier, V. Avalos, S. Dannefaer, F. Schiettekatte, and S. Roorda. Divacancies in proton irradiated silicon: Comparison of annealing mechanisms studied with infrared spectroscopy and positron annihilation. *Nuclear Instruments and Methods in Physics Research Section B: Beam Interactions with Materials and Atoms*, 206:85–89, 2003. 13th International Conference on Ion Beam Modification of Materials.

[125] Robert Street. *Technology and Applications of Amorphous Silicon*. 01 2000.

[126] M. A. Green. *Solar cells: Operating principles, technology, and system applications*. 1982.

[127] Brett J. Hallam, Phill G. Hamer, Alison M. Ciesla née Wenham, Catherine E. Chan, Bruno Vicari Stefani, and Stuart Wenham. Development of advanced hydrogenation processes for silicon solar cells via an improved understanding of the behaviour of hydrogen in silicon. *Progress in Photovoltaics: Research and Applications*, 28(12):1217–1238, 2020.

[128] Yoshihiro Hishikawa, Shinya Tsuda, Kenichiro Wakisaka, and Yukinori Kuwano. Principles for controlling the optical and electrical properties of hydrogenated amorphous silicon deposited from a silane plasma. *Journal of Applied Physics*, 73(9):4227–4231, 05 1993.

[129] A.H. Mahan, B.P. Nelson, S. Salamon, and R.S. Crandall. Deposition of device quality, low H content a-Si:H by the hot wire technique. *Journal of Non-Crystalline Solids*, 137-138:657–660, 1991.

[130] M. Molina-Ruiz, H. C. Jacks, D. R. Queen, Q. Wang, R. S. Crandall, and F. Hellman. Two-level systems and growth-induced metastability in hydrogenated amorphous silicon. *Materials Research Express*, 7(9), 2020.

[131] Alex Neumüller, Oleg Sergeev, Stephan J. Heise, Segei Bereznev, Olga Volobujeva, Jose Fabio Lopez Salas, Martin Vehse, and Carsten Agert. Improved amorphous silicon passivation layer for heterojunction solar cells with post-deposition plasma treatment. *Nano Energy*, 43:228–235, 2018.

[132] T. D. Moustakas. Sputtered hydrogenated amorphous silicon. *Journal of Electronic Materials*, 8(3):391–435, 1979.

[133] S. Gerke, H. W. Becker, D. Rogalla, F. Singer, N. Brinkmann, S. Fritz, A. Hammud, P. Keller, D. Skorka, D. Sommer, C. Weiß, S. Flege, G. Hahn, R. Job, and B. Terheiden. Influence of post-hydrogenation upon electrical, optical and structural properties of hydrogen-less sputter-deposited amorphous silicon. *Thin Solid Films*, 598:161–169, 2016.

[134] F. Demichelis, E. Minetti-Mezzetti, A. Tagliaferro, E. Tresso, P. Rava, and N. M. Ravindra. Optical properties of hydrogenated amorphous silicon. *Journal of Applied Physics*, 59(2):611–618, 01 1986.

[135] Jeffrey A. Reimer, Robert W. Vaughan, and John C. Knights. Proton nmr studies of annealed plasma-deposited amorphous si:h films. *Solid State Communications*, 37(2):161–164, 1981.

[136] H. Touir, K. Zellama, and J.-F. Morhange. Local si-h bonding environment in hydrogenated amorphous silicon films in relation to structural inhomogeneities. *Phys. Rev. B*, 59:10076–10083, Apr 1999.

[137] Jonathan Baugh, Daxing Han, Qi Wang, and Yue Wu. Structural changes and hydrogen motion in a-si:h observed by proton nmr. *MRS Proceedings*, 557, 1999.

[138] R. A. Street. *Hydrogenated Amorphous Silicon*. Cambridge Solid State Science Series. Cambridge University Press, 1991.

[139] Maruf Hossain, Husam H. Abu-Safe, Hameed Naseem, and William D. Brown. Characterization of hydrogenated amorphous silicon thin films prepared by magnetron sputtering. *Journal of Non-Crystalline Solids*, 352(1):18–23, 2006.

[140] S. Acco, D. L. Williamson, W. G. J. H. M. van Sark, W. C. Sinke, W. F. van der Weg, A. Polman, and S. Roorda. Nanoclustering of hydrogen in ion-implanted and plasma-grown amorphous silicon. *Phys. Rev. B*, 58:12853–12864, Nov 1998.

[141] Furong Zhu and Jai Singh. Approach to study the relation between optical energy gap and hydrogen concentration in hydrogenated amorphous silicon thin films. *Journal of Applied Physics*, 73(9):4709–4711, 05 1993.

[142] Franco Gaspari and Simone Quaranta. 2.5 PV Materials. In Ibrahim Dincer, editor, *Comprehensive Energy Systems*, pages 117–149. Elsevier, Oxford, 2018.

[143] C. H. Seager, P. M. Lenahan, K. L. Brower, and R. E. Mikawa. Dangling bonds and the Urbach tail in silicon. *Journal of Applied Physics*, 58(7):2704–2708, 10 1985.

[144] George D. Watkins. Intrinsic defects in silicon. *Materials Science in Semiconductor Processing*, 3(4):227–235, 2000.

[145] M Ahmed, S.J Watts, J Matheson, and A Holmes-Siedle. Deep-level transient spectroscopy studies of silicon detectors after 24gev proton irradiation and 1mev neutron irradiation. *Nuclear Instruments and Methods in Physics Research Section A: Accelerators, Spectrometers, Detectors and Associated Equipment*, 457(3):588–594, 2001.

[146] Paweł Kamiński, Jarosław Żelazko, Roman Kozłowski, Christian Hindrichsen, and Leif Jensen. Investigation of energy levels of small vacancy clusters in proton irradiated silicon by laplace photoinduced transient spectroscopy. *Crystals*, 12(12), 2022.

[147] Sokrates T. Pantelides. The electronic structure of impurities and other point defects in semiconductors. *Rev. Mod. Phys.*, 50:797–858, Oct 1978.

[148] R. L. Aggarwal and A. K. Ramdas. Optical determination of the symmetry of the ground states of group-v donors in silicon. *Phys. Rev.*, 140:A1246–A1253, Nov 1965.

[149] Abdel Ilah El Khalfi, El Maati Ech-Chamikh, Youssef Ijdiyaou, Mustapha Azizan, Abdelhadi Essafti, Lahcen Nkhaili, and Abdelkader Outzourhit. Infrared and raman study of amorphous silicon carbide thin films deposited by radiofrequency cosputtering. *Spectroscopy Letters*, 47(5):392–396, 2014.

[150] G. Foti. Silicon carbide: from amorphous to crystalline material. *Applied Surface Science*, 184(1):20–26, 2001. Proceeding of the European Materials Research Soceity 2001-Symposium F "Amorphous and crystalline Silicon Carbide: material and applications".

[151] Alex Amato. *Low Thermal Noise Coating for New Generation Gravitational-Wave Detectors*. Theses, Université de Lyon, November 2019.

[152] G. Favaro, M. Bazzan, A. Amato, F. Arciprete, E. Cesarini, A.J. Corso, F. De Matteis, T.H. Dao, M. Granata, C. Honrado-Benítez, N. Gutiérrez-Luna, J.I. Larruquert, G. Lorenzin, D. Lumaca, G. Maggioni, M. Magnozzi, M.G. Pelizzo, E. Placidi, P. Prosposito, and F. Puosi. Measurement and simulation of mechanical and optical properties of sputtered amorphous sic coatings. *Phys. Rev. Appl.*, 18:044030, Oct 2022.

[153] D. Dasgupta, F. Demichelis, C. F. Pirri, and A. Tagliaferro. π bands and gap states from optical absorption and electron-spin-resonance studies on amorphous carbon and amorphous hydrogenated carbon films. *Phys. Rev. B*, 43:2131–2135, Jan 1991.

[154] C. Oppedisano and A. Tagliaferro. Relationship between sp2 carbon content and E04 optical gap in amorphous carbon-based materials. *Applied Physics Letters*, 75(23):3650–3652, 12 1999.

[155] G. Fanchini, A. Tagliaferro, D. P. Dowling, K. Donnelly, M. L. McConnell, R. Flood, and G. Lang. Interdependency of optical constants in $a-\mathrm{C}$ and $a-\mathrm{C:H}$ thin films interpreted in light of the density of electronic states. *Phys. Rev. B*, 61:5002–5010, Feb 2000.

[156] J. Robertson. Diamond-like amorphous carbon. *Materials Science and Engineering: R: Reports*, 37(4):129–281, 2002.

[157] Mingming Li, Lihua Jiang, Yihua Sun, Ting Xiao, Peng Xiang, and Xinyu Tan. Silicon content influence on structure and photoluminescence properties of carbon rich hydrogenated amorphous silicon carbide thin films. *Journal of Alloys and Compounds*, 753:320–328, 2018.

[158] M. Chhowalla, J. Robertson, C. W. Chen, S. R. P. Silva, C. A. Davis, G. A. J. Amaratunga, and W. I. Milne. Influence of ion energy and substrate temperature on the optical and electronic properties of tetrahedral amorphous carbon (ta-C) films. *Journal of Applied Physics*, 81(1):139–145, 01 1997.

[159] Q. Wei and J. Narayan. Superhard diamondlike carbon: preparation, theory, and properties. *International Materials Reviews*, 45(4):133–164, 2000.

A. PCI - CORRECTION FACTOR

In the PCI method, for a film with a refractive index that is much higher than that of the substrate, the incident laser beam creates a standing wave. The intensity of the wave is influenced by the reflectivities of both interfaces and the optical thickness of the film. It also varies across the film's thickness, requiring appropriate averaging to extract the desired absorption coefficient from the measured temperature rise. The magnitude of the electromagnetic field within the film is expressed as,

$$E_{e0} = t_1 E_{in} + E_{c0} r_1 r_2 e^{i2\phi} \tag{A.1}$$

where E_{in} and E_{c0} stand for the incident electromagnetic field and the field circulating just inside the top surface of the film. In Eq. A.1, t_1, r_1 and r_2 are transmission and reflection coefficients for the front (index 1) and rear (index 2) surfaces, and $\phi = 2\pi nd/\lambda$ is the optical thickness of the film with the physical thickness d at a laser wavelength of λ. The total power in the film is then:

$$P_{tot} = \int_0^d P_{abs}(z)\, dz = \frac{1}{2}\alpha \int_0^d |E(z)|^2\, dz = \frac{\alpha d |E_{in}|^2}{2}(1 - r_1^2) F_{corr} \tag{A.2}$$

where the prefactor F_{corr} is the result in the absence of interference effects, which is given by

$$F_{corr} = \frac{1 + r_2^2 + r_2 sin(2\phi)/\phi}{1 + r_1^2 r_2^2 - 2 r_1 r_2 cos(2\phi)} \tag{A.3}$$

with $r_1 = \frac{n_f - n_{air}}{n_f + n_{air}}$ and $r_2 = \frac{n_s - n_f}{n_s + n_f}$. The terms n_{air}, n_f and n_s represent the refractive index of air (1), film (3.6 for a-Si, 2.46−3.06 for a-SiC depending on its Si content [149]) and substrate (1.45 for fused silica).

Hence, the measured values of the optical absorption, α_m, were corrected by F_{corr}, with the value of this correction factor for each sample reported in this work listed in Table A.1.

$$\alpha = \frac{\alpha_m}{F_{corr}} \tag{A.4}$$

Table A.1: Summary of MS a-Si(:H) (discussed in Chapter 6), a-Si_xC_{1-x}(:H) (discussed in Chapter 7) and a-Si(:H) underwent annealing in air (discussed in Appendix B) samples for optical absorption measurements using PCI.

Sample	Deposition conditions	Substrate type	Film thickness (nm)	F_{corr}		
				1064 nm	1550 nm	2000 nm
a-Si(:H)						
S22-038B	RT, Ar 1.5 mTorr	C7980	364.1±0.9	1.984	1.420	1.235
S22-039B	360 °C, Ar 1.5 mTorr	C7980	377.9±0.4	1.975	1.171	1.473
S22-041C	360 °C, Ar/5% H_2 1.5 mTorr	C7979	341.9±0.4	1.295	1.890	0.961
S22-042D	RT, Ar/5% H_2 1.5 mTorr	C7979	331.8±0.6	1.045	2.031	0.879
S23-037D	360 °C, Ar/10% H_2 1.5 mTorr	C7979	331.2±1.1	1.034	2.036	0.875
S23-039D	RT, Ar/10% H_2 1.5 mTorr	C7979	328.4±1.0	0.982	2.051	0.857
a-Si_xC_{1-x}(:H)						
S21-089C	RT, Ar 1.5 mTorr	C7979	311.4±1.0	1.337	0.861	1.118
S21-091C	RT, Ar 4.0 mTorr	C7979	314.7±1.3	1.351	0.857	1.103
S21-025B	360 °C, Ar 4.0 mTorr	C7979	320.7±3.0	1.366	0.852	1.078
S21-059F	360 °C, Ar/0.5% H_2 4.0 mTorr	C7979	348.5±3.2	1.283	0.866	0.975
S21-061F	360 °C, Ar/1% H_2 4.0 mTorr	C7979	324.2±3.2	1.370	0.851	1.064
S21-062F	360 °C, Ar/5% H_2 4.0 mTorr	C7979	334.5±4.2	1.354	0.852	1.024
S23-055D	RT, Ar 1.5 mTorr, $Si_{90}C_{10}$	C7980	325.6±4.0	0.877	1.146	0.800
a-Si (air annealed)						
S21-098C	360 °C, Ar 1.5 mTorr	C7979	356.6±0.3	1.782	1.579	1.127
S21-099C	RT, Ar 1.5 mTorr	C7979	335.0±0.3	1.114	1.998	0.902

B. ANNEALING AMORPHOUS Si IN AIR

This appendix presents a comparative study between annealing in air and annealing in vacuum for magnetron sputtered *a*-Si films. The annealing process is a crucial post-growth treatment that allows for relaxation of internal stresses and rearrangement of atoms, thus influencing the film's properties. Annealing in air is a commonly used method for LIGO mirror coatings since they are currently made of oxide materials (*a*-Ti:Ta_2O_2 and *a*-SiO_2). However, annealing *a*-Si in air poses a challenge due to the potential oxidation of silicon, which can significantly impact the properties of the resulting film.

It is worth noting that *a*-SiO_2, the oxide formed during air annealing, has been shown to exhibit low room-temperature mechanical loss [94] and low optical absorption [96], making it challenging to discern the true effects of annealing on *a*-Si itself. The presence of surface oxide may effectively lower both the measured Q_{RT}^{-1} and absorption of the annealed *a*-Si film, thereby complicating our understanding of the intrinsic impact of annealing on *a*-Si.

By contrast, annealing in vacuum avoids the oxidation issue and provides a controlled environment for examining the effects of post-growth treatment on *a*-Si films. Figure B.1 compares the optical absorption of vacuum- and air-annealed MS *a*-Si. The observations from the comparison are as follows: 1) Among the 360 °C-deposited samples, the one annealed in air shows a larger reduction in absorption compared to its as-deposited state at both wavelengths studied. 2) The samples annealed in air exhibit a weaker response to the subsequent post-hydrogenation; the reduction in absorption at both 1550 and 2000 nm is less pronounced in air-annealed *a*-Si. The first observation can be attributed to the lower density of the 360 °C, Ar 1.5 mTorr *a*-Si, as illustrated in Fig. 4.1, which facilitates oxygen diffusion and potentially leads to the formation of a thicker oxide layer. Consequently, the optical absorption at these wavelengths decreases as *a*-SiO_2 is transparent to them. However, the formation of this oxide may act as a diffusion barrier, hindering the incorporation of hydrogen during post-H, thus making the post-H process less effective on air-annealed samples.

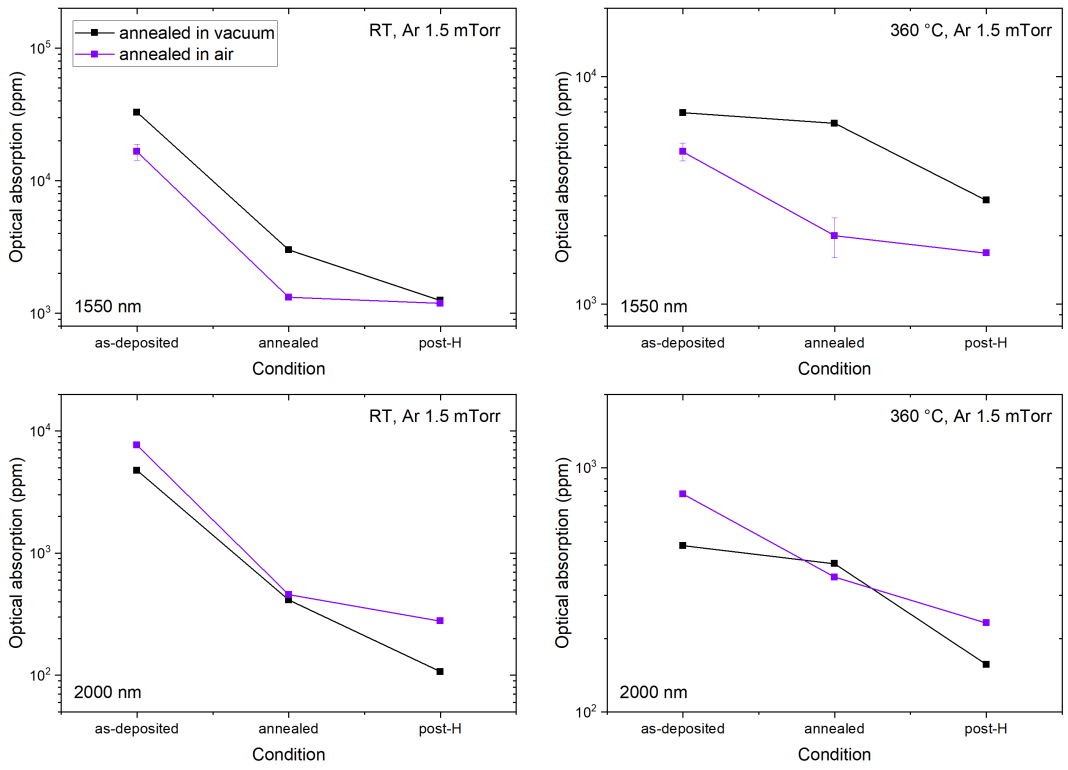

Figure B.1: Comparison of the optical absorption of MS a-Si films deposited at RT and 360 °C, Ar 1.5 mTorr, after undergoing annealing in both vacuum (black lines) and air (purple lines), at 1550 nm (top) and 2000 nm (bottom).

C. TABLES OF EXPERIMENTAL RESULTS

Table C.1: List of structural properties of MS Ar-deposited a-Si.

Sample state	Growth conditions	ρ_{at} $\times 10^{22}$ cm^{-3}	$\Delta\theta$ $^\circ$	-tr(ε) %	ρ_{DB} $\times 10^{18}$ cm^{-3}	O content at.%
as-deposited	RT, 1.5 mTorr	5.08±0.06	11.00±0.18	1.24±0.03	20.0±1.2	0.29
	360 °C, 1.5 mTorr	4.73±0.09	9.62±0.10	0.59±0.03	17.5±1.0	0.19
	RT, 4.0 mTorr	4.87±0.13	11.13±0.22	2.30±0.03	13.5±0.8	0.92
	360 °C, 4.0 mTorr	4.94±0.07	9.88±0.13	1.17±0.03	14.4±0.8	-
	RT, 10.0 mTorr	3.48±0.21	10.22±0.10	2.37±0.03	10.4±0.6	37.99
	360 °C, 10.0 mTorr	4.48±0.43	9.20±0.07	1.59±0.03		12.26
annealed	RT, 1.5 mTorr		10.10±0.10	1.57±0.03	20.4±1.1	
	360 °C, 1.5 mTorr		9.07±0.07	0.67±0.03	14.7±0.8	
	RT, 4.0 mTorr		10.35±0.10	2.35±0.03		
	360 °C, 4.0 mTorr		9.70±0.10	1.63±0.03	6.1±0.3	
	RT, 10.0 mTorr		11.07±0.10	2.78±0.03		
	360 °C, 10.0 mTorr		9.80±0.08	2.02±0.03		

Table C.2: Mechanical loss and elastic constants of MS Ar-deposited a-Si.

Sample state	Growth conditions	$Q^{-1}_{0,1K}$ $\times 10^{-5}$	$Q^{-1}_{0,10K}$ $\times 10^{-5}$	Q^{-1}_{100K} $\times 10^{-5}$	G GPa	Q^{-1}_{RT} $\times 10^{-4}$	E GPa	ν
as-deposited	RT, 1.5 mTorr	4.8	6.5	17.4	31.8	2.91±0.04	122.0±1.6	0.408±0.002
	360 °C, 1.5 mTorr	2.5	3.0	13.3	46.1	1.12±0.01	135.7±1.6	0.287±0.002
	RT, 4.0 mTorr							
	360 °C, 4.0 mTorr	2.8	3.3	13.4	44.6	1.25±0.01	123.4±1.6	0.402±0.002
	RT, 10.0 mTorr							
	360 °C, 10.0 mTorr							
annealed	RT, 1.5 mTorr					0.85±0.03	136.4±1.7	0.334±0.002
	360 °C, 1.5 mTorr	2.4	2.9	12.5	46.7	1.53±0.01	138.2±1.7	0.104±0.002
	RT, 4.0 mTorr							
	360 °C, 4.0 mTorr					0.90±0.01	140.5±1.6	0.320±0.001
	RT, 10.0 mTorr							
	360 °C, 10.0 mTorr							

Table C.3: List of structural properties of MS Ne-, Ar-, Kr- and Xe-deposited a-Si.

Working gas	Growth conditions	ρ_{at} $\times 10^{22}$ cm^{-3}	$\Delta\theta$ $^{\circ}$	-tr(ε) %	ρ_{DB} $\times 10^{18}$ cm^{-3}	O content at.%
Ne	360 °C, 11.0 mTorr	3.68±0.21	9.50±0.07	1.67±0.02	8.5±1.0	5.97
Ar	360 °C, 1.5 mTorr	4.73±0.09	9.62±0.10	0.59±0.02	17.5±1.0	0.19
Kr	360 °C, 1.5 mTorr	4.68±0.19	8.43±0.07	0.33±0.02	12.7±1.4	0.19
Xe	360 °C, 0.5 mTorr	4.81±0.13	8.43±0.02	1.26±0.02	12.8±1.3	-
	360 °C, 1.5 mTorr	4.97±0.08	8.37±0.02	1.28±0.02	16.4±1.7	0.48

[a] *The gas inclusion in all samples is below the detection limit (0.1 at.%), except for the Ne-deposited a-Si (∼2 at.%).*

Table C.4: Mechanical loss and elastic constants of MS Ne-, Ar-, Kr- and Xe-deposited a-Si.

Working gas	Growth conditions	$Q^{-1}_{0,1K}$ $\times 10^{-5}$	$Q^{-1}_{0,10K}$ $\times 10^{-5}$	Q^{-1}_{100K} $\times 10^{-5}$	G GPa	Q^{-1}_{RT} $\times 10^{-4}$	E GPa	ν
Ne	360 °C, 18.0 mTorr					6.47±0.04	82.0±5.3	0.261±0.154
Ar	360 °C, 1.5 mTorr	2.5	3.0	1.3	46.1	1.12±0.01	135.7±1.6	0.287±0.002
Kr	360 °C, 1.5 mTorr	1.4	1.9	9.1	45.3	1.06±0.01	128.0±1.3	0.288±0.021
Xe	360 °C, 0.5 mTorr	0.8	1.2	6.7	48.3	0.90±0.01	129.1±2.3	0.355±0.025
	360 °C, 1.5 mTorr	1.7	2.0	10.2	48.2	0.89±0.01	137.7±2.1	0.275±0.029

Table C.5: List of structural properties of MS Ar- and Ar/H_2-deposited a-Si:H.

Sample state	Growth conditions	ρ_{at} $\times 10^{22}$ cm^{-3}	$\Delta\theta$ $^\circ$	-tr(ε) %	ρ_{DB} $\times 10^{18}$ cm^{-3}	O content at.%
as-deposited	RT, 1.5 mTorr	5.08±0.06	11.00±0.18	1.24±0.03	20.0±1.2	0.29
	360 °C, 1.5 mTorr	4.73±0.09	9.62±0.10	0.59±0.03	17.5±1.0	0.19
	RT, Ar/5% H_2	4.71±0.12	8.88±0.06	2.18±0.02	18.7±1.0	0.49
	360 °C, Ar/5% H_2	4.78±0.05	8.81±0.05	1.40±0.02	1.8±0.1	-
	RT, Ar/10% H_2	4.65±0.05	8.76±0.08	1.65±0.02		0.41
	360 °C, Ar/10% H_2	4.72±0.05	8.77±0.05	0.76±0.02		-
annealed	RT, Ar only	5.04±0.06	10.10±0.10	1.57±0.03	20.4±1.1	
	360 °C, Ar only	4.79±0.09	9.07±0.07	0.67±0.03	14.7±0.8	
	RT, Ar/5% H_2	4.85±0.14	8.90±0.07	1.44±0.02	1.3±0.1	0.22
	360 °C, Ar/5% H_2	4.91±0.07	8.81±0.05	0.75±0.02	1.7±0.1	-
	RT, Ar/10% H_2	4.60±0.08	8.56±0.09	1.51±0.02		0.72
	360 °C, Ar/10% H_2	4.69±0.06	8.73±0.05	0.78±0.02		-
post-H	RT, Ar only	4.60±0.09	8.99±0.05	1.37±0.02	3.8±0.2	0.60
	360 °C, Ar only	4.75±0.05	8.73±0.06	0.79±0.02	4.8±0.3	0.20
	RT, Ar/5% H_2	4.79±0.18	8.68±0.07	1.35±0.02	0.3±0.0	0.18
	360 °C, Ar/5% H_2	4.91±0.13	8.81±0.05	0.69±0.02	0.9±0.1	0.27
	RT, Ar/10% H_2	4.57±0.08	8.67±0.08	1.47±0.02		0.47
	360 °C, Ar/10% H_2	4.69±0.08	8.70±0.05	0.63±0.02		0.18

[a] *Note that the same thickness was used to estimate the atomic density for the same sample in all three states, as the change in film thickness after post-growth processing is within 2%, except for the RT- and 360 °C-deposited Ar only samples. For these samples, change in thickness was used to estimate the ρ_{at} of their annealed state.*

Table C.6: Mechanical loss and elastic constants of MS Ar- and Ar/H_2-deposited a-Si:H.

Sample state	Growth conditions	$Q^{-1}_{0,1K}$ $\times 10^{-5}$	$Q^{-1}_{0,10K}$ $\times 10^{-5}$	Q^{-1}_{100K} $\times 10^{-5}$	G GPa	Q^{-1}_{RT} $\times 10^{-4}$	E GPa	ν
as-deposited	RT, 1.5 mTorr	4.8	6.5	17.4	31.8	2.91±0.04	122.0±1.6	0.408±0.002
	360 °C, 1.5 mTorr	2.5	3.0	13.3	46.1	1.12±0.01	135.7±1.6	0.287±0.002
	RT, Ar/5% H_2					1.95±0.01	113.3±1.8	0.419±0.002
	360 °C, Ar/5% H_2					0.23±0.01	129.5±1.7	0.343±0.002
	RT, Ar/10% H_2							
	360 °C, Ar/10% H_2							
annealed	RT, 1.5 mTorr					0.85±0.03	136.4±1.7	0.334±0.002
	360 °C, 1.5 mTorr	2.4	2.9	13.4	46.7	1.53±0.01	138.2±1.7	0.104±0.002
	RT, Ar/5% H_2					0.59±0.01	121.2±1.6	0.372±0.002
	360 °C, Ar/5% H_2					0.27±0.01	132.1±1.6	0.341±0.002
	RT, Ar/10% H_2							
	360 °C, Ar/10% H_2							
post-H	RT, Ar only					0.50±0.02	113.1±1.6	0.413±0.002
	360 °C, Ar only					1.15±0.01	119.4±1.5	0.395±0.002
	RT, Ar/5% H_2					0.75±0.01	126.5±1.6	0.337±0.002
	360 °C, Ar/5% H_2					0.22±0.01	134.0±1.6	0.339±0.002
	RT, Ar/10% H_2							
	360 °C, Ar/10% H_2							

[a] *G is the shear modulus extracted from DPO measurements at 300 K, and E and ν are Young's modulus and Poisson's ratio obtained from GeNS measurements (Sec. 3.3.8 and 3.3.9).*

D. CORRELATION MATRICES OF PROPERTIES

	ρ_{at}	$\Delta\theta$	tr(ε)	%DB	Q_0^{-1}	Q_{RT}^{-1}	G
ρ_{at}	1						
$\Delta\theta$	-0.063	1					
tr(ε)	-0.354	0.538	1				
%DB	0.375	-0.086	-0.126	1			
Q_0^{-1}	-0.600	0.699	0.791	-0.264	1		
Q_{RT}^{-1}	-0.312	0.634	0.372	-0.496	0.852	1	
G	0.130	-0.604	-0.588	-0.533	-0.593	-0.483	1

Table D.1: Correlation between properties of MS and e-beam a-Si data, excluding MS Ne a-Si. %DB represents the percentage of dangling bonds in the Si-Si bonding network, taking into account ρ_{DB} and ρ_{at}. Cells highlighted in yellow indicate statistically significant results.

	ρ_{at}	$\Delta\theta$	tr(ε)	%DB	Q_0^{-1}	Q_{RT}^{-1}	G
ρ_{at}	1						
$\Delta\theta$	0.586	1					
tr(ε)	0.807	0.354	1				
%DB	0.598	0.868	0.338	1			
Q_0^{-1}	0.667	0.957	0.197	0.389	1		
Q_{RT}^{-1}	0.657	0.649	-0.072	0.706	0.888	1	
G	-0.609	-0.862	-0.174	-0.674	-0.918	-0.995	1

Table D.2: Correlation between properties of MS a-Si data only, excluding MS Ne a-Si. %DB represents the percentage of dangling bonds in the Si-Si bonding network, taking into account ρ_{DB} and ρ_{at}. Cells highlighted in yellow indicate statistically significant results.